2012

Pulmonary fluid dynamics and aerosol drug delivery in the upper tracheobronchial airways under mechanical ventilation conditions

Timothy Andrew Van Rhein

Department:

PULMONARY FLUID DYNAMICS AND AEROSOL DRUG DELIVERY IN THE UPPER TRACHEOBRONCHIAL AIRWAYS UNDER MECHANICAL VENTILATION CONDITIONS

By

TIMOTHY ANDREW VAN RHEIN

A THESIS

Presented to the Faculty of the Graduate School of the

MISSOURI UNIVERSITY OF SCIENCE AND TECHNOLOGY

In Partial Fulfillment of the Requirements for the Degree

MASTERS OF SCIENCE IN MECHANICAL ENGINEERING

2012

Approved by

Arindam Banerjee, Advisor

John Singler

David Riggins

ABSTRACT

The effects of mechanical ventilation conditions on fluid flow and particle deposition were studied in a computer model of the human airways. The frequency with which aerosolized drugs are delivered to mechanically ventilated patients demonstrates the importance of understanding the effects that ventilation parameters have on particle deposition in the human airways. Past studies that modeled particle deposition in silico frequently used an idealized geometry with steady inlet conditions. With recent advancements in computational power and medical imaging capabilities, studies have begun to use more realistic geometries or unsteady inlet conditions that model normal breathing. This study focuses specifically on the effects of mechanical ventilation waveforms using a computer model of the airways from the endotracheal tube to generation G7, in the lungs of a patient undergoing mechanical ventilation treatment. Computational fluid dynamics (CFD), using the commercial software package ANSYS® CFX®, combined with realistic respiratory waveforms commonly used by commercial mechanical ventilators, large eddy simulation (LES) to model turbulence, and user defined particle force models were applied to solve for fluid flow and particle deposition parameters. The endotracheal tube (ETT) was found to be an important geometric feature, causing a fluid jet towards the right main bronchus, increased turbulence, and a recirculation zone in the right main bronchus. In addition to the enhanced deposition seen at the carinas of the airway bifurcations, enhanced deposition was also seen in the right main bronchus due to impaction and turbulent dispersion resulting from the fluid structures created by the ETT. The dependence of local particle deposition on respiratory waveforms implies that great care should be taken when selecting ventilation parameters.

ACKNOWLEDGEMENTS

I would like to thank my advisor, Dr. Arindam Banerjee, for offering guidance and motivation throughout my research and thesis writing. I would like to express gratitude to my thesis committee members, Dr. John Singler and Dr. David Riggins, for their support and cooperation. I would like to offer a special thanks to Dr. John Singler for offering his expertise and experience with numerical methods and coding. I would like to thank Dr. Gary Salzman for his cooperation and for providing the CT scans used for geometry creation. Thanks to University of Missouri Research Board Award to Dr. Banerjee (PI) titled: Optimization of aerosol-drug delivery in mechanically-ventilated lungs. Additional thanks to the Missouri S&T Chancellor's office for funding.

I would like to thank the members of my lab group, Mohammed Alzahrany, Aaron Haley, Varun Lobo, Raghu Mutnuri, Pamela Roach, Suchi Mukherji, Nitin Kolekar, Ashwin Vinod, Rahul Nemani, and Taylor Rinehart. Their range of skill sets, and their patience and willingness to teach me what they know helped me to grow as an engineer and to create something I can be truly proud of. I would like to thank Connie Gensamer for providing support for software troubleshooting and installation problems. I would also like to thank the mechanical and aerospace engineering department administrative staff.

I would like to give thanks to my mother and father, my grandparents, my brothers, my aunts and uncles, and my cousins. The support, encouragement, and inspiration that my family has offered me throughout my studies have been invaluable. Finally I would like to thank my wife and daughter, who are my world, who all of this is done for, and without whom, none of this would have been achievable.

TABLE OF CONTENTS

Page

LIST OF FIGURES

Page

LIST OF TABLES

Page

1. INTRODUCTION

Breathing is an essential function to maintain life. Respiration is a function by which gas exchange occurs -the body takes in oxygen from the environment and expels carbon dioxide. The process of gas exchange involves two primary mechanisms: conduction of gases from the external environment to the alveolar zone, and a subsequent diffusion based exchange across the epithelium into the bloodstream [1]. Air enters the lungs when a lower pressure is created due to the expansion of the lungs. The expansion is controlled by a set of muscles in the thoracic cavity, most notably the diaphragm which is located below the lungs. When the lungs prove inadequate to deliver oxygen due to various medical conditions, mechanical ventilation is often a lifesaving intervention [2].

It is a very common therapeutic technique to deliver medicine in aerosolized form to mechanically ventilated patients. The ability of other inhaled materials to also pass through the epithelium into the bloodstream is what makes drug delivery in the lungs possible. The structure of the lung has evolved to serve the function of a delivery mechanism. For this reason it is also ideal for delivery of aerosolized drugs and at risk to deliver inhaled toxins to the body. A better understanding of the mechanisms behind the deposition of inhaled particulates is thus critical in improving aerosolized drug delivery and mitigating the dangers of inhalation of airborne toxins.

1.1. TERMINOLOGY AND STRUCTURE OF THE HUMAN AIRWAYS

The human airways are a network of gas channels with complex and dynamic features. The airways can be divided into three regions based on anatomy: (a) extrathoracic region which includes the oral cavity, the nasal cavity, the pharynx, the larynx, and the upper part of the trachea (b) upper bronchial region which includes the

bronchi, and (c) lower bronchial region which contains the bronchioles and the alveolar region [3]. The term tracheobronchial (henceforth referred to as TB) refers to a region including the trachea and the upper bronchial region. With a focus on respiratory function, it is convenient to separate the lungs into the conducting zone, and the respiratory zone. The conducting zone contains all of the airways above the respiratory bronchioles. The purpose of the conducting zone is to move large volumes of air from the larger airways to the tiny airways where the flow velocity will be low enough, and there will be enough surface area, for gas exchange to occur through the epithelium. No gas exchange occurs in the conducting zone. Respiratory bronchioles are sometimes seen as a transition zone where the air continues to move to lower airways but some gas exchange does occur. The respiratory zone consists of alveolar ducts and sacs where the primary function is gas exchange [4]. An acinus is a tiny respiratory unit that consists of a primary respiratory bronchiole and all of the respiratory bronchioles, alveolar ducts, and alveolar sacs it supplies [5].

Air that enters through the mouth will pass through the oral cavity into the pharynx. The pharynx acts as a pipe junction as it connects to the nasal cavity, oral cavity, larynx, and esophagus. It is broken into three parts: (1) the nasopharynx which connects to the nasal cavity and leads into (2) the oropharynx which connects to the oral cavity and leads into (3) the laryngopharynx (sometimes called the hypopharynx) which connects to the esophagus and larynx (refer to Figure 1.1) [1]. Air that enters through the nose will pass through the nasal cavity and nasopharynx into the oropharynx. From the oropharynx the air conducts downward through the laryngopharynx past the epiglottis and through the larynx into the trachea. The epiglottis is a movable flap of cartilage and

tissue that covers the opening of the larynx to direct food or drink down the esophagus while swallowing [6]. The larynx leads into the trachea and contains the glottis [6].

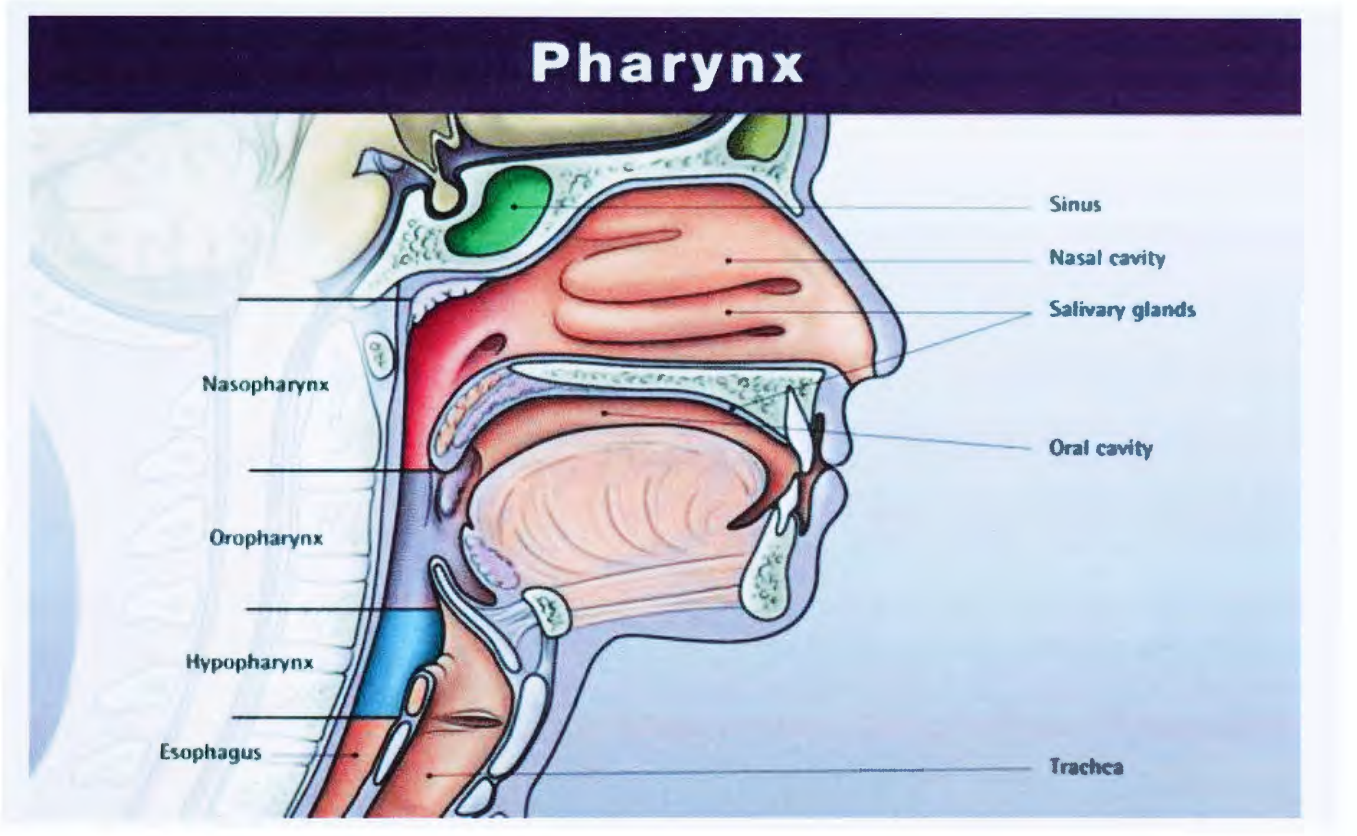

Figure 1.1: Upper airway terminologies [7]

Beginning from the trachea, the lungs split repeatedly. The trachea splits into the left and right main bronchi which split into the lobar bronchi. The left lung contains two lobes, referred to as the left upper and lower lobes; whereas the right lung consists of three lobes that are referred to as the right upper, middle, and lower lobes [1]. The lobar bronchi continue to split into the tertiary bronchi, each of which supplies a broncho-pulmonary segment (BPS) [8]. A BPS is a segment of the lung that is supplied by its

own blood vessels and is separated from the other segments by connective tissue. The BPSs contain the bronchioles and alveolar ducts and sacs, and mark the end of the bronchi. The primary bronchioles (i.e. the first airways in each BPS) continue to split repeatedly until the terminal bronchioles which supply the respiratory bronchioles and are considered to be the most distal airways (farthest from the stem, or trachea). The respiratory bronchioles contain alveoli, but also continue to split and supply alveolar ducts and sacs where gas exchange primarily takes place.

The airways after each bifurcation (or split) are considered to be in a new generation and the number of airways in each generation is approximately double that of the previous generation. The lungs are made up of about 23 generations of branching airways with the trachea as the 0^{th} generation (G0), the left and right main bronchi as the 1^{st} and so on [5]. The bronchioles begin at generations 3 or 4 and continue through generations 16 to 19 [5]. The alveolar ducts are only present for about 4 generations after the respiratory bronchioles. The airways terminate at the alveolar sacs. A bifurcation primarily consists of a parent branch that splits into two daughter branches. A parent branch is considered to be proximal (closer to the trachea) to the daughter branch and the daughter branches are considered to be distal (farther from the trachea) to the parent branch. In general the size of the parent branch is larger than that of its daughter branches with few exceptions [5]. The size of an airway could be characterized by a diameter; however the airways are not perfectly round. For this reason it is convenient to define a hydraulic diameter (D_h) to characterize the size of an airway as:

$$D_h = \frac{4A}{P} \tag{1.1}$$

where A is the cross sectional area, and P is the wetted perimeter of a slice, cut perpendicular to the center line of the airway. It should be noted that the hydraulic diameter for the pulmonary airways is not strictly constant along the axis of an airway but rarely varies significantly. The branch angle is the angle between the two daughter branches of a bifurcation, the ridge-like area where the parent branch separates being called a carina. Figure 1.2 illustrates some of the commonly used terminologies that are used to quantify pulmonary bifurcations.

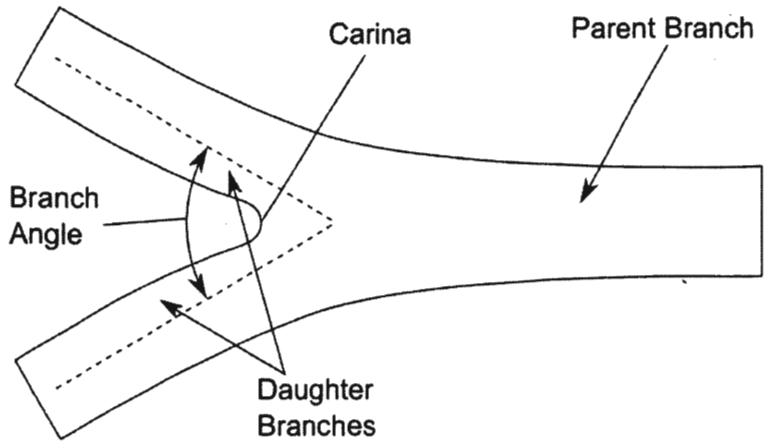

Figure 1.2: Illustration of bifurcation terminologies.

The lining of the airways is known as an epithelium. In the alveoli, the epithelium is comprised of type I and type II epithelial cells. Type I epithelial cells make up about 97% of the alveolar surface and their primary function is gas exchange. Type II epithelial cells are responsible for secreting a surfactant that increases the airway compliance, prevents atelectasis (lung collapse), and helps keep the alveoli dry [5]. The

thickness of the pulmonary blood-air barrier can be as small as 0.5 μm [9]. The rest of the airway walls are lined with a variety of epithelial cells and a layer of mucus. The mucus, along with tight junctions between epithelial cells protects the internal lung structures [5]. Throughout most of the airways, the epithelium is lined with ciliated cells. These ciliated cells beat frequently to propel the layer of mucus upwards towards the laryngopharynx, where it is either passed down the esophagus to be swallowed, or passed through the oropharynx to be expectorated [5, 10]. The mucus is secreted by cells of the airway epithelium, but not in the alveoli [5]. The flowing layer of mucus is commonly referred to as the mucociliary escalator [10]. The mucus flows more quickly in the larger airways then in the smaller airways because the surface area over which the mucus can flow decreases as the mucus moves towards the trachea [5]. The mucus layer is biphasic with a less viscous layer directly against the ciliated walls and a viscous gel layer on top. The functions of the mucus layer are to keep the epithelium from dehydration, to humidify inhaled air, and to protect the airways by trapping inhaled particulate matter. The thickness of the mucus layer is variable, and can change due to factors such as coughing, hyper-secretion of mucus, or insufficient activity of the mucociliary escalator [1]. The upper airways of the lung contain cartilage to maintain airway rigidity. The trachea contains C-shaped rings of cartilage and these rings continue into the main bronchi. The amount of cartilage decreases as the generation number increases and the shape of the cartilage changes from rings to irregular-shaped plates.

Under normal breathing conditions the lungs will repeatedly fill and deflate. The volume of air that enters and exits the lungs is known as tidal volume. The total lung capacity is the volume of air present in the lungs after a deep breath inward. Even after

expiration, with full effort to empty the lung, there still remains a volume of air in the lungs which is known as the residual volume. The difference between the total lung capacity and the residual volume is known as the vital capacity. The inspiratory reserve volume is the volume of air that can be inhaled beyond a normal tidal inspiration and the expiratory reserve volume is the volume of air that can be exhaled beyond a normal tidal expiration. The sum of the inspiratory reserve volume and the tidal volume is the inspiratory capacity. The expiratory reserve volume plus the residual volume is the functional residual capacity which is also equal to the total lung capacity minus the inspiratory capacity, and represents the volume of air that remains in the lungs after a normal tidal expiration. These terms are illustrated in Figure 1.3.

Turbulence is present in the human airways. For flow in a straight pipe turbulence is classified based on the Reynolds number (Re) defined the ratio of inertial forces to viscous forces and described by [11]:

$$\mathrm{Re} = \frac{\rho d_h U}{\mu} \tag{1.2}$$

where ρ is the fluid density, d_h is the hydraulic diameter, U is the mean flow velocity, and μ is the fluid dynamic viscosity. In laminar flow, viscous forces dominate, and the fluid flow is stable (flow along streamlines). When inertial forces dominate a flow, the flow will become unstable and turbulence may arise. Typically the limit for laminar flow in a smooth pipe is a Re less than 2300 [11]. Turbulence may also develop in the airways when the geometry varies significantly from that of a smooth pipe such as in the larynx [12]. In the human airways, turbulence may first develop between the soft pallet and the

throat [13] and after the larynx, but will re-laminarize in the lower airways where the Reynolds number is lower [14]. Turbulence is expected in the airways from generation G0 (just after the larynx) and may be present up to generation G6 [13].

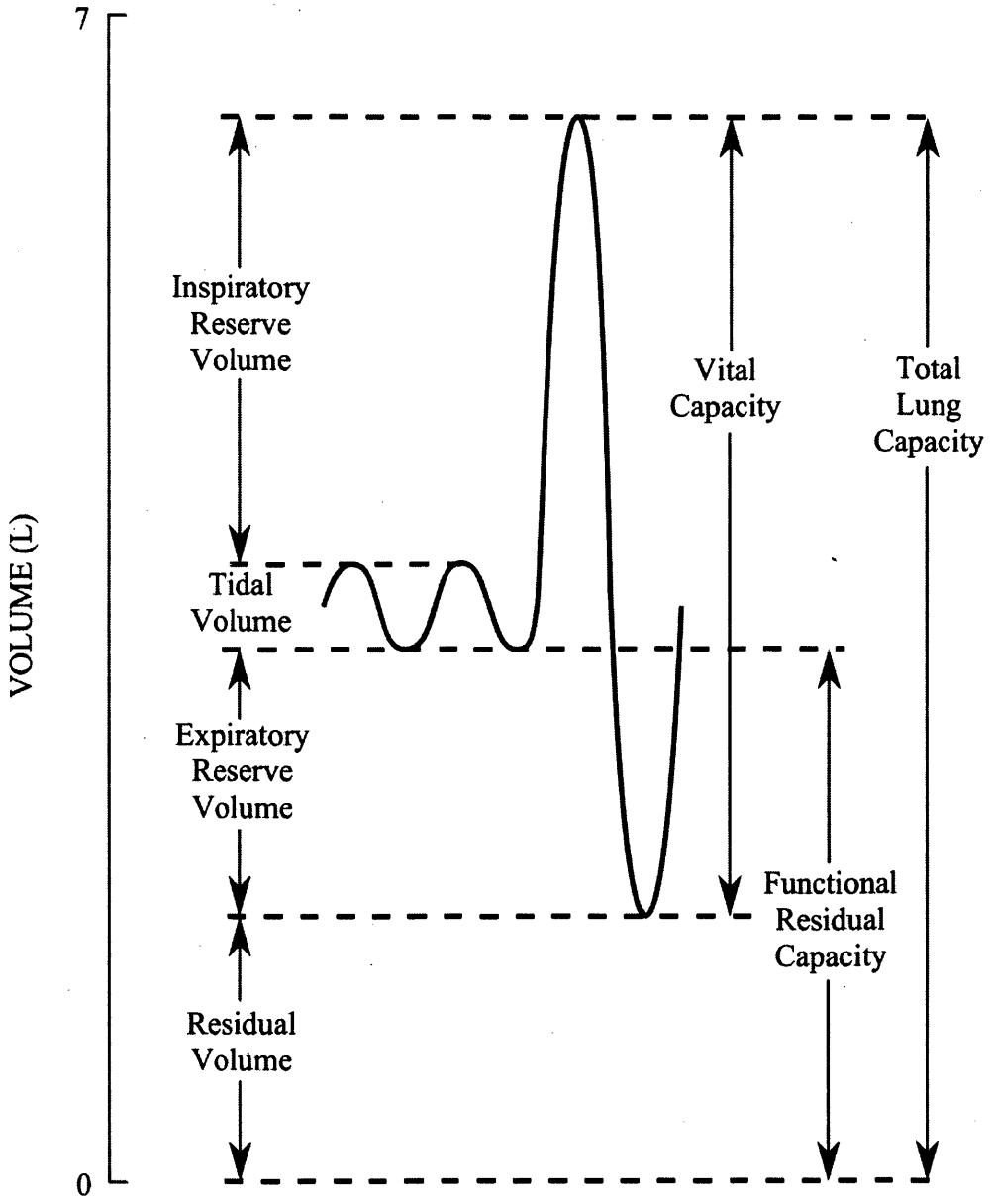

Figure 1.3: Lung volume definitions and capacities. This figure is adopted from ref. [5].

The cross sectional area of the airways increases moving downward from the trachea. From the trachea to the terminal bronchioles (about 19 generations) the cross sectional area increases from ~2.5 cm^2 to ~180 cm^2 [15]. This small increase in cross sectional area allows the flow to disperse rapidly through the many bifurcations to the lower airways. In the next four generations the cross sectional area increases from 180 cm^2 to 10,000 cm^2 [15]. This enormous and rapid increase in cross sectional area causes the flow to slow rapidly to speeds that are lower than that of diffusing molecules. The surface area of the alveoli reaches 75-100 m^2 [16]. It is this huge surface area and the thin blood-air barrier that makes the lungs an ideal delivery device.

1.2. STATE OF THE ART

Airflow and particle transport in the human airways has been studied for decades. Because of the complexities modeling human airway mechanics, studies have limited themselves to certain regions of the airways under simplified conditions with respect to geometry, boundary conditions, or heat and mass transfer properties/species. The development of computational capability over the past decades of study have allowed for the use of a more complex model with a greater degree of realism.

Many studies in the past have used the statistical models of Weibel *et al* [17] or Horsfield *et al* [8] and only modeled a few generations. Xia *et al* [18] studied airflow in a single bifurcation from generations G3-G4 with fluid structure interaction involving a model of parenchymal tethering (how the airways attach to surrounding tissue). Velocity patterns and wall shear stress were investigated to conclude that fluid flow is influenced by the deformation of the surrounding airways. Specifically, the larger cross sectional areas seen during inspiration produce flatter velocity profiles. In a recent study

performed by Zhang *et al* [19] airflow and particle deposition in a single asthmatic bifurcation was studied. It was found that airway diameter and the number of folds in collapsed airways affect the airflow, particle deposition, and pressure drop across the bifurcation. Fluid flow in an asymmetric double bifurcation model representing the trachea to generation G2 was studied by Nagels *et al* [20] using LES. Velocity and vorticity were considered to evaluate flow and turbulence under high frequency oscillatory flow. Fluid motion at the end of inspiration or exhalation (called pendelluft) was observed in the right main bronchus in this study. Comer *et al* [21-22] studied steady laminar airflow and particle transport in a double bifurcation model (generations G3-G5) with different carina shapes. Fluid velocity patterns and secondary motion were characterized, and particle deposition locations and overall deposition fractions were reported. Cross sectional flow asymmetry in the second bifurcation due to skewed flows was observed. This caused corresponding asymmetric particle deposition in the second bifurcation. At higher Reynolds numbers secondary flows played a significant role in particle deposition in the domain. The shapes of the carina were reported to have little influence on the overall deposition and a slight effect on local deposition.

To develop a more realistic inlet condition into the bifurcating airways and to study particle deposition, many studies have been performed in the airways above, and including, the trachea. Particle deposition of micro-particles and nano-particles was studied by Zhang *et al* [23] in a simplified model of the human upper airways (oral) and the first three bifurcations with different flow rates. Values for overall deposition fractions, deposition efficiencies, and deposition enhancement factors were reported. In this study deposition in the lower airways was found to be dependent upon particle size

distributions which in turn are dependent upon upstream deposition. The non-uniformity of particle deposition was found to be higher for larger particle diameters with micro-particle deposition highly non-uniform, nano-particle deposition more uniform, and with ultrafine particles depositing over a very large area. Longest *et al* [24] studied nano-particle deposition in a simplified model of the oral airways from the mouth to the trachea using both Lagrangian and Eulerian methods for particle tracking. This study also compared particle tracking models in a commercial software package to user defined models. Calculation of deposition fraction and deposition enhancement factors helped to characterize the differences in the built in and user defined models as well as the differences between the Lagrangian and Eulerian models. When compared to experimental studies the use of the Lagrangian model with the user defined models showed much better agreement than the built in models which stresses the importance of an appropriate Lagrangian particle tracking model. The Eulerian model also showed a similar degree of agreement with experimental studies; however the Lagrangian and Eulerian models still showed significant differences with each other, which was hypothesized to be due to slip corrections. Targeted drug aerosol delivery was studied by Kleinstreuer *et al* [25] in a simplified model of the upper airways from the mouth to generation G3 using a Weibel symmetric and asymmetric model. Particle termination locations were determined using a Lagrangian particle tracking method and the starting positions of those particles at the inlet of the oral airways were presented as release sites for drug aerosol targeting. A proof of concept experimental study was also performed in a physical reproduction of the computational airway model. Cross sectional particle distributions are presented to compare experimental and predicted particle transport

through the domain. Visually, the experimental data was reported to agree well with simulation data. The capture efficiency, which characterizes the percentage of particles reaching the prescribed target zone, varied greatly from 10 % to 100 % with higher values at low flow rates and lower values under normal breathing conditions. Secondary flows were found to play a significant role in the stretching and squeezing of the initial particle bolus released at the inlet. Xi *et al* [26] studied the effects of simplified models on particle deposition in the oral airway. Four models were generated: a realistic one directly from CT scans, one with elliptical cross sections, one with circular cross sections, and one with circular cross sections with a constant diameter. Deposition fractions, deposition locations, deposition enhancement factors, and particle profiles at the exit (trachea) were used to compare the four models. The best agreement of deposition fraction with other experimental studies was found with the realistic airway model, although the deposition fractions for all four models fell within one standard deviation of experimental data. Despite the agreement of the airway models with respect to overall deposition fractions, differences in the local deposition characteristics were found to be much more significant. Airflow and particle transport through a tube with a local constriction and a simplified model of the oral airways from the mouth to the trachea was studied by Zhang *et al* [27]. Comparisons were made between an LES turbulence model and three Reynolds averaged Navier-Stokes models: k-ω model, low Reynolds number k-ω model, and the shear stress transport transition model. Velocity and turbulence kinetic energy were evaluated and compared between the turbulence models and compared to experimental data. The general trend of the turbulence dissipation was similar between the tube with a local constriction and the oral airway model, but the oral airway model

had significantly more complex airflow structures. It was concluded that local constrictions were the dominant geometric feature responsible for producing turbulence. The standard k-ω model failed to capture laminar behavior at low Reynolds numbers, while little difference was found between the other three models. The ability of LES to capture instantaneous velocity fluctuations was hypothesized to be important for modeling mico-particle transport.

In recent years, due to advancements in medical imaging equipment and techniques, studies have begun to use geometries based on CT scans of patients. Choi *et al* [28] studied airflow through geometries created from the CT scans of two patients from the mouth to generation G7. Velocities, turbulence kinetic energy, and turbulent coherent structures were compared between the subjects to assess inter-subject variability. It was concluded that airflow structures at similar flow rates were only qualitatively similar and the differences in flow characteristics between the subjects was attributed to the glottal aperture area and the shape and orientation of the trachea. Simulations were also run in the geometry of one patient with the complete model and three models at different truncation levels to investigate intra-subject variability. Truncated geometries resulted in the absence of some of the major airflow structures. Careful analysis of proposed improved boundary conditions for the truncated geometries showed solutions that were closer to those obtained with the full geometry. Inthavong *et al* [29] studied airflow and micro-particle deposition in a model generated from CT scans of a patient from the trachea to generation G5. Two breathing conditions were applied at the inlet: the first half a sinusoidal waveform over 2 seconds with a peak inspiratory flow rate of 90 L/min with a 2 second breath hold immediately after, and 5 cycles of a

sinusoidal waveform over 10 seconds (2 seconds per cycle) with a peak inspiratory flow rate of 30 L/min. Fluid flow was characterized with velocity contours and secondary flows vectors at slices throughout the domain. Secondary flow vortices were seen in the domain and were stronger during inspiration. Deposition fractions were used to characterize the particle depositions for both breathing conditions. Increased deposition fractions were reported for the breathing condition with the higher flow rate and breath hold. Analysis of the deposition patterns revealed that the breathing condition with the breath hold and higher flow rate increased deposition in the first few bifurcations instead of in the lower generations. Fluid flow and particle deposition was studied by Xi *et al* [30] in a model from CT scans with and without a larynx. Fluid flow was characterized with velocity profiles, and turbulence viscosity ratios as well as velocity contours, and secondary motion vectors in slices through the domain. The laryngeal jet was found to cause a large region of recirculating flow in the trachea and to generate turbulence. Particle deposition was characterized with particle deposition locations, particle deposition fractions, particle deposition enhancement factors, particle trajectories, and cross sectional particle profiles. The larynx was shown to be important for modeling fluid flow and particle transport in the upper airways causing a decreased deposition at the carina of the first bifurcation and the first three bronchi, increased deposition in the trachea, and increased particle transport to the lower airways of the model. In a recent study by Lambert *et al* [31] fluid flow particle deposition was studied in a CT scan based model of the airways from the mouth to generation G7 using large eddy simulation for a steady inlet condition. An assessment of velocity, and turbulence kinetic energy, particle deposition locations, deposition fractions and efficiencies, and particle transport profiles

showed that the laryngeal jet was a great influence in particle impaction and dispersion. The left lung was found to have grater deposition which was thought to be caused by airway geometry and influences of the laryngeal jet flow in the trachea.

Before the widespread availability of high computing power, experiments were often more useful in the study of fluid flow and particle deposition in the human airways. In recent years the number of experimental studies being performed has dropped but there is a great deal of insight yet to be gained from experimental studies and with advancements in computational model realism there will be an increased importance for experimental data for validation and for setting realistic boundary data. Große *et al* [32] experimentally studied airflow in a silicone cast of generations G0-G6. PIV was used with hydrogen bubbles in a water glycerin mixture to take measurements of the flow field. Velocity vectors and contours, vorticity contours, and an analysis of vortical structures were presented to carefully study the flow in the first bifurcation. Vortical flow structures were found to depend strongly on the Reynolds number and Womersley number. Fully developed flow was not seen in any of the bronchial generations, indicating the importance of ensuring proper flow rate distributions. Transient evolution of bronchial flows was observed under oscillating flow conditions that would not otherwise be captured with steady state analyses. In an experiment by Zhang *et al* [33] the effects of cartilaginous rings on particle deposition was studied in two simplified models from the mouth to generation G3 with a symmetric in plane triple bifurcation: one with a representation of cartilaginous rings, and one without. Particle deposition was measured by determining the increase in mass of the filters that were placed at the outlets to capture particles. Deposition fractions and deposition efficiencies were presented.

The inclusion of cartilaginous rings was found to greatly increase the deposition efficiencies. Experiments were performed by Fresconi *et al* [34] in a symmetric planer triple bifurcation model under oscillatory flow conditions. PIV measurements were made using fluorescent particles in a glycerol-water solution to collect data on secondary flow velocities. Centrifugal forces were shown to trigger secondary flows including Dean vortices due to the curvature in the airways. It was hypothesized that Dean vorticies may be present up to generations 10-13 depending on inspiratory flow conditions. Due to the repeated interruption of flow development by each new bifurcation secondary flow velocities did not exceed 20 % of the primary flow velocities in the airways. In addition, local curvature was found to have a greater effect on secondary flows than the propagation of flow fields from higher generations. Kim *et al* [35] studied particle deposition in a symmetric planar double bifurcation and a symmetric double bifurcation with the second bifurcation oriented 90° out of plane. Particle depositions were determined by dissolving deposited uranine particles in water and measuring the concentrations with a fluorometer. The model was divided into several sections and filters were placed at the outlets so that regional deposition efficiencies could be determined. Valves were also placed at the outlets so that the flow distribution could be adjusted. Deposition fraction and deposition efficiency values showed that the angular position of the bifurcations as well as the flow distributions had a significant impact on region particle deposition.

1.3. MECHANICAL VENTILATION AND AEROSOLIZED DRUG DELIVERY

Mechanical ventilation is a mechanical means to assist or replace a patient's natural breathing. It is now the most commonly used mode of life support in medicine

[36]. Mechanical ventilation is used when a patient's natural breathing is not sufficient to deliver oxygen to the bloodstream. Common indications for mechanical ventilation include acute lung injury (ALI), acute respiratory distress syndrome (ARDS), acute respiratory failure (ARF), acute exacerbation of chronic obstructive pulmonary disease (COPD), severe asthma, cystic fibrosis, pulmonary edema, pulmonary embolus, coma, drug overdose, neuromuscular disorders, and others [37-39]. Many diseases which require drug treatment are also indications for ventilation such as COPD, ARDS, and severe asthma [5]. For this reason it is logical to deliver drugs directly to the lungs in aerosolized form while undergoing mechanical ventilation treatment. The use of pharmaceutical aerosols is advantageous for several reasons. The surface area of the lung epithelium available for drug absorption is very large (75-100 m^2) which is much greater than that of the gastro-intestinal (GI) system [5]. In addition the epithelium is very thin (0.5 μm) which allows for rapid drug absorption [14]. Unlike ingestion, the blood will flow to the rest of the body before passing through the liver. When considering the application of systemic drugs, injection is used more frequently than inhaled aerosols for drug delivery. However in recent years the use of inhaled drug aerosols for systemic delivery has also increased and it has shown improvement even over subcutaneous injection of insulin [40]. Continued advances in drug aerosol delivery may make the lungs a more viable delivery method.

The effectiveness of pulmonary drug delivery under mechanical ventilator conditions is dependent on a number of factors [41-42] that are itemized below:

(a) **Ventilator related**: Ventilation mode, tidal volume, respiratory rate, duty cycle, inspiration waveform and breath-triggering mechanism

(b) **Circuit related**: Endotracheal tube size, humidity and density of inhaled gas

(c) **Device related**: Type of device (nebulizer, metered dose inhaler, or dry powder inhaler), fill-volume, gas flow, cycling (inspiration vs. continuous), duration, and timing of actuation

(d) **Drug related**: Dosage, formulations, particle size, targeted site for delivery and duration

(e) **Patient related**: Age, ethnicity, severity of airway obstruction, mechanism of obstruction, presence of dynamic hyper-inflation and patient ventilator synchrony

The objective of this study is to explore the ventilator related effects on pulmonary drug delivery. Specifically we focus on the waveforms of the respiratory cycle as they are easily adjusted on modern ventilators. In this study, the focus is on the model of a single patient and not intra-subject variability. For this reason the factors that fall into the patient related category will not be discussed further.

Mechanical ventilation can be lifesaving, but there are also risks and potential complications associated with mechanical ventilation. These risks and complications include but are not limited to: infections, obstructions, ventilator induced lung injury (VILI), and damage to the trachea due to the endotracheal tube or airtight cuffs. VILI is actually a set of conditions that can be caused by volutrauma (damage to the lungs due to over-inflation of the lungs), barotrauma (damage due to excessive pressures), atelectrauma (damage from repetitive opening and collapse of distal airways), or biotrauma (severe inflammation of the lungs) [43]. In addition if the ventilation is not

properly controlled then the pH levels of the blood may increase (respiratory alkalosis) or decrease (respiratory acidosis) [5].

1.3.1. Ventilation Management Techniques. Mechanical ventilators can be separated into two main groups: (a) negative pressure ventilators, and, (b) positive pressure ventilators. Negative pressure ventilators create suction outside of the thoracic cavity which creates a pressure differential that causes air to move into the lungs. Positive pressure ventilators push air into the lungs by creating a higher pressure in an endotracheal tube, or outside the nose or mouth causing air to flow into the lungs. The use of negative pressure ventilators has decreased dramatically and they are rarely seen in use at modern hospitals [44]. This study does not focus on negative pressure ventilation. It is important to note, however, how positive pressure ventilation is different from normal breathing [45].

Normal breathing is controlled by a set of muscles and the natural compliant properties of the lungs. Muscles in the thoracic cavity (most notably the diaphragm muscle) work to expand the lungs. The expansion of the lungs causes a decrease in airway pressure and the pressure differential between the airway pressure and the ambient (external) pressure is what drives the flow of air into the lungs during inspiration. During exhalation the muscles relax and allow the lung to return to its natural size. This process is passive and is driven by the natural elasticity of lung tissue. The pressure in the airways increases and the pressure differential between the airway pressure and the ambient pressure is what drives the flow of air out of the lungs.

Some patients are unable to produce any respiratory effort and the ventilator must provide the total effort of breathing. This type of ventilation is known as controlled

mechanical ventilation (CMV) and is used for patients that are, for example, comatose, or on anesthesia [36]. Other patients are able to produce some respiratory efforts, however their efforts are not sufficient to supply oxygen properly, or their efforts are not consistent. This type of ventilation is called assisted mechanical ventilation (AMV) and the ventilator input is triggered by the patient's inspiratory effort based on a measurement of flow or pressure. It is common for ventilators to offer an assist-control mode, where the ventilator will assist when inspiratory effort is detected and deliver a controlled breath when inspiratory effort is absent, usually based on a time trigger [36].

Traditionally, there are four phases of the ventilator cycle: trigger, delivery, cycle, and expiration [36]. The trigger phase marks the onset of inspiration. Even under CMV there is some trigger that initiates inspiration such as flow or time. Triggers are generally based on time, flow, or pressure. After the trigger has been set a breath is delivered by the ventilator. There are many risks involved with improper breath delivery (discussed above) so the inspiratory waveform must be precisely controlled. The delivery phase will be discussed further in §1.3.2. The cycle phase marks the end of inspiration and the onset of exhalation. The cycle phase is generally detected by measurements of pressure, volume, time, or volumetric flow rate. The expiration phase is a passive process of allowing the natural elasticity of the lungs to force air out of the lungs [46]. This phase closely resembles expiration during natural breathing with the exception of additional flow resistance due to the ventilator circuit [47]. Expiration is allowed to occur naturally until the next trigger phase which marks the beginning of the next breath cycle [47].

1.3.2. Ventilation Waveforms The artificial breathing during positive pressure mechanical ventilation needs to be carefully controlled to avoid VILI but still maintain

proper ventilation of the alveoli. In addition many patients require a constant positive pressure to keep the airways from collapsing [47]. This is known as positive end expiratory pressure (PEEP). Ventilation waveforms are generally controlled by pressure, volume, or volumetric flow rate. One of these variables controls the shape of the waveform, however there are usually limits set on the other variables to avoid lung injury. Typically the lungs are modeled as an elastic container with some resistance to flow. The three variables, pressure, volume, and flow, are related to each other by the following equations:

$$P = \frac{V}{C} + QR \tag{1.3}$$

$$Q = \frac{dV}{dt} \tag{1.4}$$

where V is the volume of air above the functional residual capacity, P is the airway pressure above PEEP, and Q is the flow rate. The parameter C is the lung compliance which is the multiplicative inverse of the lung elasticity. Compliance represents the average slope of the pressure-volume diagram and is defined as:

$$C = \frac{\Delta V}{\Delta P} \tag{1.5}$$

The airway resistance, R, which represents the average slope of the pressure flow diagram and is defined as:

$$R = \frac{\Delta P}{\Delta Q} \tag{1.6}$$

Although, lung compliance (C) and airway resistance (R) are not constant for a given patient nor throughout a complete respiratory cycle, it is a common assumption to consider them to have a constant value when evaluating waveform patterns [48].

Ventilators can be classified into three types depending on what variables they use to control the inspiratory waveform. Although it is very common for a ventilator to offer different types of control it cannot simultaneously control all three variables (pressure, volume, and flow) [47]. A pressure controller will set the delivered pressure throughout inspiration though this set pressure need not be a constant pressure. The flow rate and volume throughout the cycle depend on the airway resistance and compliance as can be seen in Equation 1.3. A volume controller will set the volume of air delivered throughout inspiration. There are ventilators that integrate flow measurements to determine volume, but a true volume controller will measure volume by the displacement of a piston or bellows and use this measurement to control breath delivery [47]. Because flow is the time derivative of volume and there are no other constants involved (Equation 1.3), the flow is also determined when the volume is set. The, pressure, however will depend upon the airway resistance and compliance as can be seen in Equation 1.2. A flow controller will set the flow of air throughout inspiration. The volume is the integral of flow with no other constants involved which can be seen in Equation 1.3. This means that the change in the volume of the lung from the volume at the onset of inspiration will also be determined when the flow is set. Therefore if the functional residual capacity remains constant each cycle, then the same flow waveform will produce the same volume

waveform regardless of changes in lung compliance and airway resistance. The pressure throughout the inspiration phase for a flow controller will depend on the lung compliance and airway resistance as can be seen in Equation 1.2.

Pressure control is considered to be more protective ventilation strategy than volume or flow control, but because the volume depends on the compliance and resistance there is no guarantee that the degree of ventilation will be sufficient or necessary [36]. Volume and flow control will deliver a set amount of air to the lungs, but because pressure depends on the compliance and resistance there is a higher risk of barotrauma or airway closure. When set up properly, volume control, flow control, and pressure control will be equally sufficient in providing gas exchange, hemodynamics, and pulmonary mechanics [36].

The effect of the waveforms on pulmonary drug delivery may be more significant than the effects on alveolar ventilation. The aerosolized particles suspended in the flow are not the same density as the flowing air and will not simply follow along with the flow. Fluid flow characteristics influence the degree and location of particle deposition [49]. The speed of the flow will have a direct influence on particle deposition and there are additional influences due to turbulent eddies in the domain.

1.3.3. Aerosolized Drug Delivery Mechanical ventilation is meant as a temporary intervention to assist in breathing but does not cure any underlying disease [50]. Aerosolized drug delivery can help to keep the airways fit for oxygen delivery and carbon dioxide expulsion, and can help to treat the underlying conditions. It is also being used for insulin delivery, pain management, cancer therapy, and nanotherapeutics [14].

There are several commonly used drug aerosol treatments. Bronchodilators are used to open airways in patients with asthma and chronic bronchitis [5]. In general they are used to relax the muscles in the rings around the airways causing the airways to widen. Corticosteroids are used to reduce inflammation in airways for patients with asthma or emphysema [5]. Aerosolized antibiotics are used to treat broncho-pulmonary infections and are especially useful for patients with cystic fibrosis, who are susceptible to pulmonary infections [51]. Ipratropium bromide is used to reduce the production of mucus in chronic bronchitis [52]. Mucolytic agents are used to reduce the viscosity of mucus for patients with COPD [5]. This will make mucus clearance easier and reduce the obstructions in the airways. Insulin therapy is also being considered as an aerosol therapy that has shown improvement over traditional subcutaneous injection [40].

Drug aerosols are delivered by one of three devices: nebulizers, metered dose inhalers (MDI), or dry powder inhalers (DPI). Nebulizers are a device to aerosolize liquid medications. There are three types of common nebulizers: (a) jet nebulizers, (b) ultrasonic nebulizers, and, (c) vibrating mesh nebulizers. Jet nebulizers use a jet of air that entrains liquid medications. The entrained fluid thins out in the air stream until it forms instabilities. These instabilities continue to stretch and thin until breakup occurs. The particles form due to surface tension [42]. The airstream is passed by a baffle that causes larger particles to impact and move to the walls while smaller particles will flow past. The air jet required for these nebulizers can come from compressed air or can be generated by an electric compressor. These devices tend to be bulky and must have a source of compressed air or electricity depending on the model.

Ultrasonic nebulizers use a piezoelectric at the bottom of the liquid medicine reservoir to create ultrasonic vibrations in the liquid. The vibration waves travel to the surface where instabilities occur. The instabilities grow, stretch, and thin until particle breakup occurs. The particles form due to surface tension. These devices require a source of electricity. In ultrasonic and jet nebulizers particles that are small enough to be suspended in the airstream are passed out of the nebulizer to the ventilator circuit to be delivered to the patient. Particles that are too large will drop down into the medication reservoir or collect on the walls and be recycled. Vibrating mesh nebulizers use a mesh attached to a piezoelectric. The mesh is full of tapered holes that act as micro pumps as the mesh vibrates. As the mesh moves into the fluid, the fluid is forced through the holes forming tiny droplets. These devices require electricity but can be battery powered [42]. Unlike jet and ultrasonic nebulizers, vibrating mesh nebulizers do not recycle aerosolized medication [53]. These devices require precision holes which can increase cost. In addition they may be difficult to disinfect. Metered dose inhalers (MDI) are portable drug delivery devices that are specifically designed to deliver a precise dose to the patient. They are comprised of a canister, a propellant, medication (either liquid or particles suspended in liquid), a metering valve, and an actuator. The canister contains the medicine formulation and the propellant. When actuated, the propellant will force the drug formulation through the metering valve which controls the dose. The formulation will begin to expand and boil. Liquid ligaments will form and will be ripped apart by aerodynamic forces forming particles [54]. The patient's breath must be synchronized with the actuation to achieve proper delivery. The propellant causes the aerosolized medicine to leave the device at a high velocity which can cause a high degree of

deposition in the oropharynx. Spacers are commonly used to allow the aerosol spray to decelerate and mitigate this deposition to encourage more aerosol transport to the lower airways. Dry powder inhalers use the inspiratory effort of a patient to deliver a suspension of dry powder. The flow of air through the device is produced by the patient and causes the powder to be sucked up into the airstream. Once in the airstream, the dry powder particles will continue to break up, or disaggregate. Higher flow rates will increase the rate of particle pickup and aggregation, but also may cause a high degree of deposition in the oropharynx [42]. Some models will measure out a set dose before inhalation but others will rely on the rate and length of inspiration to pick up the correct dose.

There are several advantages and disadvantages to the different drug delivery devices and maximizing the effectiveness of treatment depends on the choice of delivery device. Nebulizers have the ability to aerosolize a variety of drug solutions including drug mixtures but can only aerosolize liquids and does not aerosolize suspensions well [14]. MDIs have the ability to aerosolize liquid medications and solid suspensions, however, DPIs can only aerosolize dry powders and are particularly susceptible to moisture. Nebulizers utilize normal breathing so they can be used for patients that may be very young, very old, debilitated, or distressed. DPIs and MDIs require hand breath coordination and require that the patient have control of their breathing. The determination of emitted dose is easiest for a MDI and does not depend on inspiratory effort. It is difficult to determine how much of a nebulizer's dose is lost during expiration, recycled, collected on the walls, and how much is lost from leaks that may occur around a mask. The dose given by a DPI is dependent on the patient's inspiratory

effort and a single dose is not measured out in all models. In addition not all models of DPIs have a dose counter and most MDI models do not. MDIs and DPIs are highly portable; however the MDI is slightly less portable with a spacer. Nebulizers have problems with portability due to their size and the requirement of a power source, and are often noisy. Maintenance for DPIs and MDIs are much lower than that of a nebulizer. High deposition in the oropharynx can occur when using a DPI with improper breathing or when using a MDI without a spacer. Nebulizers have the longest treatment times of all three of the delivery devices. MDIs and DPIs have comparable treatment times that are significantly shorter than nebulizers [42]. The cost of these devices depends on the specific drug formulations as well as the duration of use, and other factors. In general, however, nebulizers tend to be the most expensive, with DPIs being more expensive than MDIs [14].

When a patient is undergoing mechanical ventilation treatment it is very common to deliver aerosolized medication with a MDI or a nebulizer. In recent years, MDIs have become more popular than nebulizers for the delivery of bronchodilators [41]. The use of DPIs during mechanical ventilation is feasible, but has potential complications with the ventilator circuit and humidity, and their efficacy has not been well demonstrated in a clinical setting [55]. Further study of aerosol drug delivery may increase the occurrence of DPIs use for patients undergoing mechanical ventilation treatment. After the aerosolized medications have left the drug delivery device the next important step is to determine where it will land. The goal of drug delivery is to ensure the medications traverses the path from their release points to the site that will maximize their medial effectiveness. This is known as targeting whether the delivery site is local or systemic

[14]. Determining where a particle deposits hinges on understanding the mechanisms that cause deposition.

There are three primary deposition mechanisms: (a) impaction, (b) sedimentation, and, (c) diffusion. Impaction is an inertial effect. Due to drag forces a particle will naturally tend to move with the flow. However, if the flow changes suddenly, for example due to an obstacle, the particle will take some time to respond to the changes in the flow. A characteristic time for an aerosolized particle to respond to flow changes has been defined as:

$$\tau_p = \frac{\rho_p d_p^2}{18\mu} \tag{1.7}$$

where, τ_p is the particle's characteristic time, ρ_p is the particle density, d_p is the particle diameter, and μ is the dynamic viscosity. A particle in the flow will only have so much time to adjust to the new flow before impacting on the obstacle. A characteristic time needed for a particle to adjust to the flow, known as the hydrodynamic time has been defined as:

$$\tau_h = \frac{D}{C_c u} \tag{1.8}$$

where, τ_h is the hydrodynamic time, D is the airway diameter, C_c is the Cunningham correction factor (a factor that accounts for non-continuum slip effects, see § 3.2 for a more detailed discussion), and u is the fluid velocity. Together the characteristic time for

a particle to adjust to flow changes and the hydrodynamic time characterize the Stokes number which is defined as:

$$\mathrm{St} = \frac{\tau_p}{\tau_h} = \frac{\rho_p d_p^2 C_c u}{18 \mu D} \tag{1.9}$$

The Stokes number is used to classify the degree of inertial impaction [56]. If the particle's inertia is too high it will deviate from the flow and may deposit on the obstacle by impaction. The most common obstacle in the lungs is a bifurcation. The flow will suddenly split and turn. If the particle inertia is too high it will deposit on, or near, the carina by impaction. This deposition mechanism is most dominant for larger particles in the upper airways where air velocities are highest. Sedimentation is a gravitational effect [57]. The aerosolized particles have a much higher density than the air. This will cause the particles to "sink" in the airstream. This deposition mechanism is most dominant for heavier particles in the more distal airways where the velocity is low and particle residence times are high [5]. The ratio of the gravitational force to the buoyant force is equivalent to the ratio of the particle and fluid densities. Diffusion as a deposition mechanism refers to the movement of the aerosolized particles due to random collisions with gas particles [57]. This can be described as a Brownian diffusion which depends upon the Brownian diffusivity and the energy of the gas. The Brownian diffusivity is defined as:

$$\tilde{D} = \frac{k_b T C_c}{3 \pi \mu a_p} \tag{1.10}$$

where, k_B is the Boltzmann constant, and T is the absolute temperature of the fluid. This deposition mechanism is most dominant for very small particles in the lower airways where fluid velocities are low and particle residence times are high.

Turbulence can also greatly increase particle dispersion. The turbulent mixing will cause the particles to spread more quickly which can be viewed as increased diffusion [58]. Turbophoresis is an effect that causes particles with inertia to be transported from regions of higher turbulence intensity to lower turbulent intensity [58]. Turbulent dispersion and turbophoresis are expected to have an effect on particle transport and deposition in regions with high turbulence, and also may create particle distributions in the domain that are more favorable for deposition by the other particle deposition mechanisms.

2. COMPUTATIONAL DOMAIN

Proper formation of the computational domain is critical to obtaining a useful solution. Important features that are left out or poorly modeled could fundamentally alter dominant flow features. Care was taken to how the geometry was generated, corrected, and modified. An appropriate mesh type was selected and fit to the geometry. In addition, detailed studies were performed to ensure a grid independent solution which will be discussed in Chapter 4.

2.1. GEOMETRY

The human airways are a complicated structure to model. The airways have a large range of sizes, they are numerous, and they are intricate [59-60]. Even under normal breathing conditions the airways change size and shape [61]. It is not computationally feasible to run detailed simulations on a complete set of human airways [62]. The current study focuses on the tracheobronchial region.

2.1.1. State of the Art. There have been several computational studies that have modeled the human airways [63-65]. Some attention has been given to the study of a single bifurcation [18-19, 63, 66-68]. While there is much to be learned from the study of a single bifurcation a greater degree of detail is needed to gain more useful insight into the problems of airflow throughout the respiratory system.

In the past studies have typically used one of two methods for generating more complex airway geometry: (a) computer generation of an idealized statistical model; or, (b) computer reconstruction of computer tomography (CT) scans from hospital patients. The two most widely used statistical models were created by Weibel *et al* [17] and Horsfield *et al* [8, 16]. The model developed by Weibel *et al* is a symmetric model that

specifies lengths and diameters of airways based on generation number. However one of the most prevalent characteristics of the upper airways is their asymmetry. Horsfield *et al* [8] proposed a model that specified the length and diameter of airways based on order, i.e. the number of converging branches from the most distal branch (i.e. the respiratory bronchioles). The most distal branch was considered to be of order 1. When two branches would converge the parent branch would take the order of one more than the maximum of the orders of the converging branches. The model created by Horsfield *et al* [8] also accounted for average asymmetry of the regions of the lungs. Both the Weibel and Horsfield models assume the airways of the lungs to be straight and cylindrical. However, the airways of the human respiratory system are neither entirely straight nor entirely cylindrical. In addition the models do not account for the orientation of the airway bifurcations. The models are both statistically based and do not account for a patients physical characteristics (height, weight, race, etc.) nor do they account for a patient's medical history (disease, injury, etc.); all of which are expected to significantly vary the pulmonary geometry.

Computed tomography (CT) scans are a medical imaging technique that uses an X-ray emitter and detector on opposite sides of a spinning drum to collect three dimensional data from a patient. Modern medical imaging techniques such as CT scans have made it possible to take detailed measurements of patient's specific airway geometries. These measurements, combined with medical imaging processing software, such as Materialize® Mimics®, have made it possible to reconstruct a computer model of the airway geometry. Several studies have taken advantage of these innovations and CT scan reconstruction techniques have been applied to the current study [31, 69-73].

2.1.2. Geometry Creation. CT scans will produce data that represents the topology of a three dimensional space. The data is presented as a set of two dimensional slices in the patient's axial (transverse) planes (refer to Figure 2.1). Each two dimensional slice is a set of grayscale values; one for each pixel in the slice. The grayscale values are measured in Hounsfield units (HU). When represented as a three dimensional array, the scanned volume is broken into cells called voxels, each having a dimension of pixel size × pixel size × slice increment. This data was stored as DICOM (Digital Imaging and Communications in Medicine) files. The geometry creation process involves three major steps: (a) volumetric reconstruction, (b) segmentation, and (c) geometry cleanup. Volumetric reconstruction involves lining up the two dimensional scan planes on top of each other to create the volume of voxels and selecting a set of voxels based on grayscale values that are likely to contain a target material. Segmentation involves cutting voxels from the set of voxels produced from volumetric reconstruction that are not contiguous or that do not actually contain the targeted material. This step relies on intuition and is generally performed manually. Geometry cleanup is the process of removing defects in the reconstructed model due to the representation of the geometry by voxels (blocks) and the adjustment of surface geometries to allow implementation of boundary conditions.

For the current investigation, CT scans were taken of a 57 year old, male, patient undergoing mechanical ventilation treatment at the University of Missouri at Kansas City (UMKC) hospital, using a Siemens SOMATOM Definition AS 128 slice CT scanner. There are several metrics that determine the quality of a CT scan such as: field of view, resolution, pixel size, slice increment, and pixel depth. The field of view was

approximately 34 cm and covered the entire lung. The resolution of each scan was 512×512 pixels with a pixel size of about 0.7×0.7 mm^2 and a slice increment of 3 mm. Images were taken at a pixel depth of 12-bit grayscale.

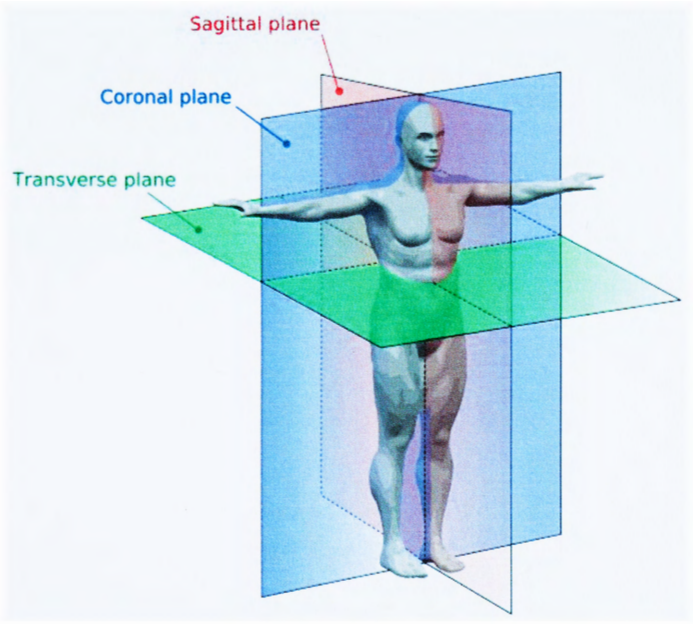

Figure 2.1: Anatomical planes [74]

The DICOM files were imported into Materialize® Mimics® software for volumetric reconstruction and segmentation. A threshold operation was performed to extract a set of voxels with grayscale values in a selected range of HU. A region growing operation is an operation where a single voxel from a primary set is selected and placed into a secondary set. Any voxel in the primary set that is adjacent to a voxel in the secondary set will be added to the secondary set. This process is repeated until no new voxels are added to the secondary set. A region growing operation was performed on the

set of voxels that had undergone the threshold operation to obtain a continuous set of voxels. The "calculate 3D" operation in Mimics® was used to reconstruct a continuous volume of air within the lungs.

Figure 2.2 shows a screenshot from Mimics® software. The upper right view shows a slice of the axial plane (the plane in which the CT scans were taken) where the main bronchi can be seen. The upper left view shows a slice in the coronal plane which is constructed by Mimics® from the data in the axial slices. The coronal view has a clear image of the first bifurcation. The bottom left view is a slice in the sagittal plane which was also constructed by Mimics® from the data in the axial slices. In the sagittal view the trachea can be seen as well as an edge of the endotracheal tube. There are two active masks shown in the CT scan views. The green mask is the initial thresholding region. The yellow mask is what was generated after the first region growing operation. The bottom right view shows the three dimensional reconstructed volume after the first region growing operation.

The data acquired by the CT scan process represents a measurement of average attenuation coefficient for X-rays over the voxel volume. In general each type of tissue will have a small, distinctive range of HU values. Ideally a voxel would only contain one type of tissue. However, the degree of resolution for this to occur is not attainable with current imaging techniques. For this reason a voxel that is mostly air may fall within the threshold range. Towards the lower region of the lungs the airways and alveolar sacs become so close together that several voxels fall within the threshold region. This means that a voxel that contains several small airways may be viewed as empty space. This kind of false positive known as the tissue fraction effect can cause volume leakage for the

reconstructed volume and necessitates the segmentation process [75]. This volume leakage can be seen clearly in Figure 2.2.

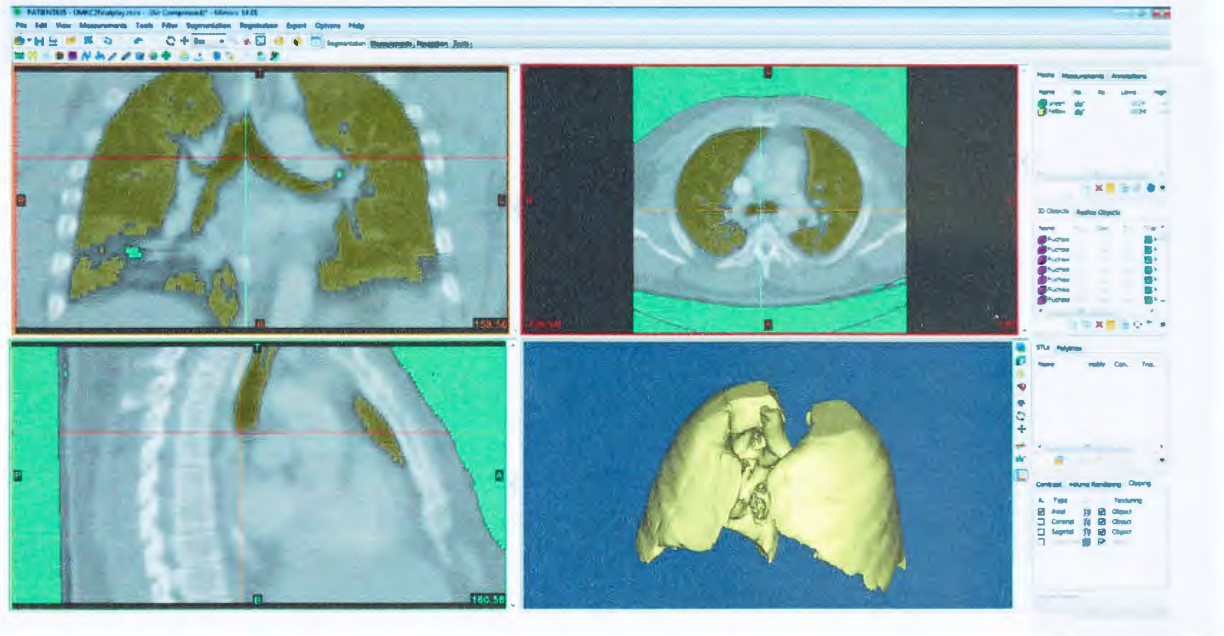

Figure 2.2: Mask and 3D volume after thresholding and region growing. View from Mimics® software. Upper left: coronal view plane, upper right: axial view plane, lower left: sagittal view plane, and lower right: 3D view.

Segmentation was performed on the reconstructed volume to remove under-resolved branches of the lung model. By carefully removing voxels from the mask (a set of colored pixels displayed in each of the three directional planes in Mimics® software) of the reconstructed volume the under-resolved regions were essentially cut off of the tracheobronchial region. A second region growing operation was performed to extract the rough airways of the computational domain. The extracted (unsmoothed) volume can be seen in the bottom right view of Figure 2.3 along with its mask in the CT scan views.

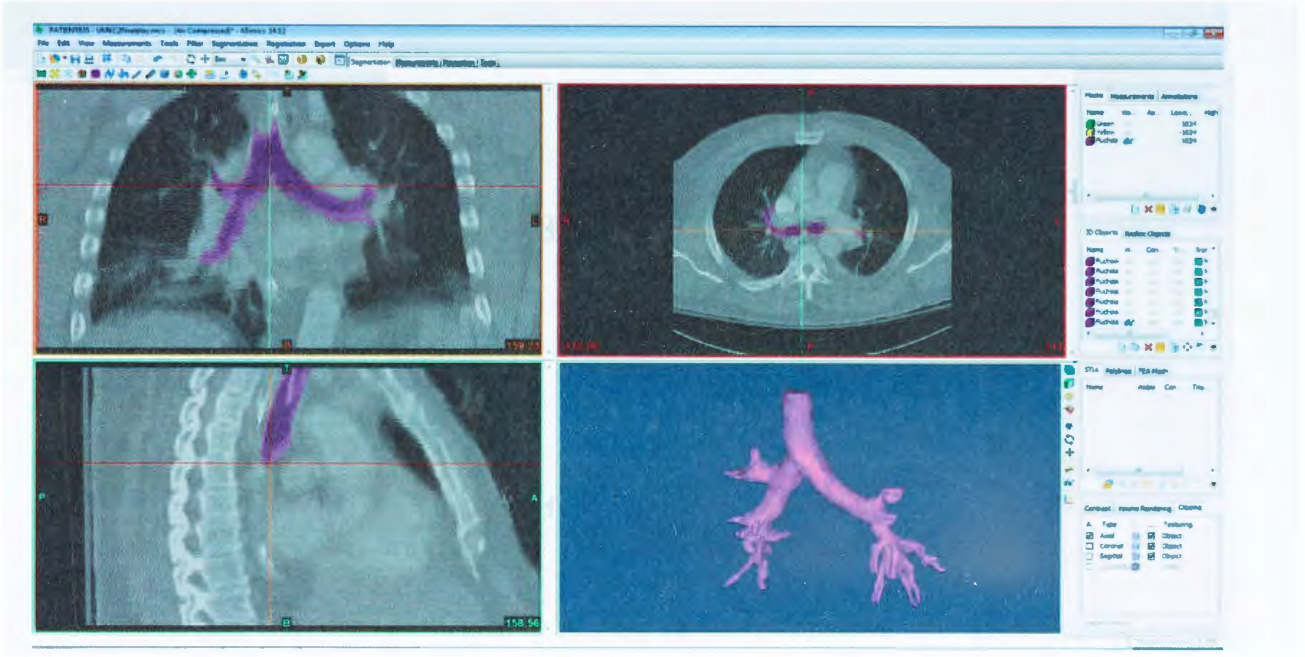

Figure 2.3: Mask and 3D volume after segmentation. View from Mimics® software. Upper left: coronal view plane, upper right: axial view plane, lower left: sagittal view plane, and lower right: 3D view.

After segmentation the model is a set of voxels that make up the large airways of the respiratory system. The voxels are rectangular prisms, and the volume represents space that air would flow through in the lungs. Geometry cleanup is necessary to create a more organic (smooth) surface and to establish inlets and outlets for air to flow through [69, 76]. An additional goal of geometry cleanup is to prepare the domain to accept boundary conditions that are realistic and can be numerically specified while setting up the computational fluid dynamics (CFD) simulations.

A smoothing operation was performed on the model using Mimics® software and it was exported from Mimics® as an STL (stereolithography) file using the STL+ module. As an STL file the geometry is represented by a set of nodes on the surface of the volume and a set of faces made up of three nodes each to approximate the surface.

The STL file was imported into Blender® 2.5 and further smoothing was performed. A set of faces were selected for each outlet and were projected onto a plane at the end of the airway perpendicular to the airway the outlet belonged to. To ensure appropriate outlet conditions extensions were added to each outlet. An extension was created at each outlet by extruding the projected faces parallel to the airway and gradually transitioning the airway shape to a circle. A similar process was performed at the inlet of the endotracheal tube to ensure an appropriate inlet condition. The finished geometry was exported from Blender® as an STL file. The completed geometry, after smoothing, adding extensions, and defining the openings for the inlet and outlets is shown in Figure 2.4.

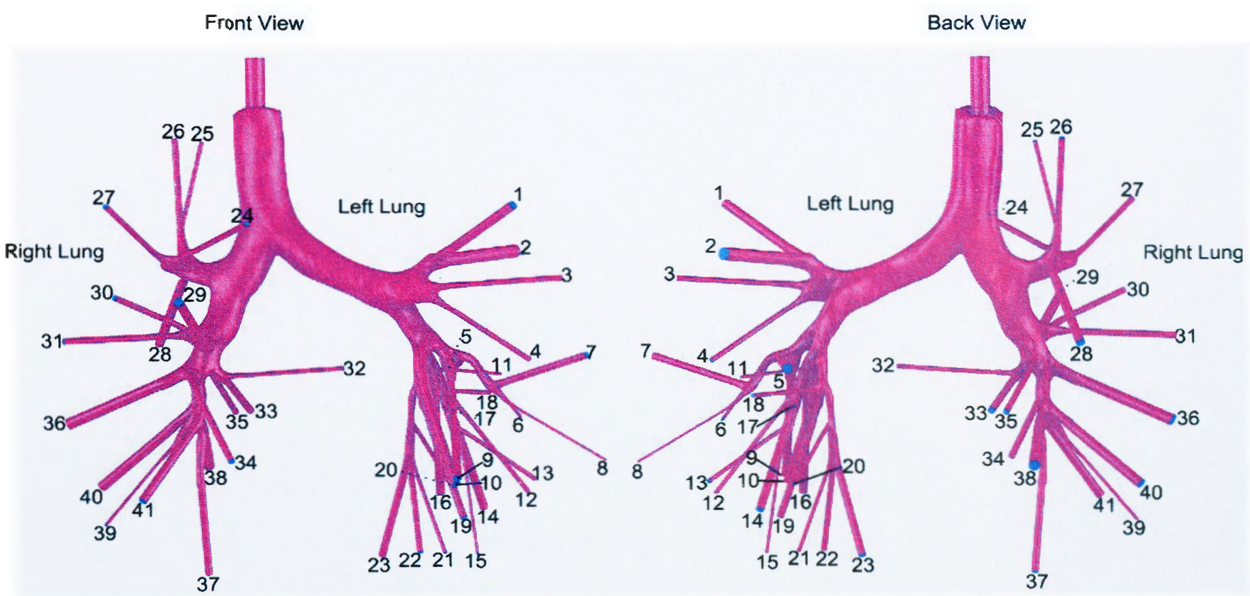

Figure 2.4: Completed geometry with extensions. Exported from Blender® 2.5.

2.1.3. Geometric Features Present in the Current Model. For CFD simulation purposes, important features of lung geometry are those that would cause changes in the fluid flow solution. Obvious examples may be main airway structures such as the nasal or oral passages, the trachea, or the generations of the lung. The way that these features are modeled is also important. Various simplifications to the airways have been used in the past [23, 26, 77-81]. One less obvious feature is the larynx, which a great deal of study has been devoted to. To summarize the general findings, the larynx creates a jet of air during inhalation that creates turbulence in the trachea and contributes to turbulent dispersion and deposition of aerosols in the trachea and upper bronchi [30, 82-85]. Other less obvious characteristics are the shape and orientation of the airways, which includes the direction the branching occurs, the branching angles, and any curvature of the airways. Cartilaginous rings have been given some attention as a potential influence on fluid flow and particle deposition [33, 68, 86-87]. Studies have also focused on carinal ridges and tumors [88-91].

In addition to the features of the lung geometry there are features of the ventilator circuit. The endotracheal tube (ETT) is certainly one of the most important ventilator circuit features to be included in the model. The endotracheal tube has had some study devoted to it in the past [68, 92-95]. The focus of these studies has typically been on measuring the effect of the ETT tube on airway resistance and workload, and hospital practices to prevent poor placement of the ETT during intubation. However the influence of the endotracheal tube has yet to be thoroughly explored from a fluid flow perspective, i.e., studies have not focused on what effects the ETT has on turbulence, flow distributions, or particle dispersion and deposition.

The model used in this study includes the trachea, the left and right main bronchi, and four to seven generations. There are a total of 41 outlets in the current geometry. The generation number at the outlets ranges from G4 to G7. Due to the nature of the reconstruction technique the lengths, sizes, branching angles, branch orientations, and shapes of the airways are consistent with the actual geometry of the patient. From the ventilator circuit, the endotracheal tube has been included and the fluid flow from the ventilator into the endotracheal tube has been modeled with an inlet condition. The larynx is not present in the current model. However, since the outlet of the endotracheal tube into the trachea is below the larynx, we hypothesize that the larynx should not have any significant effect on the fluid flow into the domain. Cartilaginous rings were not evident in the CT scans and were not included in the current airway model.

2.1.4. Advantages and Potential Problems. Due to the complex nature of the human airways and the need for accurate modeling, CT scan geometries offer several distinct advantages. However, there are also ways in which the data collection and geometry creation processes can contribute to errors in the study. The choice of geometry modeling technique also depends largely on the degree to which a single set of airways are representative of any set of airways. This has been looked at, but it is still yet to be fully determined [28].

Obvious advantages of using CT scan based geometries are the more accurate representation of a patient's airway size, shape, position, curvature, and diameter variations. CT scans will also capture patient specific characteristics like physical markers of disease, such as, tumors, or airway constrictions. Other patient specific characteristics such as lung injuries or surgical procedures or scarring may also be

visible. Currently the geometry creation process can be rather lengthy. However, with advancements in medical imaging technology and geometry creation software, the speed at which a computational geometry can be created may surpass the creation time for some idealized models that include some degree of patient specificity.

Although many aspects of a patient's actual lung geometry can be captured by the CT scans and are able to be reconstructed, others may be left out. There are some features of the lung that are known to exist and can be modeled but are not easily captured or reconstructed. One example of this is cartilaginous rings, which have been included in studies already mentioned but are not visible in CT scan geometries.

The reasons for the lack of some details in CT scan based geometries can be linked to several potential factors. The resolution of a scan can cause problems with the tissue fraction effect and characteristics smaller than a voxel size. Poor resolution can also lead to a tendency to over-smooth the surfaces. The smoothing operation can cause sharp features to be dulled or distorted. Cardiovascular and reparatory motion during the CT scan process can also lead to a blurring effect that will degrade the resolution in some parts of the CT scans.

The segmentation process is another source of potential geometric discrepancies. All of the CT scan quality issues mentioned above can make the segmentation process more difficult. The segmentation process is performed manually because there is no readily available software for automatic human airway segmentation, and if such software did exist, it would be unlikely that it could mimic the human intuition and knowledge of the human airways. Because segmentation is performed manually it could

contribute significantly to geometric discrepancies if it were performed by someone who is unfamiliar with the structure of the human airways.

2.1.5. Geometry Statistics. Geometric characteristics of the current airway model are given in Table 2.1. The outlet numbers provided in Table 2.1 correspond to the labels shown in Figure 2.4. The generation column designates how far down the tracheobronchial tree the outlets occur, with the trachea being G0 and the main bronchi as G1 and so forth. The size of the airways is given as hydraulic diameter described in Equation 1.1. The flow ratios are provided for each outlet as a percentage of the mass flow rate at the endotracheal tube. These flow ratios will be discussed further in § 3.3.3.

The geometric features present in the model down to the third generation have been compared to the two most common statistical models in Table 2.2. It is difficult to compare airway size directly with the statistical models because the size of human airways varies based on height, weight, physical activity, age, gender and several other physiological factors. For this reason the airway sizes of the current model and the statistical models were non-dimensionalized by defining a diameter ratio for each bifurcation. The diameter ratio presented in the table is defined as the daughter branch diameter divided by the parent branch diameter. The smaller diameter ratio for each bifurcation was designated as the minor diameter ratio and the larger was designated as the major diameter ratio. For the most part the diameter ratios are consistent with those presented in the Weibel and Horsfield models.

Table 2.1: Geometry information and flow ratios

Outlet #	Generation	Hydraulic Diameter (mm)	Flow Ratio, % of Trachea	Outlet # (cont.)	Genera-tion (cont.)	Hydraulic Diameter (mm) (cont.)	Flow Ratio, % of Trachea (cont.)
	Trachea	16.40	100.00%				
	ETT	8.36	100.00%	21	G7	1.5	0.32%
1	G4	4.01	4.96%	22	G6	2.47	1.12%
2	G4	5.88	10.66%	23	G7	3.17	1.44%
3	G4	2.43	1.82%	24	G4	2.44	3.06%
4	G4	2.19	1.48%	25	G4	1.79	1.65%
5	G5	4.01	3.77%	26	G4	2.6	3.47%
6	G5	1.22	0.35%	27	G4	2.34	2.81%
7	G6	3.06	1.71%	28	G4	3.93	7.93%
8	G6	0.93	0.16%	29	G4	3.88	5.01%
9	G4	3.37	3.41%	30	G4	2.59	2.23%
10	G4	3.78	4.29%	31	G4	2.84	2.69%
11	G6	1.31	0.31%	32	G5	1.88	0.92%
12	G7	1.79	0.46%	33	G5	2.99	2.33%
13	G7	1.82	0.47%	34	G5	2.83	2.09%
14	G7	3.43	1.68%	35	G5	2.52	1.66%
15	G7	1.16	0.19%	36	G5	4.92	6.32%
16	G5	3.46	2.81%	37	G7	3.05	1.48%
17	G5	0.87	0.18%	38	G6	4.69	4.49%
18	G5	1.94	0.88%	39	G7	1.21	0.23%
19	G5	3.04	2.17%	40	G6	4.34	3.84%
20	G7	1.67	0.40%	41	G6	3.67	2.75%

Table 2.2: Comparison of diameter ratios among statistical models

Parent Generation Number	Weibel Model		Horsfield Model		Current Model	
	Major Diameter Ratio	Minor Diameter Ratio	Major Diameter Ratio	Minor Diameter Ratio	Major Diameter Ratio	Minor Diameter Ratio
0	0.68	0.68	0.75	0.69	1.02	0.75
1	0.68	0.68	0.67	0.63	0.92	0.77
1	0.68	0.68	0.80	0.66	0.82	0.58
2	0.67	0.67	0.97	0.73	0.66	0.57
2	0.67	0.67	1.06	0.69	0.97	0.93
2	0.67	0.67	0.89	0.75	0.67	0.55
2	0.67	0.67	0.72	0.58	0.87	0.64

2.2. MESH

To solve the governing equations for fluid flow, the geometric domain was broken into very small elements and numerical methods were used to solve for the unknown quantities (this will be discussed in detail in Chapter 3). The elements, along with their faces and vertices, comprise the computational mesh. For CFD simulations in general, the mesh is important to ensure, geometric fidelity, useable data resolution, and numerical solution convergence. For CFD simulations using large eddy simulation (LES, see § 3.1) and particle tracking the mesh becomes a more involved aspect of the simulations and their results. The selection of the best mesh is not only important but also problem dependent.

2.2.1. State of the Art. Generation of a computational mesh requires the selection of element types (shapes), sizes, and orientations. Meshes can be organized into two major categories, structured and unstructured. Within each major category the meshes can be further divided by element type. Common element types include: hexahedrons (hexa), tetrahedrons (tetra), prismatic elements (prism), and pyramids (Figure 2.5). The two most commonly used element types are hexahedrons, and tetrahedrons.

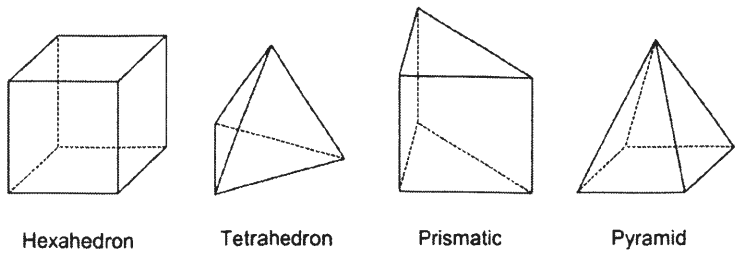

Figure 2.5: Element types

Due to the problem specific nature of mesh selection there have been studies of mesh type for cases related to the present case [96-97]. These studies do suggest a preference towards hexahedral elements that are aligned with direction of the flow. However they were performed with a RANS model on an idealized double-bifurcation. In addition Vinchurkar [97] suggests that structured hexahedral meshes are often prohibitively expensive in terms of time, despite the high quality solutions they typically produce. Even within the specific field of human airway fluid mechanics there is a variety of mesh styles being used for different problem formulations. Table 2.3 gives a summary of some studies and the mesh styles they have used. In general, the geometry and turbulence modeling formulation governs what type of mesh is fit to the geometry.

Meshes for CT scan based geometries are almost always unstructured and involve tetrahedrons. Unstructured hybrid meshes with tetrahedrons in the center and prism layers near the wall are frequently used with the low Reynolds number (LRN) formulation of the k-ω model. Prism layers are rarely used in conjunction with LES due to the cell anisotropy. For an idealized geometry hexahedrons are sometimes used but generally in cases where there are few generations.

Table 2.3: Literature review of turbulence modeling and mesh styles

Author (year)	Modeling and conditions	Geometry	Mesh type
Lambert A.R. et al (2011) [31]	LES, steady inlet velocity	CT-scan based, mouth up to G7	Tetrahedral
Xia, G. et al (2010) [18]	LES, Sinusoidal inlet waveform	CT-scan based, single bifurcation G3 to G4	Tetrahedral
Choi,J. et al (2010) [71]	LES, Sinusoidal inlet waveform	CT-scan based, mouth up to G7	Tetrahedral
Lin, Ching-Long, et al (2007) [83]	DNS, steady inlet velocity	CT-scan based, Two models start from trachea up to G6: Model 1- includes mouth and larynx Model 2- without mouth and larynx	Tetrahedral
Xi, J. et al (2008) [99]	LRN k-ω, steady inlet velocity	Mouth to trachea, CT-scan based and idealized	Realistic model: hybrid: tetrahedral with prism layers Ideal model: structured hexahedral
Xi, J. et al (2008) [30]	LRN k-ω, steady inlet velocity	CT-scan based larynx up to G5	Hybrid: tetrahedral with prism layers
Isaacs, K.K. et al (2006) [100]	laminar, steady inlet velocity	Idealized model, single bifurcation	Structured hexahedral
Zhang, Z. et al (2008) [101]	LRN k-ω, steady inlet velocity	Idealized geometry, series of triple bifurcations to simulate G0-G15	Structured hexahedral
Farkas, A. et al (2007) [102]	Laminar steady inlet velocity	Idealized geometry. Trachea up to G2	tetrahedral

2.2.2. Mesh Creation. The mesh selection problem was carefully considered for this study. Structured hexahedral meshes have proven to be a good choice for geometries with simple features such as circular airways, symmetrical branching patterns, or a low number of bifurcations. The geometry of the current study is based off of CT scans and

is complex for meshing purposes. A structured hexahedral mesh was attempted in ANSYS® ICEM® CFD but found to be prohibitively time consuming and it was not clear that a grid absent of rapid changes in cell size would be achievable.

An unstructured hexahedral mesh created by a body fitted Cartesian method was also considered but a mesh with isotropic and high quality elements was not able to be realized. The modeling guide for the chosen solver, CFX®-13.0, suggests the use of isotropic grids with tetrahedral rather than hexahedral elements [98]. ANSYS® ICEM® CFD also offered options for hybrid meshes such as a tetrahedral mesh with prism layers in the near wall region or a tetrahedral mesh with a hexahedron core. However the cells of a prism layer would be anisotropic and a hexahedron core would require a sudden change in element type and size. For these reasons a fully tetrahedral mesh was adopted for the current study.

The computational mesh was created using ANSYS® ICEM® CFD. The geometry was imported as an STL file after geometry cleanup and the addition of extensions in Blender® 2.5. A build topology operation was performed to establish the curves and points from the edges of the surfaces and to ensure there were no holes or gaps in the geometry. The surfaces of the geometry were separated into several different parts so that mesh parameters could be specifically set for each part. Curves and points that were not meant to guide the mesh were deleted to avoid unnecessary constraints for the mesh. Parameters including maximum element size and tetra size ratio were set for each part. The smoothing option was turned off so that the surface mesh could be later smoothed without the volume elements to constrain it.

An octree method was used to compute a mesh in the domain [103]. Octree meshing is performed by continually dividing a tetrahedron that encloses the entire domain. When an element is below the maximum element size it will stop splitting. Then if an element is intersected by a surface then the mesher will look at the distance between the nodes of the element and the surfaces. If the node is within a tolerance then the node is projected to the surface. If the node is not within the tolerance then the element is refined. In this way the mesher will create a mostly uniform mesh that is fit to the surface of the geometry. For the current study the mesh generated in the volume was not the focus of this operation. The octree method created a reasonable surface mesh but the volume could better be created with an operation that grows mesh inward from the surface mesh.

The volume elements were then deleted while the surface elements were retained for smoothing. To obtain a high quality surface mesh the surface elements were smoothed first using a Laplace smoothing operation. The goal of this operation is to find a good center point for each node with respect to the nodes it is connected to by edges. This smoothing process is iterative and will result in a more uniform spacing of nodes. After the Laplace smoothing operation a smoothing operation was performed without the Laplace smoother. This operation focused on moving nodes to improve the quality of the surface elements. This smoothing operation is also iterative and resulted in a high quality surface mesh. It is important to note that during the smoothing operations the nodes were constrained to the surface specified in the input STL file.

The surface elements were then examined for quality. The quality of a surface element (triangle) is defined as the minimum ratio of the height of the triangle to its

corresponding base length, normalized so that an equilateral triangle would have a quality of 1. Any element that was of quality less than 0.45 was manually corrected by splitting a mesh edge or merging two mesh nodes and re-smoothing. The minimum quality of any surface element was 0.455 and the average quality of surface elements was 0.866. A total of 2.39×10^5 surface elements were created.

To create a high quality volume mesh with a smooth transition in element size, an advancing front Delaunay method was used [103]. This operation takes the surface mesh as an input and will place points in the interior and create a Delaunay triangulation to determine edges and faces of the created tetrahedral elements. A growth ratio of 1.25 was used to control the expansion of the volume elements as the distance from the wall increased. After creation of the volume elements a smoothing operation was performed to improve the quality of the volume elements. Several iterations were first performed without modifying the surface mesh. Several more iterations were performed while allowing the surface to adjust along with the volume. The surface nodes were once again constrained to the surfaces of the geometry.

The volume elements were then examined for quality. Any element that was of low quality was manually corrected by splitting a mesh edge or merging two mesh nodes and re-smoothing. The quality of a tetrahedral volume element is defined as the ratio of the radius of an inscribed sphere to the radius of a circumscribed sphere, normalized so that a regular tetrahedron would have a quality of 1. The minimum quality of any volume element was 0.400 and the average quality of the volume elements was 0.746. A total of 1.11×10^6 tetrahedral volume elements were created and there were a total of 2.50×10^5 nodes in the computational mesh. The created mesh is shown in Figure 2.6.

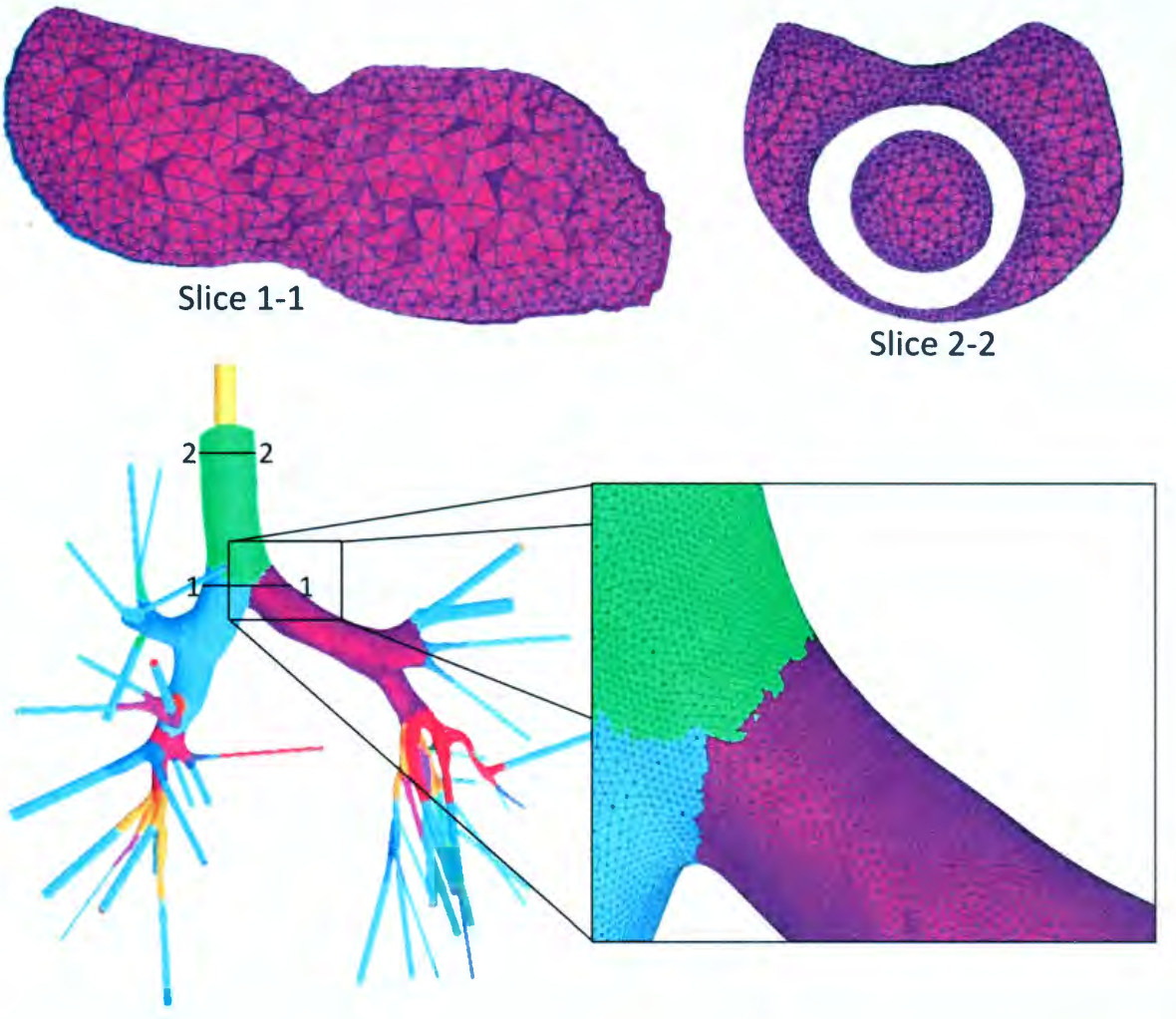

Figure 2.6: Computational mesh. The expanded view displays the surface mesh. Slice 1-1 shows the volume mesh in a cut plane through the transition between parent and daughter branches in the first bifurcation. Slice 2-2 show the volume mesh in a cut plane through the trachea and the endotracheal tube.

3. MODELING

This study models fluid flow and particle transport and deposition in a realistic airway geometry. Computational fluid dynamics (CFD) was employed to solve governing equations for the flow field variables. CFD is a set of numerical methods used to model and solve equations that govern fluid motion; most notably the conservation equations for mass, momentum, and energy [104]. A computational domain with a set of boundary conditions is divided into many elements in time and space over which, the modeled equations are applied and solved algebraically to obtain numerical values for field variables at discrete points [104].

Fluid and particle properties, turbulence modeling, boundary conditions, and particle transport modeling were carefully chosen and specified in the commercial CFD software ANSYS® CFX®. Several of the numerical specifications were set using user FORTRAN subroutines or CFX® expression language (CEL). Simulations were run in parallel on a machine with 8 Intel® Xeon® E5620 processors (2.4 GHz), 24 GB RAM, and Windows® 7 Enterprise edition. This chapter will offer detailed descriptions of the numerical modeling of, momentum, particle transport, and boundary conditions used for the simulations. The references cited should be consulted for further detail on the numerical models presented here.

3.1. MOMENTUM

The working fluid for the simulations run for this study is dry air at 25 °C with a constant density of $\rho = 1.185$ kg/m^3 and a dynamic viscosity of $\mu = 1.831 \times 10^{-5}$ kg/m·s at an ambient pressure 1 atm. A transient simulation was run for one breathing cycle. Heat transfer and gravity were not considered in this study.

At peak inspiratory velocity the Reynolds number throughout the domain ranges from about 180 to 13,400 indicating that both laminar and turbulent conditions should be seen in the flow as discussed in § 1.1. To model turbulence, large eddy simulation (LES) was used. The wall-adapted local eddy-viscosity (WALE) model was chosen for the subgrid-scale eddy viscosity model [105]. The ability of LES to resolve large scale turbulence eddies gives it a distinct advantage over Reynolds averaged Navier-Stokes (RANS) models for accurately modeling particle transport [106]. The WALE model was chosen for subgrid-scale eddy viscosity modeling for its ability to reproduce the laminar to turbulent transition process [105].

The principle behind LES is a filtering of the large scale turbulence. The larger scale flows are directly resolved while the smaller scales are modeled, usually with an eddy viscosity model [107]. Particle motion is influenced more by the larger scales of fluid motion and the effect of the smaller scale (subgrid scales) turbulent motion is reduced further in the case of particles with higher inertia [108]. Direct numerical simulation (DNS) would resolve all of the flow scales, but is computationally expensive and may not add much due to the dominance of the large scales for particle transport.

The filtered conservation of mass equation for incompressible flow is:

$$\frac{\partial \overline{u}_i}{\partial x_i} = 0 \tag{3.1}$$

where u_i is the i^{th} velocity component with an overbar denoting filtering.

The filtered momentum equation for incompressible flow is [109]:

$$\frac{\partial \overline{u}_i}{\partial t}+\frac{\partial}{\partial x_j}(\overline{u}_i\overline{u}_j)=-\frac{1}{\rho}\frac{\partial \overline{p}}{\partial x_i}+\frac{\partial}{\partial x_j}\left[\nu\left(\frac{\partial \overline{u}_i}{\partial x_j}+\frac{\partial \overline{u}_j}{\partial x_i}\right)\right]-\frac{\partial \tau_{ij}}{\partial x_j} \tag{3.2}$$

where x_i is the i^{th} position component, ρ is the fluid density, p is the pressure, ν is the fluid kinematic viscosity, and τ_{ij} is the subgrid-scale stress defined by [109]:

$$\tau_{ij}=\overline{u_iu_j}-\overline{u}_i\overline{u}_j \tag{3.3}$$

The relationship between the subgrid-scale stress and the large-scale strain rate tensor $\overline{S}_{ij}$ is expressed in Equation 3.4 [109].

$$-(\tau_{ij}-\tfrac{\delta_{ij}}{3}\tau_{kk})=2\nu_{sgs}\overline{S}_{ij} \tag{3.4}$$

The strain rate tensor, $\overline{S}_{ij}$ is defined by [109]:

$$\overline{S}_{ij}=\frac{1}{2}\left(\frac{\partial \overline{u}_i}{\partial x_j}+\frac{\partial \overline{u}_j}{\partial x_i}\right) \tag{3.5}$$

The subgrid scale viscosity ν_{sgs} for the LES WALE model is modeled by [109]:

$$\nu_{sgs}=(C_w\Delta)^2\frac{(S_{ij}^dS_{ij}^d)^{\frac{3}{2}}}{(\overline{S}_{ij}\overline{S}_{ij})^{\frac{5}{2}}+(S_{ij}^dS_{ij}^d)^{\frac{5}{4}}} \tag{3.6}$$

In Equation 3.6 S_{ij}^d is the traceless symmetric part of the square of the velocity gradient tensor i.e. [109]:

$$S_{ij}^{d} = \frac{1}{2}(\bar{g}_{ij}^{2} + \bar{g}_{ji}^{2}) - \frac{1}{3}\delta_{ij}\bar{g}_{kk}^{2} \tag{3.7}$$

where $\bar{g}_{ij}$ is the velocity gradient tensor i.e. [109]:

$$\bar{g}_{ij} = \frac{\partial \bar{u}_i}{\partial x_j} \tag{3.8}$$

A second order central differencing scheme was used for advection and a second order backwards Euler scheme was used for transience. A residual target of 10^{-4} was set for convergence at each time step. ANSYS® CFX ® is an implicit solver.

3.2. PARTICLE TRACKING

To model particle tracking in the domain, a Lagrangian particle tracking method was used. The particles were assumed to have a low enough volume fraction as to not have a significant effect on the carrier fluid. The particles used in this study were assumed to be spherical particles with constant diameters with a constant density of 2000 kg/m^3. Particles were injected at the inlet of the domain at random positions given by a uniform distribution. The diameters of the particles injected were selected from a uniform distribution between 0.05 and 10 μm. The velocity of the particles at the site of injection was set to match the velocity of the fluid. At the highest volumetric flow rate seen during inspiration, the Stokes numbers of the particles ranged from 2.90×10^{-5} to 2.95 throughout the domain. A FORTRAN user subroutine was used so that the rate of particles injected scaled with the inlet mass flow rate such that the total number of particles would be close to 100,000.

The injected particles were then tracked through the domain until the particle deposited on the wall, escaped from the domain, or encountered some form of integration error. Particles were considered to have deposited on the wall when the distance between the particle center and the wall was less than the particle radius. Upon deposition a user FORTRAN subroutine was called to output variables including the particle diameter, position, and time of deposition. These values were used for post processing the particle deposition results. A particle was considered to have left the domain when the particle crossed an outlet boundary. An integration error would occur when the particle exceeded the maximum number of integration steps i.e. 1,000,000, when the particle exceeded the maximum tracking distance i.e. 100 m, or when a particle's velocity became very close to zero. Particle end statuses will be discussed further in § 4.6.1.

As the particles were tracked through the domain, the particle displacement was calculated using forward Euler as [109]:

$$x_p^{n+1} = x_p^n + v^n \Delta t \tag{3.9}$$

where, x_p is the particle position, v is the particle velocity and Δt is the particle tracking time step size. The subscript n in Equation 3.9 indicates the particle tracking step number. The particle velocity v comes from the particle momentum equation [109]:

$$m_p \frac{dv}{dt} = F_{all} = F_D + F_L + F_B \tag{3.10}$$

where m_p is the mass of the particle, and F_{all} is the sum of all the forces acting on the particle. The particle momentum equation (Equation 3.10) is a form of the generic transport equation with an analytic solution. The particle velocity v is solved for by using the analytic solution. The forces that make up F_{all} include the drag force F_D, the Saffman lift force F_L, and the Brownian motion force F_B, as used by Xi *et al* [30]. These forces were implemented in ANSYS® CFX® with a user FORTRAN subroutine. The calculations of these forces are briefly described below. Refer to the cited works for further detail or derivation of these expressions. The effects of gravity were not accounted for in this study because the direction of gravity during drug delivery for this patient was not well known. Particles were tracked over several iterations during each fluid flow time step. The particle time step was determined by dividing the local element length scale by the particles velocity and the number of time steps per element, which was set at 10.

3.2.1. Drag Force. The drag force is the resistive force of the fluid on the particle due to their relative velocities. The i^{th} component of the drag force term F_D is modeled in this study by:

$$F_{D,i} = \frac{\rho_f \pi C_D d_p^2 |u - v|}{8C_c}(u_i - v_i) \tag{3.11}$$

where ρ_f is the fluid density, d_p is the particle diameter, and u is the fluid velocity. The expression of Morsi and Alexander was used for drag coefficient of the particle, C_D [110]. In Equation 3.11, the Cunningham correction factor, C_c, is described by [111]:

$$C_c = 1 + \frac{\lambda}{d_p}\left(2.34 + 1.05e^{-0.39\frac{d_p}{\lambda}}\right) \tag{3.12}$$

where λ is the mean free path, taken to be 65 nm. The Cunningham correction factor is on the order of 1.15 for a 1 μm diameter particle and this will increase rapidly as the particle size decreases, but is negligible for particle larger than a 10 μm in diameter [111]. In this study the Cunningham correction factor is expected to be significant for the particle diameter range of 0.05-10 μm.

3.2.2. Lift Force. The lift force is caused by a pressure differential that occurs under the conditions of a particle moving at a different speed than the fluid at a location where a large velocity gradient is present such near a wall [58]. A particle that is moving faster than the fluid will be forced towards the wall, while a particle moving slower than the fluid will be forced away from the wall [58]. The drag force will act to diminish the difference in particle and fluid speeds, but for particles with significant inertia in areas with rapidly changing geometry or significant turbulence, this force is expected to play a large role in the particle's motion. The i^{th} component of the lift force F_L is described by [112]:

$$F_{L,i} = \frac{-\rho_f d_p^2 \hat{n}_i}{4m_p}\left[u_s^2 \cdot g(\kappa, \Lambda)\right] \tag{3.13}$$

where $\hat{n}$ is the unit wall normal vector pointing out of the domain. The wall-tangent slip velocity u_s in Equation 3.13 is described by [112]:

$$u_s = v \cdot \hat{t} - u \cdot \hat{n} \tag{3.14}$$

where $\hat{t}$ is the unit wall-tangent vector in the direction of the particle velocity, i.e.:

$$\hat{t} = \frac{(\hat{n} \times v) \times \hat{n}}{|(\hat{n} \times v) \times \hat{n}|} \tag{3.15}$$

The function g used in Equation 3.13 is an empirical expression developed by Cherukat and McLaughlin for a freely rotating sphere close to a wall and is described by [113]:

$$\begin{aligned} g(\kappa, \Lambda) = & \left[1.7631 + 0.3561\kappa - 1.1837\kappa^2 + 0.845163\kappa^3\right] \\ & - \left[\frac{3.24139}{\kappa} + 2.6760 - 0.8248\kappa - 0.4616\kappa^2\right]\Lambda \\ & + \left[1.8081 + 0.8796\kappa - 1.9009\kappa^2 + 0.98149\kappa^3\right]\Lambda^2 \end{aligned} \tag{3.16}$$

The parameters κ and Λ are defined as [113]:

$$\kappa = \frac{2h_p}{d_p} \tag{3.17}$$

where h_p is the distance from the wall to the particle, and

$$\Lambda = \frac{\dot{\gamma} d_p}{2u_s} \tag{3.18}$$

where the shear rate $\dot{\gamma}$ is approximated for particles near the wall by [113]:

$$\dot{\gamma} \approx \frac{u \cdot \hat{t}}{r_{i_p}} \tag{3.19}$$

3.2.3. Brownian Motion Force. The Brownian motion force is caused by random bombardment of the aerosol particle by the surrounding gas particles [111]. At a microscopic level the effect of the force is random in direction, however at a macroscopic level the particles begin to move from areas of higher concentration to lower concentration and this effect is often referred to as particle diffusion [111]. The effects of Brownian forces are most noticeable on particles that have very low inertia i.e. particles with a diameter less than 1 μm [114]. The i^{th} component of the Brownian motion force, F_B is [114]:

$$F_{B,i} = \frac{\zeta_i}{m_p}\sqrt{\frac{1}{\tilde{D}}\frac{2k_B^2T^2}{\Delta t}} \tag{3.20}$$

where k_B is the Boltzman constant, T is the absolute temperature of the fluid, Δt is the particle integration time step, and ζ is a vector of 3 randomly generated numbers each taken from a Gaussian distribution with zero mean and unit variance. The Brownian diffusivity $\tilde{D}$ in Equation 3.20 is defined as:

$$\tilde{D} = \frac{k_b T C_c}{3\pi\mu a_p} \tag{3.21}$$

where μ is the dynamic viscosity of the fluid.

3.3. BOUNDARY AND INITIAL CONDITIONS

Boundary conditions were carefully selected and implemented for the inlet, the walls of the CT scanned reconstructed geometry, the walls of the artificial extensions

added to the outlets, and the outlets of the computational domain. This section discusses the numerical specifications at the inlet, walls, and outlets of the domain and the initial conditions.

3.3.1. Inlet. The inlet refers to the circular boundary at the top of the endotracheal tube which is technically only an inlet during inspiration. The velocity at the inlet was specified with Cartesian velocity components. In the domain creation process an extension was added to the inlet reconstructed from the CT scans so that there was a smooth transition to a circular cross section. In addition the domain was oriented so that the plane of the inlet coincided with the x-y plane and the center of the circular inlet was coincident with the origin. These adjustments facilitated the implementation of a Cartesian velocity component specification at the inlet. The velocity profile at the inlet was specified as a fully developed turbulent velocity profile described by [30]:

$$u(r,t) = 1.224 u_m(t)\left(\frac{R-r}{R}\right)^{\frac{1}{7}} \tag{3.22}$$

where r is the radial distance from the origin, R is the radius of the inlet, and u_m is the time varying mean velocity at the inlet, which is dependent upon the inspiratory waveform. The selection of this profile is appropriate considering the turbulent Reynolds numbers present in the tube over most of the breathing cycle. Curvature effects in the tube upstream of the inlet were not considered for this study.

3.3.2. Walls. The walls of the domain were assumed to be smooth and rigid. A no slip boundary condition was applied to the walls of the domain i.e. the velocity was zero at the walls. The effects of the mucus layer lining the walls were not accounted for

in this study. The surface at the top of the trachea connecting the endotracheal tube and the walls of the trachea is due to the end of the CT scan field of view. This area is not physiologically realistic but was modeled just as the other walls in the domain. In reality the flow across this area is expected to be small because of the balloon attached to the endotracheal tube designed to seal the endotracheal tube against the walls of the larynx. The walls that were reconstructed from CT scans were set with parallel and perpendicular restitution coefficients of zero so that particles would deposit on contact. The walls of the artificial extensions at the outlets were given a parallel restitution coefficient of 1.0 and a perpendicular restitution coefficient of 0.1 so that no particles would collect on those walls.

3.3.3. Outlets. The flow at the outlets was specified with a mass flow rate. The mass flow rates were given as fractions of the instantaneous mass flow rate at the inlet of the domain. Similar mass flow rate specifications have been used past studies [30, 70, 115-116]. The mass flow rate fraction at each of the outlets was calculated based on data from Horsfield *et al* [8]. The mass flow rate fraction F_m at the i^{th} outlet is:

$$F_{m,i} = F_{H,j} \frac{A_{G7,i}}{A_{G7s,j}} \tag{3.23}$$

where $F_{H,j}$ is the mass flow rate fraction for the j^{th} branch given by Horsfield *et al*, $A_{G7,i}$ is the G7 equivalent area of the i^{th} outlet i.e.:

$$A_{G7,i} = \left(\frac{2}{R_{pd}^2} \right)^{7-G_i} A_i \tag{3.24}$$

where R_{pd} is the parent daughter diameter ratio, taken here as 1.25 (the average of the parent daughter diameter ratios for generations G4-G7 in Weibel's model A) [17]. In Equation 3.23, $A_{G7s,j}$ is defined as the sum of the G7 equivalent areas of the outlets that are supplied by the branch corresponding to the j^{th} branch given by Horsfield *et al* [8]. The mass flow rates at the outlets are specified, however, the distribution of the mass flow over the outlet is a function of the mass flow just upstream of the outlet [98].

3.3.4. Initial Conditions. Time t=0 is set to be the onset of inspiration and it is assumed that an identical breathing cycle has just finished. For all waveforms except the pressure controlled sinusoidal waveform, (which will be discussed in § 4.1) the flow in expiration is quick at the beginning of expiration and then flattens out asymptotically approaching zero. The inlet flow rate in expiration is less than 2 % of the maximum inlet flow rate in expiration for $t > \sim 3.2$ s. Therefore at time t=0 the velocity was set as zero.

4. RESULTS AND DISCUSSION

To simulate realistic ventilator condition the respiratory waveforms were modeled. Mean flow speed at the inlet was set to reproduce respiratory waveforms used by commercial ventilators. To establish confidence in the computational model grid convergence and time step convergence studies were performed. A validation study was also performed to check the computational model against experiments [117]. When these studies were completed simulations were ran using the various waveforms discussed in § 4.1. In this section, we discuss respiratory waveform creation, grid convergence, time step convergence, and validation studies, as well as fluid flow and particle tracking results obtained using numerical simulations.

4.1. WAVEFORMS

In this study seven different waveforms were created and modeled in the inlet condition. The waveforms represent a number of ventilator conditions commonly seen in manufactured mechanical ventilators [47]. This section will describe the creation of the respiratory waveforms and the application of those waveforms to the computational model.

The waveforms created for this study were governed by the equations of motion for the lungs given in Equation 1.3 and Equation 1.4 in § 1.3.2. One of the three control variables (pressure, volume, or flow rate) was constrained and the other two were solved for numerically. Waveforms were constrained to have the same tidal volume and period. A small rise/fall time was incorporated to smooth the waveforms and to avoid non-physical flow phenomena such as an instantaneous (step) change in flow velocity. The tidal volume of the lung was approximated as 650 mL and the lung properties of

compliance and resistance (Equation 1.5 and Equation 1.6 respectively) were taken as 0.127 L/cm H_2O and 4.33cm H_2O/(L/s) respectively. The values for resistance and compliance were found by averaging the resistances and compliances reported by Grimby for patients with COPD [118]. The ventilator waveforms used in this study are shown in Figure 4.1.

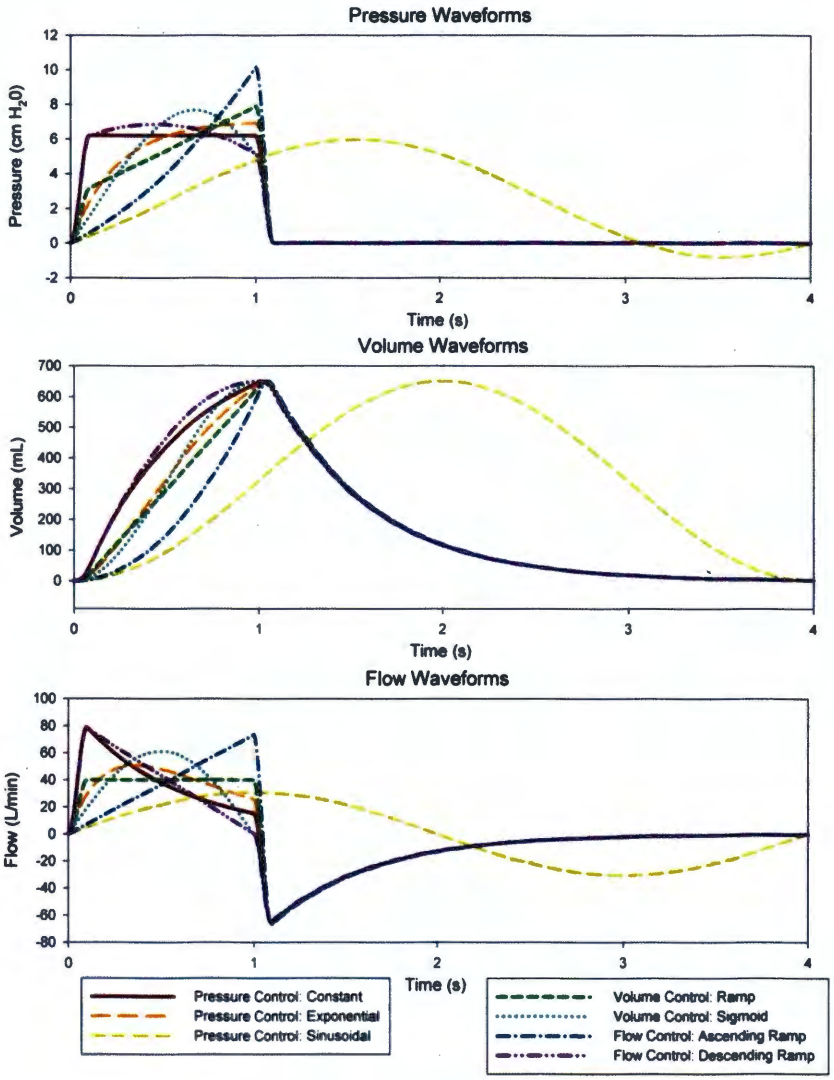

Figure 4.1: Ventilator waveforms

Seven waveforms, commonly used by commercial ventilators, are shown in Figure 4.1. The waveforms represent three different methods of controlling how a patient respires. Three of the waveforms would be seen for a ventilator that is controlling breaths by the ventilator output pressure (pressure control). Two of the waveforms would be seen for a ventilator that is controlling breaths by monitoring the volume of air that has passed into the lung (volume control). The remaining two waveforms would be seen for a ventilator controlling the flow rate into the lungs (flow control). The sinusoidal pressure waveform would be seen with the use of a reciprocating pump and this is the reason why the shape of the curve is slightly different from the rest. For all waveforms except for the sinusoidal pressure waveform the inspiration time was set to approximately 1 second. The expiration is in the shape of an exponential decay, modeling a natural outward breath based on the elasticity of the lung.

MATLAB® scripts were created to generate the waveforms. Simple shapes, including ramps, sinusoids, and an exponential rise, were imposed on the control variables during inspiration as seen used by commercial ventilators [47]. In all waveforms except the pressure controlled sinusoidal waveform, the expiration was obtained by setting the pressure to zero. For the pressure controlled ventilation mode the pressure was set throughout the breathing cycle, the volume waveform was solved for by applying a 4^{th} order Runga-Kutta method to the equation of motion for lungs (Equation 1.3), and the flow waveform was solved for by plugging in the values for pressure and the solved values for volume into the equation of motion for lungs. The volume is assumed to be zero as an initial condition. For the volume controlled ventilation mode the volume was initially set for inspiration, the flow waveform was solved for by numerically

integrating the volume waveform by trapezoid rule, a small rise/fall time was incorporated to smooth the flow waveforms and to avoid non-physical flow phenomena such as an instantaneous (step) change in flow velocity, the volume waveform was re-solved for from this new flow waveform using finite difference, and the pressure was solved for by plugging in the values for volume and flow into the equation of motion for lungs. For the flow controlled ventilation mode the flow was set for inspiration, the volume waveform was solved for by applying finite difference to flow waveform, and the pressure was solved for by plugging in the values for volume and flow into the equation of motion for lungs. The volume and flow waveforms in expiration for volume and flow ventilation modes were solved for by the method applied for the pressure controlled mode. The tidal volume was set for the final waveforms by iteratively scaling the input waveforms for the control variables and measuring the resulting tidal volume. The averaged velocity across the inlet was calculated from the flow rate waveform using the area of the inlet and was output to a file for use in ANSYS® CFX®. The MATLAB® scripts are provided in APPENDIX C.

4.2. GRID CONVERGENCE

A study was performed to ensure that the solution obtained would be grid independent. The grid convergence study was carried out on a simplified geometry described by Zhao and Lieber [119] which also allowed us to compare our preliminary simulations with experimental data obtained from their work. In this study the parent tube diameter, D, is taken to be the same as the hydraulic diameter of the trachea of the CT scan model geometry, i.e. 16.4 mm. The geometrical feature relationships of the model bifurcation to the parent diameter are taken to be the same as in Zhao's geometry

which is illustrated in Figure 4.2. Likewise the branching angle, 2α, is 70°, and the angle β, is 18°. The station numbers and locations are as shown by Zhao *et al* [119].

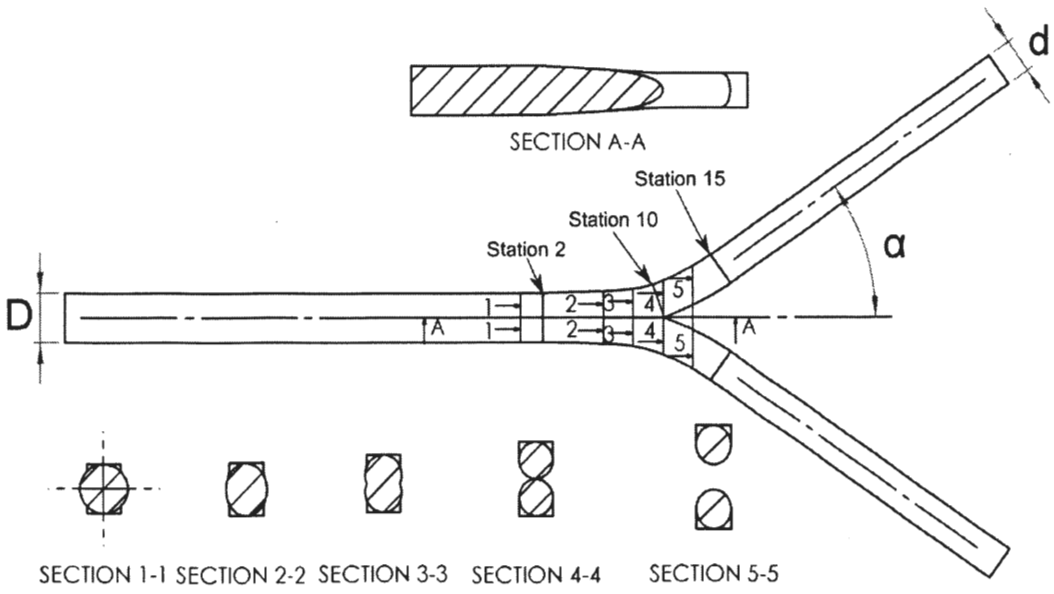

Figure 4.2: Geometry for convergence and validation simulations. Modeled as the geometry described in ref. [119]. The bifurcation plane contains the centerlines of the parent and daughter airways. The local transverse plane is perpendicular to the bifurcation plane and contains a line tangent to the centerline of the airway.

The geometry in Figure 4.2 was created using a MATLAB® program to generate a set of points to describe the curves defined by Zhao *et al* [119]. These points were then imported into SolidWorks and cubic splines were generated to represent the geometry. The SolidWorks "loft" feature was used to create a solid geometry using the cubic splines as constraints for the loft operation. This geometry was exported to ANSYS® ICEM® CFD as a standard ACIS text (SAT) file for meshing.

A number of grids were generated in ANSYS® ICEM® following the procedure explained previously in the mesh creation section (§ 2.2.2). All grids were purely tetrahedral with varying numbers of elements. The minimum element quality for each grid was greater than 0.4. The average element quality for each grid was greater than 0.75. The number of nodes and elements for each grid are shown in Table 4.1.

Transient simulations were run on these grids using the methods described in section 3. The simulations were run until peak inspiration was reached for the constant pressure ventilator waveform shown in Figure 4.1. The Reynolds number in the parent tube of the model bifurcation was 6578 and matched the Reynolds number of the trachea of the CT scan geometry at peak inspiration. A constant time step of 5×10^{-6} s was used for each simulation, to ensure a low Courant number.

Table 4.1: Grid convergence information

Tetrahedra	Triangles	Nodes	Percent Difference
1.69E+06	2.44E+05	3.45E+05	N/A
7.85E+05	1.24E+05	1.63E+05	0.74%
4.45E+05	7.47E+04	9.35E+04	0.80%
2.26E+05	4.18E+04	4.86E+04	1.76%
1.17E+05	2.43E+04	2.60E+04	3.29%
6.71E+04	1.56E+04	1.54E+04	3.99%
3.59E+04	9.54E+03	8.61E+03	7.07%

Values of the velocity magnitude at station 2 of the model bifurcation geometry in the bifurcation plane were taken for each grid at peak inspiration. The velocity magnitude for selected grids is shown in Figure 4.3 for convergence visualization

purposes. The numbers in the legend indicate the number of tetrahedral elements in the mesh. Visually the curves begin to collapse onto the curve of the finest grid. There is little difference visually between the velocity profile plots for the grid with 4.45×10^5 elements and the finest grid (1.69×10^6 elements).

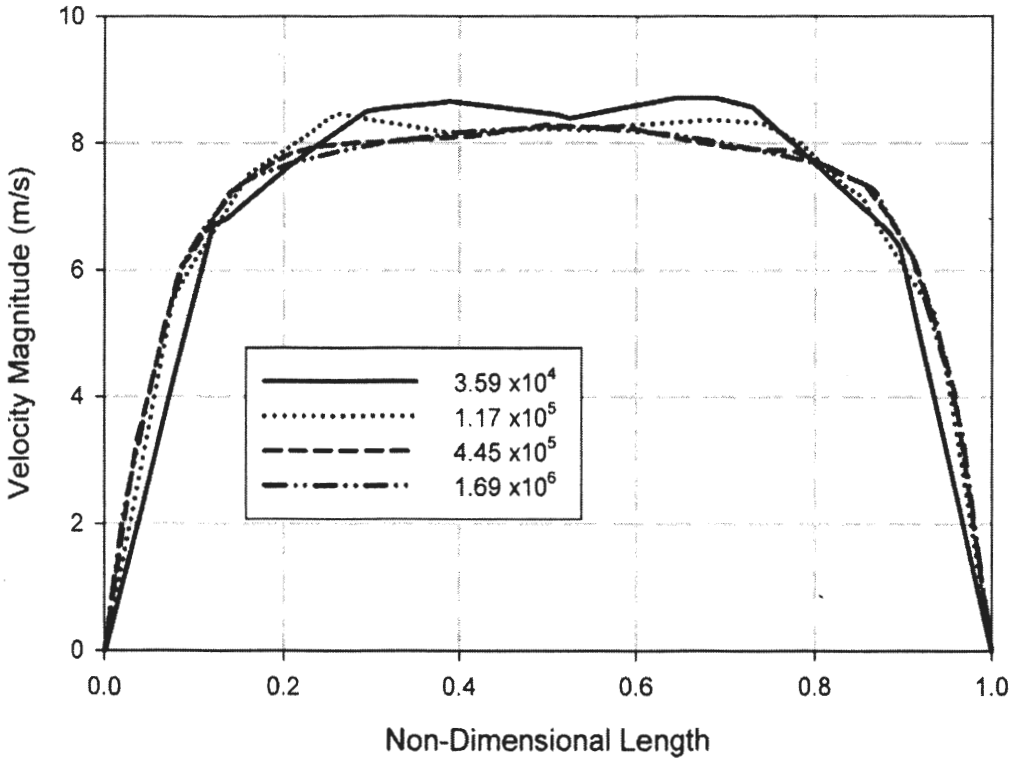

Figure 4.3: Velocity profiles at station 2, for convergence visualization. Velocity profiles are along the diameter of the parent tube. Non-dimensional length is 0 at one side of the airway, 0.5 at the center, and 1 at the other side of the airway.

The percent difference between the profiles was calculated and is shown in Table 4.1. The mesh density of the grid with 4.45×10^5 tetrahedral elements shows low percent

difference i.e. less than 1% and this density was used for the mesh of the CT scan geometry. The mesh was made finer at some of the smaller features of the for the CT scan model to retain the geometric detail of the patient specific scans.

4.3. TIME STEP CONVERGENCE

A detailed study was also performed to ensure the solution would be time step independent. A computational domain with 4.45×10^5 elements as described in the grid convergence study was used. The Reynolds number in the parent tube of the model bifurcation, again, matched the Reynolds number of the trachea of the CT scan geometry at peak inspiration i.e. 6578. The simulations ran until just after peak inspiration for the constant pressure ventilator waveform shown in Figure 4.1.

An adaptive time stepping method was used based on the RMS Courant number of the flow. By adjusting the limiting RMS Courant number, the relative time step size was also adjusted proportionally. Values of velocity magnitude were taken from the center point of station 2 at each time step. Time values of the velocity magnitudes for selected Courant number limits are shown in Figure 4.4 (a) for convergence visualization purposes. The numbers in the legend indicate the limiting courant number used for adaptive time stepping. Visually there is very little difference between the curves.

The percent difference between the velocity magnitude time plots was calculated and is shown in Table 4.2. For each time step size there was a very low percent difference i.e. less than 1%. Values of resolved turbulence kinetic energy (TKE) were also taken at each time step from the center point of station 2. Time values for TKE at selected Courant number limits are shown in Figure 4.4 (b) for convergence visualization purposes. Again there is very little difference between the curves visually. A more

quantifiable difference can be seen when the percent differences are calculated. The percent differences for TKE at different courant number limits are shown in Table 4.2. A limiting RMS Courant number of 1 was chosen to be used in the simulations with the CT scan geometry.

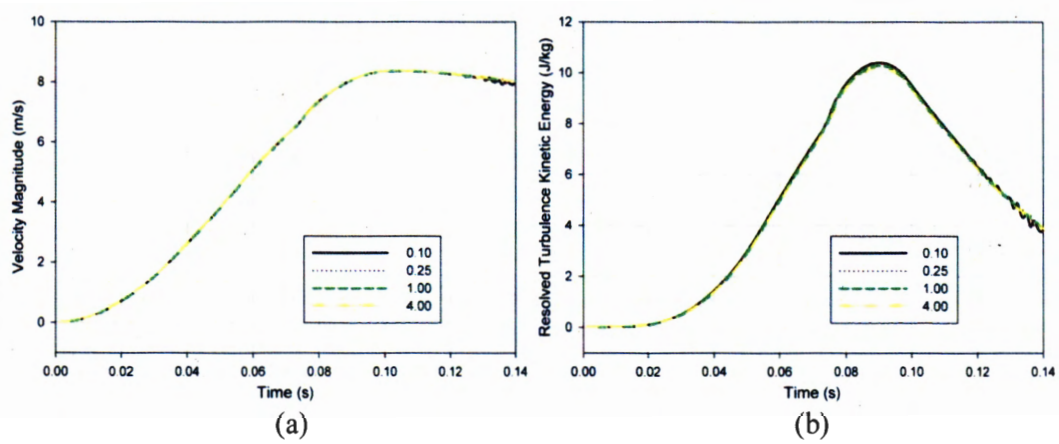

Figure 4.4: Time step convergence visualization. (a) Velocity and (b) resolved turbulence kinetic energy at the center of station 2.

Table 4.2: Time step convergence information

Courant Number Limit	Velocity Magnitude Percent Difference	TKE Percent Difference
0.10	N/A	N/A
0.25	0.07%	0.44%
0.50	0.09%	0.77%
1.00	0.10%	1.18%
2.00	0.11%	1.62%
4.00	0.11%	1.91%

4.4. VALIDATION

For validation purposes, a simulation was run to be compared with experimental data on a simplified geometry. Fluid properties and boundary conditions were set up to match the experimental model. The simulation results give evidence that the computational model constructed accurately represents real world physics. The validation simulations were run on the geometry created by Zhao and Lieber [119]. The simulation boundary conditions were set up to match the experiment of Lieber and Zhao [117].

The experiment run by Lieber and Zhao [117] was conducted on a single bifurcation (see ref [117]). A glycerin-water solution was pumped through the test section by a reciprocating pump. The reciprocating pump produced a sinusoidal inlet waveform (oscillatory flow). The glycerol solution entered the parent branch through a long straight tube and the flow at the outlets was set by two control valves. The measured flow rates in the two daughter branches were 48% in the left branch and 52% in the right branch. Velocities measurements were taken at key points in the domain using laser Doppler anemometry. For oscillatory flow in a tube the Reynolds number based on the oscillatory flow boundary layer thickness ($\mathrm{Re}_{\sim}$) is defined as [120]:

$$\mathrm{Re}_{\sim} = \alpha \frac{L}{(D/2)} \tag{4.1}$$

where D is the diameter of the tube, and L is the stroke length defined as:

$$L = \frac{V_T}{A} \tag{4.2}$$

where V_T is the tidal volume and A is the cross sectional area of the tube. The Womersley number α in Equation 4.1 is defined as [121]:

$$\alpha = (d/2)\sqrt{\frac{\omega}{\nu}} \tag{4.3}$$

where ω is the angular frequency (i.e. $\omega=2\pi f$, where f is the frequency), and ν is the kinematic viscosity. The transition to turbulent flow for oscillatory flows was estimated to occur somewhere between $Re_\omega=200$ and $Re_\omega=500$ [120]. In the experiment performed by Lieber and Zhao, $Re_\omega=483$, which suggests that turbulence is very likely to be present and play some role in the fluid dynamics, although Lieber reports that turbulence was not observed in their measurements [117].

4.4.1. Numerical Method. The geometry used for the grid convergence study (already based on the geometry of Zhao and Lieber [119]) was rescaled to match the scale of the experimental geometry (see Figure 4.2). The converged mesh was scaled along with the geometry to create the computational domain. Transient simulations were run on this computational domain with an oscillatory flow pattern matching the experimental V_T. Adaptive time stepping was used based on an RMS Courant number ~1 based on the results of the time step convergence study (§ 4.3). The large eddy simulation (LES) wall adapted local eddy-viscosity (WALE) model was used to model turbulence in the domain [105]. Numerical solver conditions were used as described in Chapter 3.

The walls were assumed to be smooth and rigid, and were modeled with a no slip condition. The inlet of the experimental domain was assumed to be long and so the

Womersley solution to oscillatory flow in a straight tube was imposed as a velocity condition at the inlet. The Womersley solution is defined as [121]:

$$u(r,t) = \text{Real}\left[\frac{1}{i\rho\omega}\left(1-\frac{J_0(\alpha r i^{\frac{3}{2}})}{J_0(\alpha i^{\frac{3}{2}})}\right)A^* e^{i\omega t}\right] \tag{4.4}$$

where ρ is the fluid density, i is $\sqrt{-1}$, and r is the non-dimensional radial distance such that r=0 in the center of the tube and r=1 at the wall. J_0 is the zeroth Bessel function of the first kind. The pressure gradient driving the flow is represented by the real part of $A^* e^{i\omega t}$. The parameter A^* can be determined by assuming a peak flow rate of Q=Re$_D$ $\pi Dv/4$ at a time where t/T=0.25, where Re$_D$ is the Reynolds number (Equation 4.1), D is the diameter, v is the kinematic viscosity and T is the period. This velocity profile was implemented in CFX® with a user FORTRAN subroutine given in APPENDIX B. The mass flow rates at the outlets were specified as a percentage of the mass flow rate at the inlet (i.e. 48% and 52% for the left and right outlets respectively).

4.4.2. Comparison with Experimental Work. Data was collected from the work by Lieber and Zhao [117] by collecting the ordered pairs for each data point and transforming them into a standard x-y coordinate system. Velocity profiles were recorded from the simulation for times $T/5$ and $7T/10$ at stations 2, 10 and 15 in both the bifurcation plane and the transverse plane. The recorded velocity profiles are compared with the experimental data in Figure 4.5. Visually the plots show good agreement with the experimental data. The percent difference between the simulations and the experimental work was calculated for each velocity profile and is tabulated in Table 4.3.

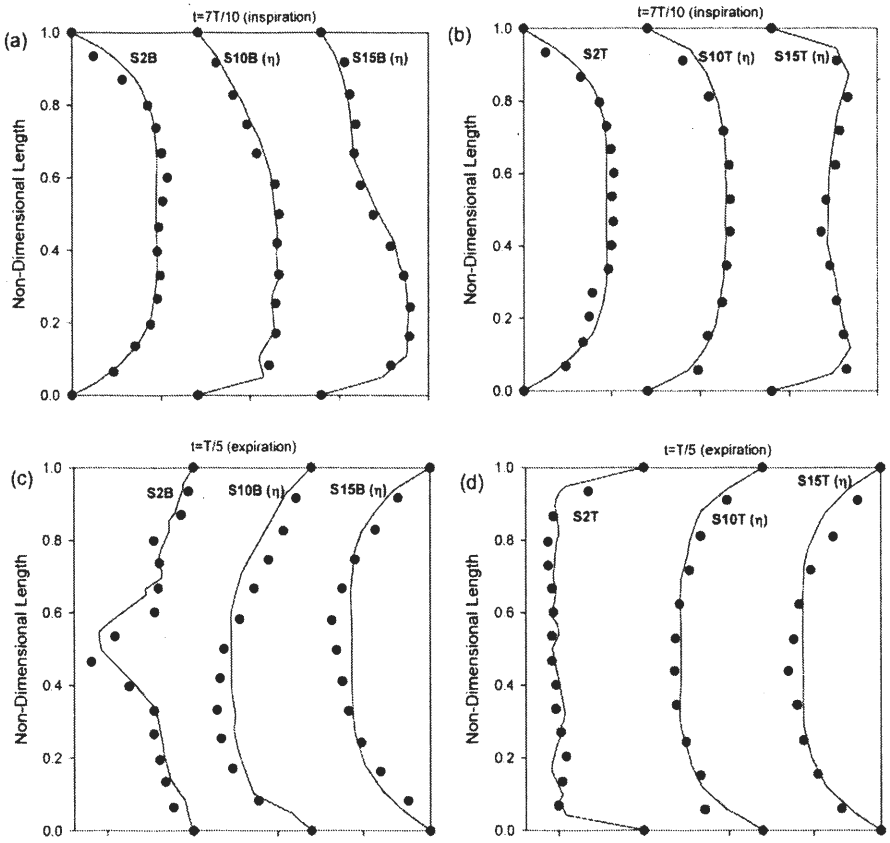

Figure 4.5: Validation plots. Circles represent laser Doppler anemometry measurements of velocity from Lieber and Zhao [117]; lines represent velocity profiles found by simulation. In the station designations "*B*" indicates that the station is in the bifurcation plane and "*T*" indicates it is in the transverse plane. (a) $t=7T/10$ (inspiration) in the bifurcation plane. (b) $t=7T/10$ (inspiration) in the transverse plane. (c) $t=T/5$ (expiration) in the bifurcation plane. (d) $t=T/5$ (expiration) in the transverse plane.

Table 4.3: Validation percent difference

station	Percent difference at t=7T/10	Percent difference at t=T/5
S2B	6.69%	20.73%
S10B	6.20%	19.69%
S15B	6.35%	14.24%
S2T	7.57%	7.04%
S10T	6.52%	8.67%
S15T	6.17%	13.66%

4.5. FLUID FLOW

Important flow features and turbulence will play a part in guiding the particles along their paths through the domain. The presence and magnitude of the flow features and turbulence vary throughout the respiratory cycle. This section will discuss important fluid flow features observed in the results of the waveform simulations and look at the role of turbulence in the domain throughout the respiratory cycle.

4.5.1. Important Fluid Structures. The dominant flow features that were apparent throughout inspiration were:

(a) the jet caused by the endotracheal tube (ETT jet)

(b) the large rotating structure in the right main bronchus, and

(c) swirling flows in the bronchi.

The ETT jet is similar to the laryngeal jet which has been studied in the past [30, 82-85]. Both the laryngeal jet and the ETT jet cause a flow constriction and release fluid into a larger environment at a high speed. The ETT jet is different from the jet caused by the larynx because of its proximity to the carina and its range of orientation is dependent upon how the tube was installed or how the patent is positioned. A structure similar to the large rotating structure in the right main bronchus was reported by Xi *et al* [30] in the trachea, and is believed to be caused by the laryngeal jet. The swirling flows in the bronchi, at times, resemble Dean vorticies [122], however some of the swirling is thought to result from the noncircular geometry of the airways as well as flow curvature effects. The presence and the magnitude of the ETT jet, the large rotating structure in the right main bronchi, and the swirling flows in the bronchi vary throughout the inspiratory

phase. During expiration the swirling in the bronchi remained and the endotracheal tube caused a constriction in the flow as it exited the domain.

For purposes of demonstrating the presence and development of these flow features the results from the flow control ascending ramp waveform were used. Velocity vectors throughout the domain were plotted at several times. They are colored by velocity magnitude and the size of the vectors scales with the velocity magnitude. Figure 4.6 shows the early stages of the ETT jet. It is clear that the jet is pointed towards the right main bronchus due to the orientation of the endotracheal tube. An ETT jet pointed towards the right main bronchus is common because path to the right main bronchus from the trachea is more direct for most patients, although this depends largely upon how the ETT was installed. The large rotation in the right main bronchus has not yet developed and swirling activity in slices L-L or R-R is not present at this early time (t=0.05 s).

Figure 4.7 demonstrates the development of the ETT jet. The jet has advanced to just above slice R-R and is about to impinge on the wall of the right main bronchus. The large rotation in the right main bronchus has still not developed and swirling activity in slices L-L or R-R is not present at this time (t=0.075 s).

After the ETT jet impinges on the wall of the right main bronchus it begins to disperse. Jet impingement and dispersion was observed by Choi [28]. Figure 4.8 shows the dispersal of the ETT jet. A low grazing angle and the orientation of the surface where the jet contacts the wall causes the jet to be deflected to the right lung; forming a secondary jet. The maximum velocity in this secondary jet is much less than that of the ETT jet. The shape of the ETT jet as it passes through slice R-R can be seen in Figure

4.8. The rotation in the right main bronchus begins to develop, but the swirling flow in slice L-L is not yet present.

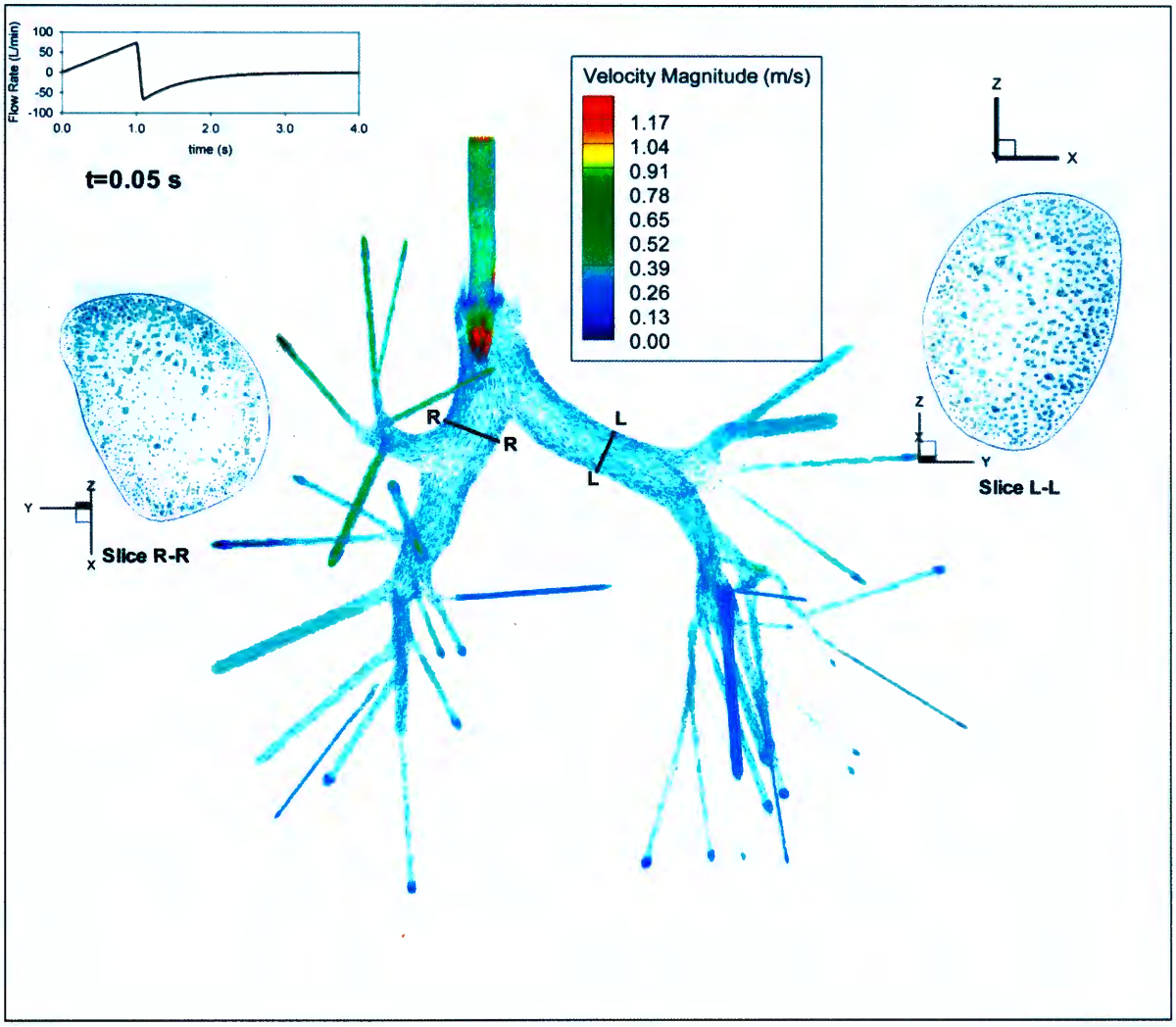

Figure 4.6: Velocity vectors at time t=0.05 s. For the flow controlled ascending ramp waveform. Vectors are colored by velocity magnitude.

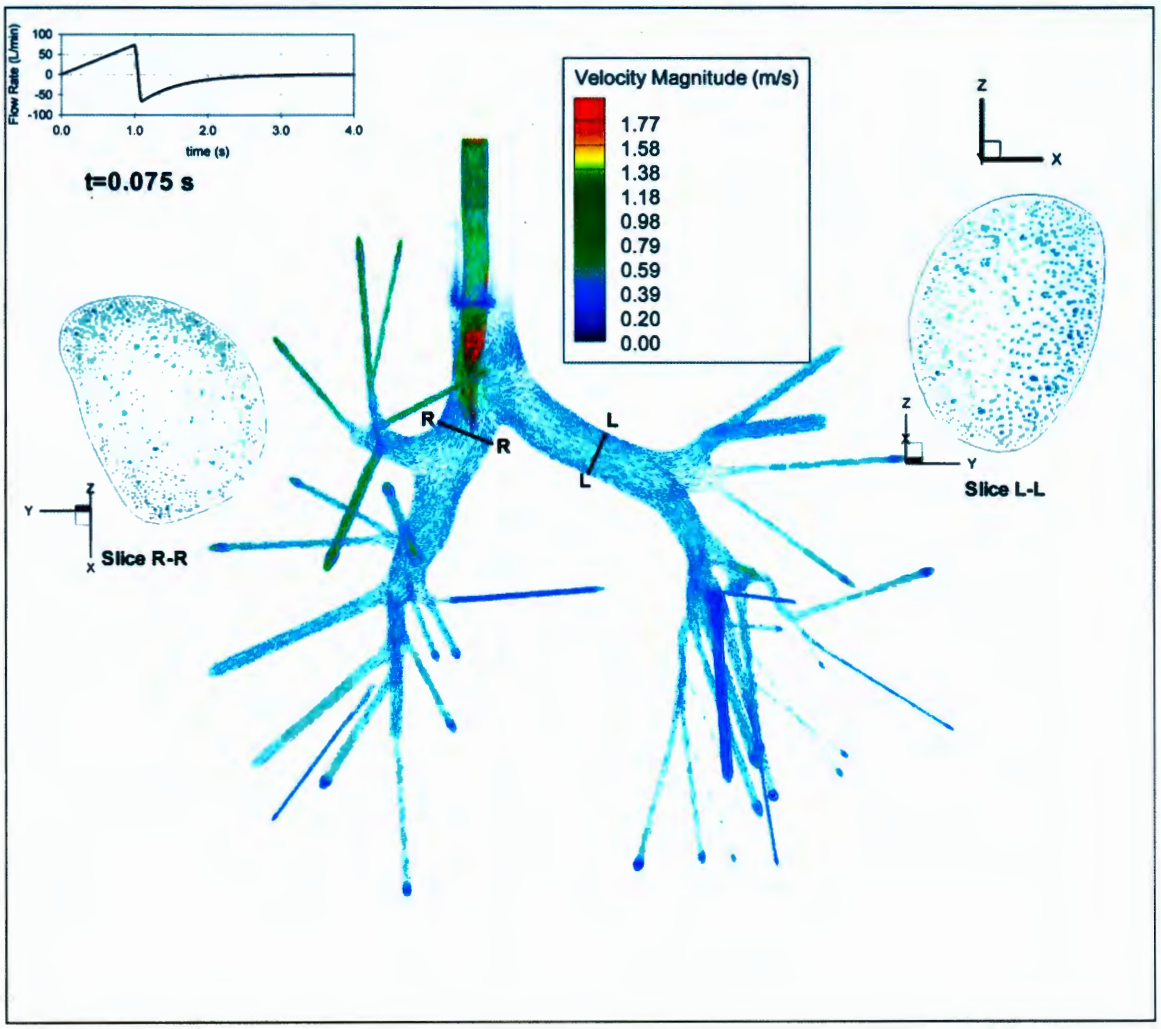

Figure 4.7: Velocity vectors at time t=0.075 s. For the flow controlled ascending ramp waveform. Vectors are colored by velocity magnitude.

At t=0.2 s the secondary (deflected) jet has impinged in the lower part of the right main bronchus where the airway turns toward the anterior side of the patient which can be seen in Figure 4.9. The jet disperses and there is no noticeable deflected jet. The dispersed secondary jet begins to flow back upward to the airways of the right upper lobe and to the left main bronchus. It is important to note that a large portion on the flow entering the left main bronchus does not come directly from the ETT but rather, passes

first through the right main bronchus before recirculating, passing over the carina of the first bifurcation, and entering the left main bronchus. The downward flow of the ETT jet and the upward flow of the dispersed secondary jet are what make up the large rotating structure in the right main bronchus. The flow through slice L-L in Figure 4.9 shows a counterclockwise swirling. The shape of the ETT jet as well as the upward flow can be seen in slice R-R.

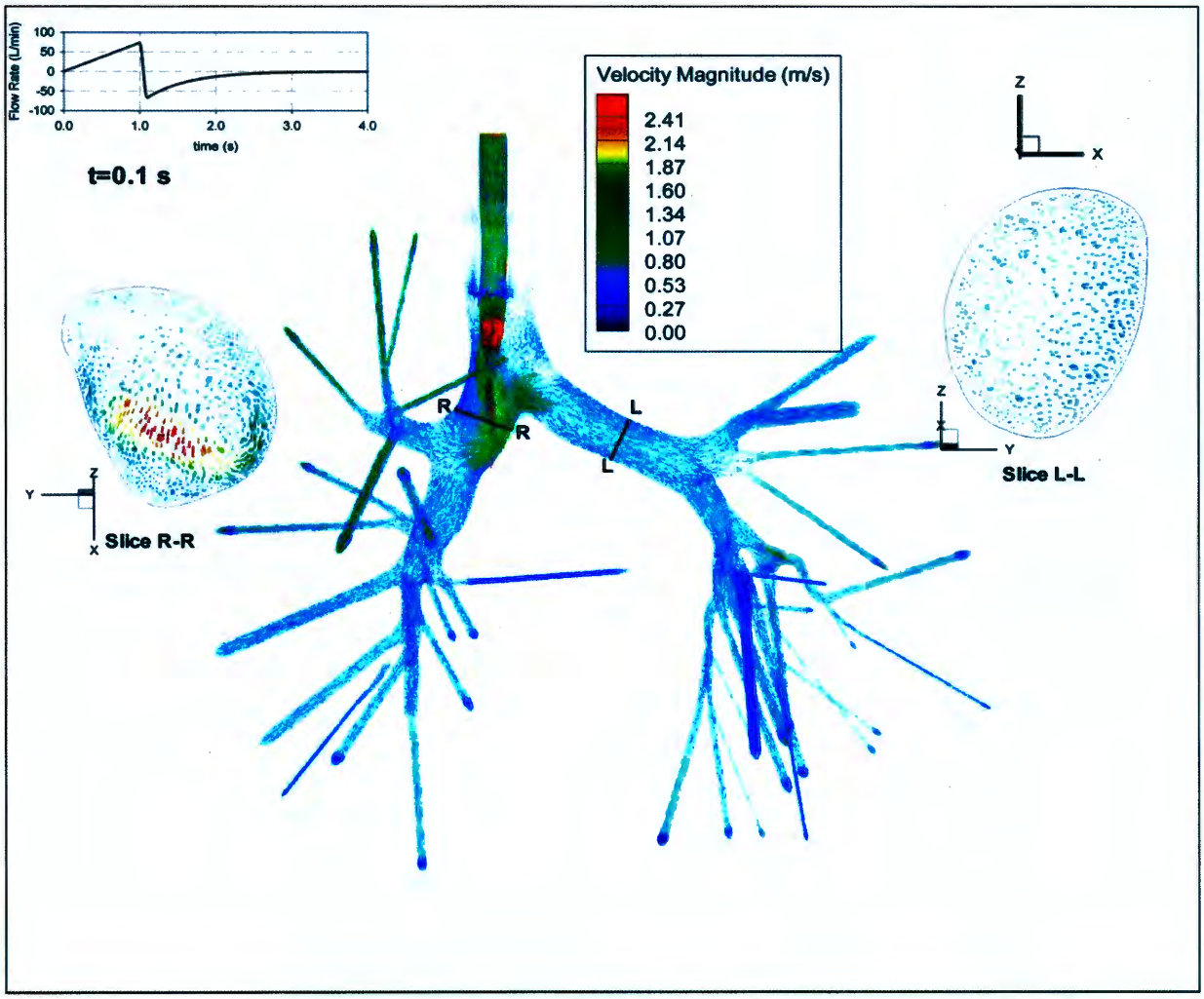

Figure 4.8: Velocity vectors at time t=0.1 s. For the flow controlled ascending ramp waveform. Vectors are colored by velocity magnitude.

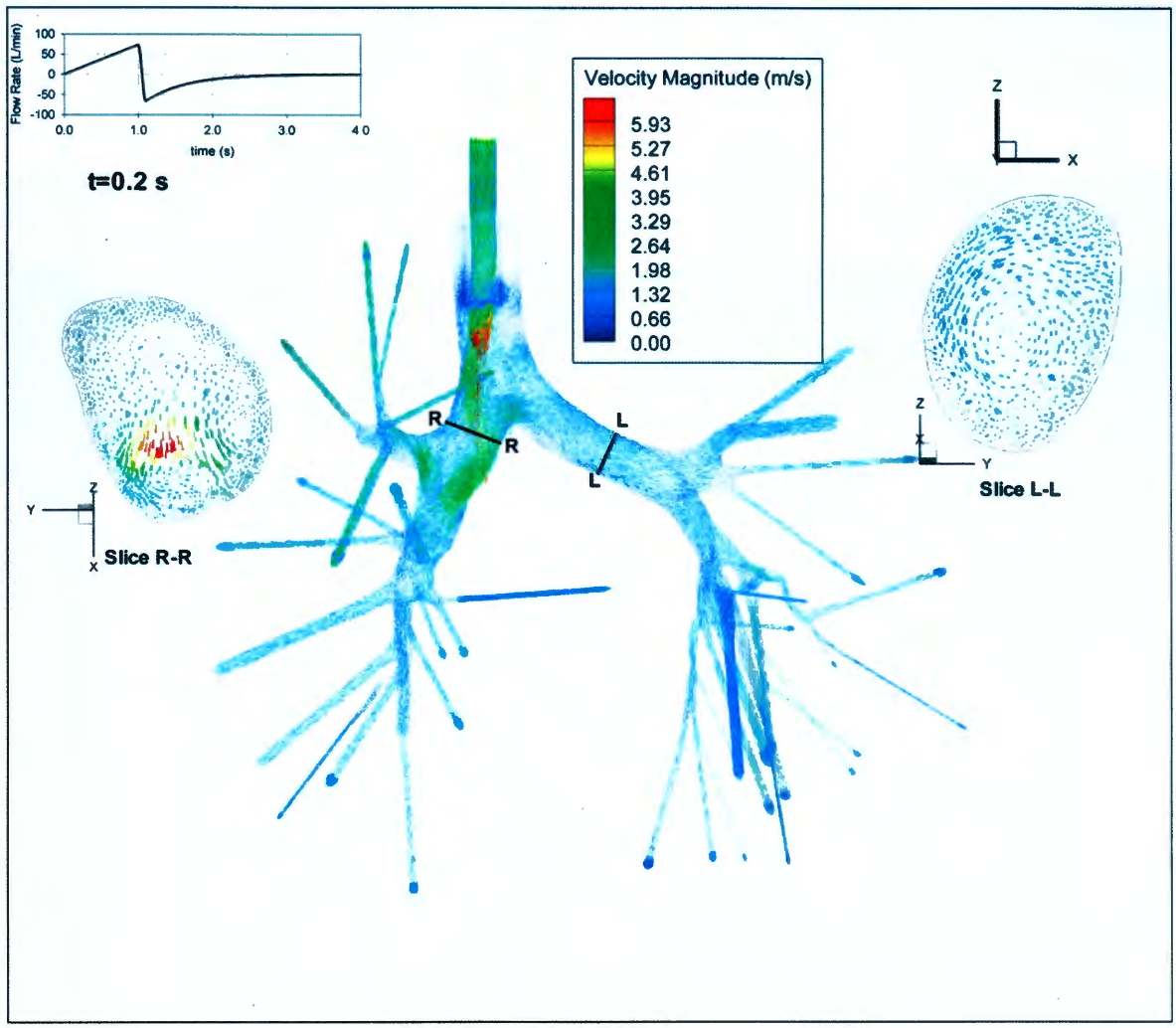

Figure 4.9: Velocity vectors at time t=0.2 s. For the flow controlled ascending ramp waveform. Vectors are colored by velocity magnitude.

By t=0.4 s the ETT jet and the rotation in the right main bronchus are developed as can be seen in Figure 4.10. The swirling at slice L-L has developed with two counter-rotating flows, one at the top of slice L-L rotating counterclockwise and the other at the bottom of slice L-L rotating clockwise. Similar structures are commonly found in flows through curved pipes and are known as Dean vortices [122]. The ETT jet, the rotation in the right main bronchus, and the swirling pattern at slice L-L do not change in structure

throughout the remainder of inspiration, however their vorticity will change. Similar flow features were observed for all waveforms. The development of these features was also similar for all waveforms. However, the rate at which they developed varied based on how quickly the flow waveform accelerated, as discussed next.

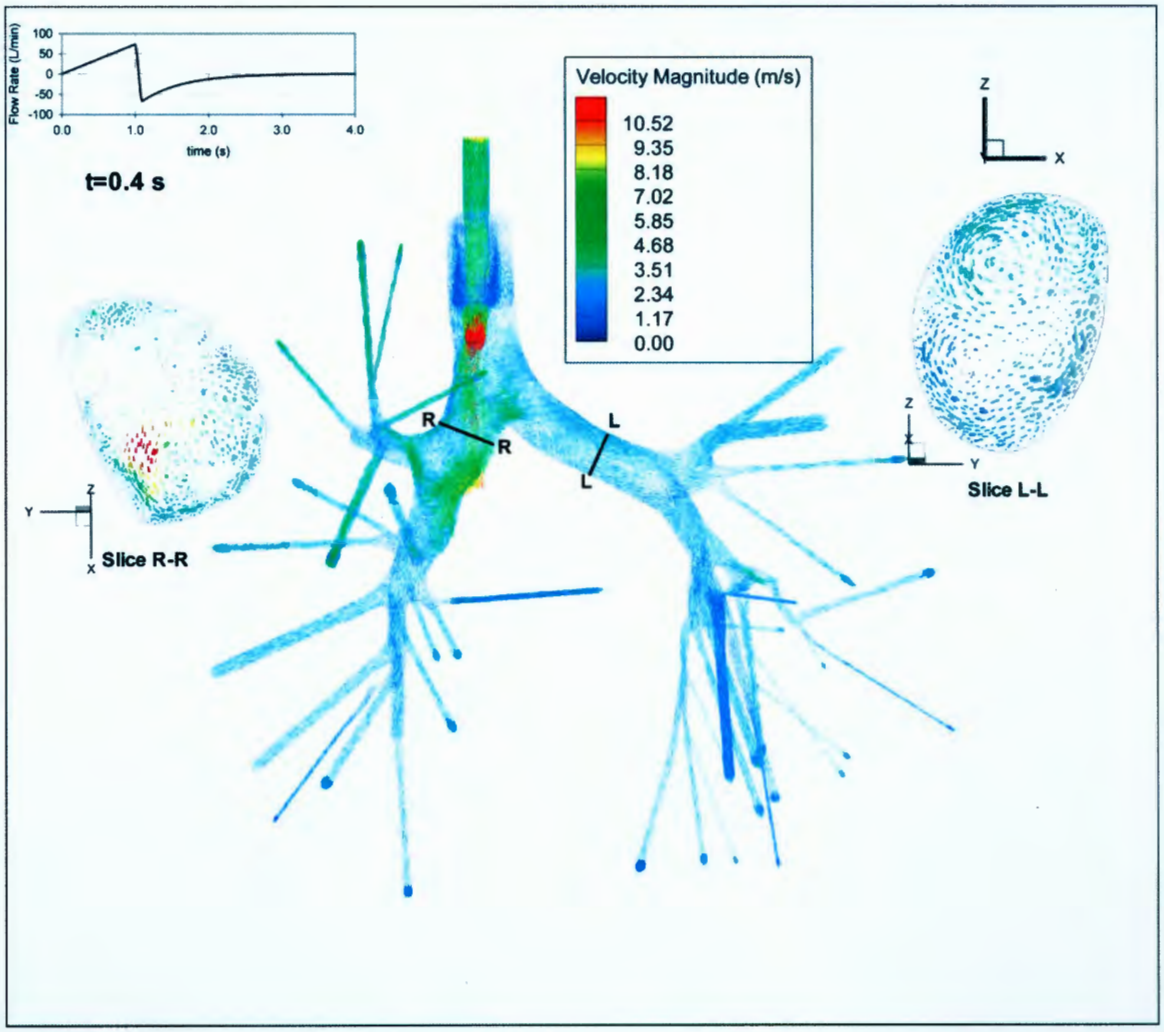

Figure 4.10: Velocity vectors at time t=0.4 s. For the flow controlled ascending ramp waveform. Vectors are colored by velocity magnitude.

The velocity vectors throughout the domain for the pressure controlled sinusoidal waveform near the end of inspiration (t=1.8 s) are shown in Figure 4.11. The flow rate is similar to that of the flow controlled ascending ramp waveform at t=0.1 s (Figure 4.8). The ETT jet, the rotation in the right main bronchus, and the swirling pattern at slice L-L are all developed in Figure 4.11 and resemble those at t=0.4 s for the flow controlled ascending ramp waveform (Figure 4.10). It is clear that the presence and strength of the flow features are not only dependent upon the inspiratory flow rate, but also the history of the flow.

The fluid flow features throughout expiration are very similar for all of the waveforms due to the nearly identical waveform shapes during expiration. The pressure controlled sinusoidal waveform was different than the others for expiration; however, the flow features were still similar. The velocity vectors throughout the domain for the pressure controlled constant waveform at peak expiration are shown in Figure 4.12. The swirling in slice L-L can still be seen in Figure 4.12 as well as the constriction in the flow as it entered the endotracheal tube. When flow from a daughter branch enters the parent branch it forms a small jet-like structure. This is most noticeable when there is a sharper transition in airway diameter. In the present model these small jets are most visible in Figure 4.12 in the most distal branches of the right and left upper lobes. These jets dissipate very quickly due to the smooth transitional shapes of the bifurcations and are more noticeable at higher flow rates.

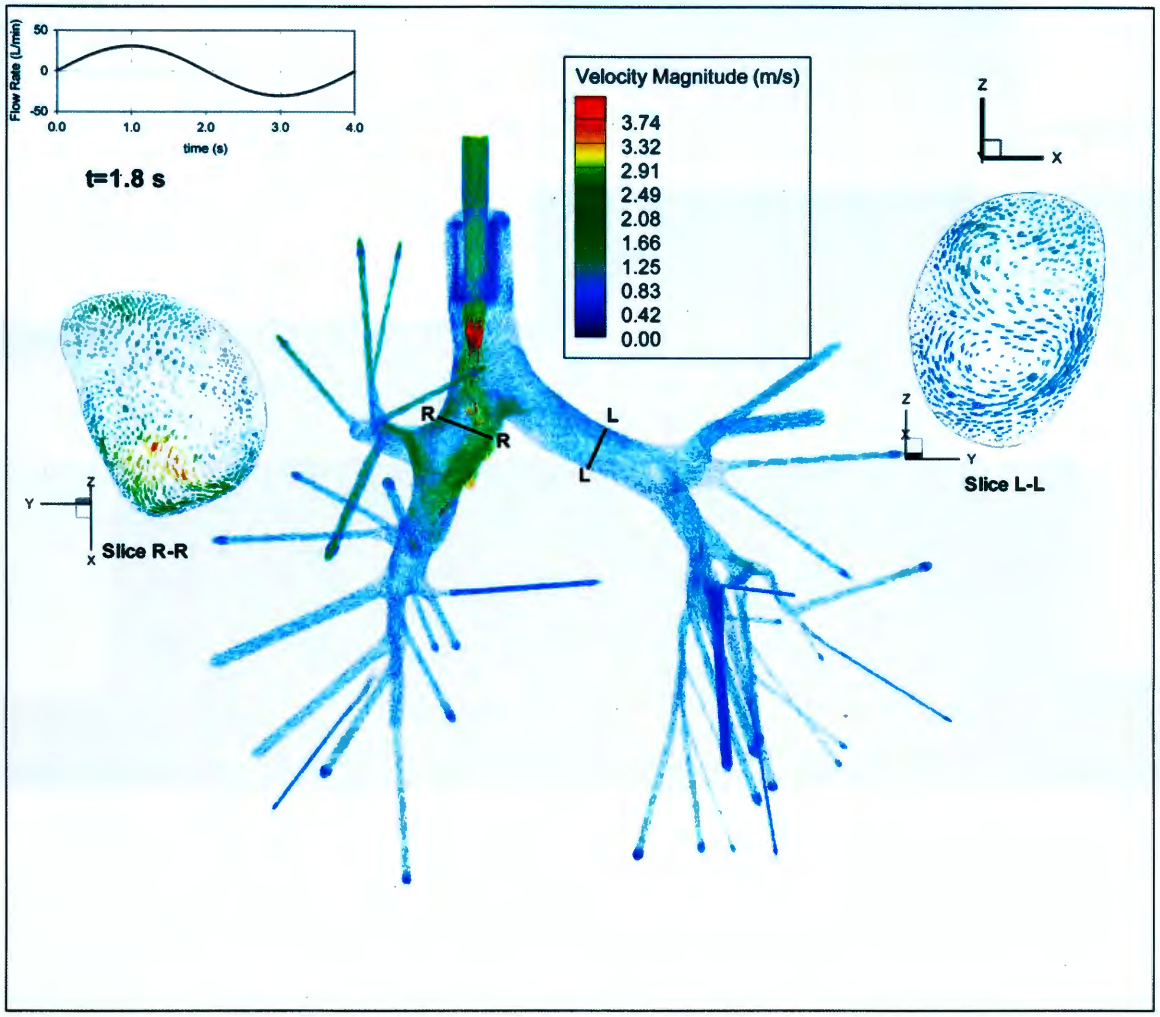

Figure 4.11: Velocity vectors at time t=1.8 s. For the pressure controlled sinusoidal waveform. Vectors are colored by velocity magnitude.

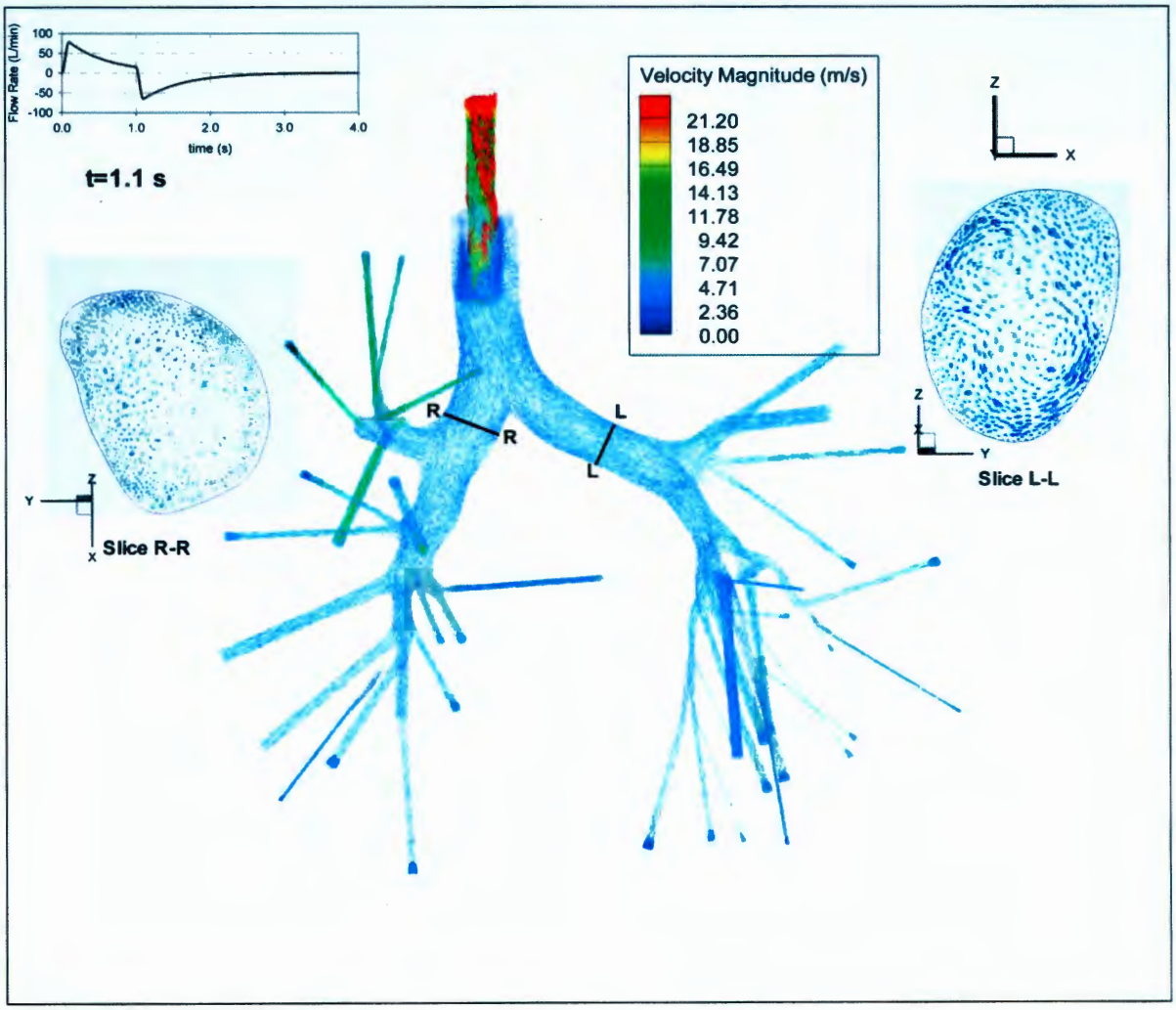

Figure 4.12: Velocity vectors at time t=1.1 s. For the pressure controlled constant waveform. Vectors are colored by velocity magnitude.

4.5.2. Turbulence. To characterize flow turbulence, turbulence kinetic energy (TKE) and vorticity were evaluated in slices through the domain. Turbulent kinetic energy k is defined as:

$$k = \tfrac{1}{2}\overline{u_i' u_i'} \tag{4.5}$$

where the prime symbol indicates a fluctuation and the overbar indicates a mean. Vorticity, ω, is defined as:

$$\omega = \nabla \times u \tag{4.6}$$

Contours of TKE for each waveform at peak inspiration are shown in Figure 4.13 and Figure 4.14 (e-g). There is a strong TKE around the edges of the ETT jet. TKE in the human airways downstream of a jet (laryngeal) has been reported by Lin [83]. The ETT jet is released far below the larynx in the trachea and, in this study, is aligned with the opening of the right main bronchus. Because of the position and orientation of the ETT, the TKE remains strong much lower into the airways when compared with the TKE caused by the laryngeal jet. In addition, there is much more TKE in the right lung.

As the ETT jet impinges and deflects the TKE begins to dissipate rapidly similar to the dissipation seen after the laryngeal jet impinges on the back of the trachea [83]. The areas of highest TKE are those where the incoming ETT jet begins to interact with the deflected and dispersed flow coming upward out of the right main bronchus and across the path of the ETT jet. A similar flow pattern was reported by Xi where the highest turbulence viscosity ratio in the flow was reported [30]. High TKE remains throughout most of the portion of the right lung modeled in this study and through some of the left main bronchus. In general the TKE is stronger with the waveforms that have a higher maximum flow rate. The patterns of TKE throughout the domain for the different waveforms are similar.

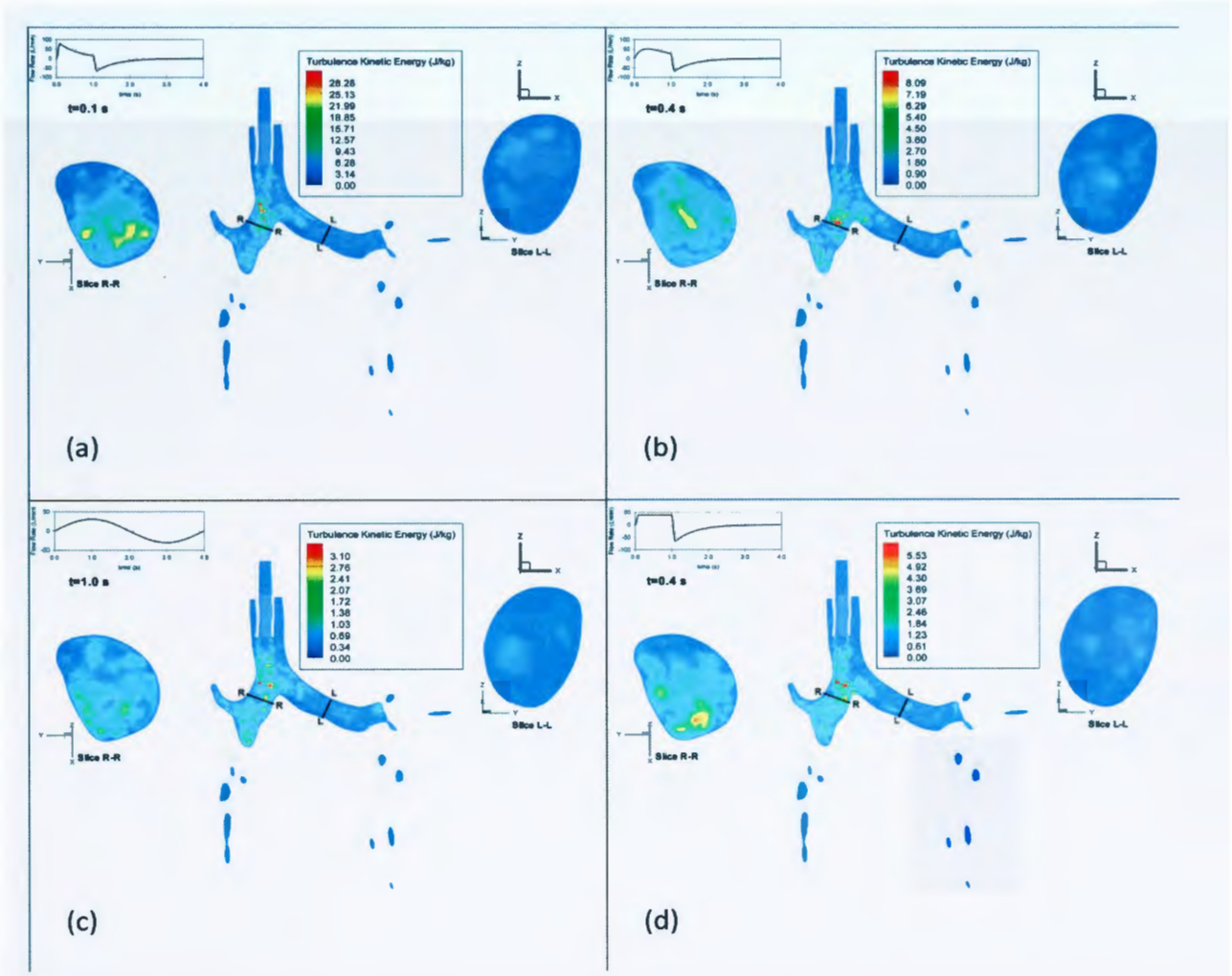

Figure 4.13: Contours of turbulence kinetic energy. For (a) pressure controlled constant at peak inspiration, (b) pressure controlled exponential at peak inspiration, (c) pressure controlled sinusoidal at peak inspiration, and (d) volume controlled ramp at peak inspiration

The TKE for the pressure controlled constant waveform at peak expiration is shown in Figure 4.14 (h) as an example. The TKE contours for the other waveforms were very similar to the pressure controlled constant case. The TKE for the pressure controlled sinusoidal waveform was also similar in structure but had lower values of TKE. The TKE present in inspiration is stronger than the turbulence for expiration (~1.5 times) even though the peak flow rate for inspiration is on average about 97% of the peak

flow rate during expiration. The difference in the TKE during inspiration and expiration is attributed to the presence of the ETT jet. Areas of highest TKE in expiration occur when the flows from the daughter braches into the parent branches begin to mix and in the ETT where the flow is suddenly constricted creating a high flow velocity. The production of TKE due to the mixing of daughter branch flows can be seen in Figure 4.14 (h) in the upper right lobe and in the left main bronchus for example.

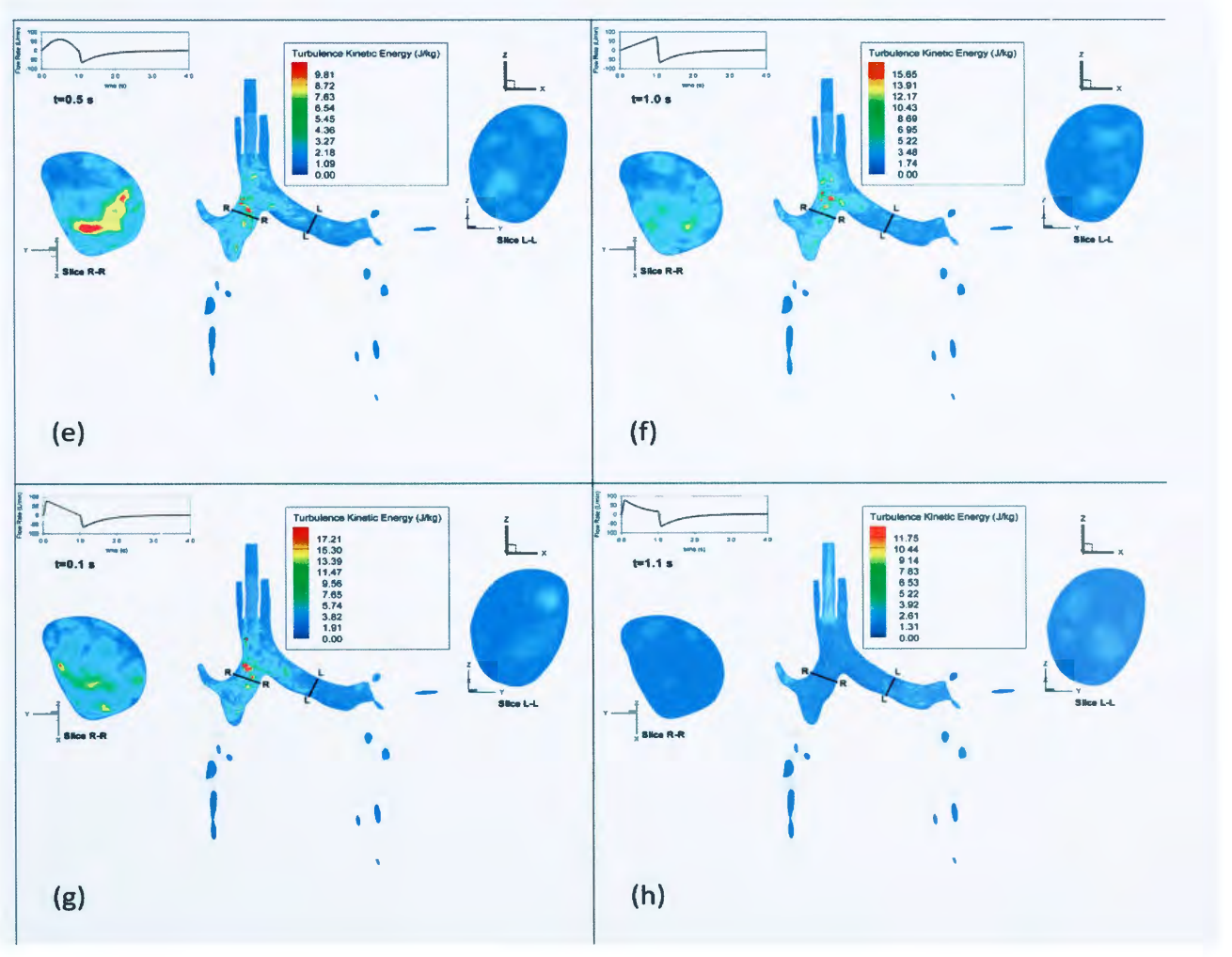

Figure 4.14: Contours of turbulence kinetic energy. For (e) volume controlled sigmoid at peak inspiration, (f) flow controlled ascending ramp peak inspiration, (g) flow controlled descending ramp peak inspiration, and (h) pressure controlled constant at peak expiration

Contours of vorticity for each waveform at peak inspiration are shown in Figure 4.15 and Figure 4.16 (e-g). Higher vorticity exists in the right lung in inspiration for every waveform due to the ETT jet. Areas of high vorticity exist in the middle of the domain around the edges of the ETT jet and at the walls of the domain. Higher near wall vorticity exists where higher near wall velocities are present. One area of high vorticity exists where the ETT jet impinges and deflects off the wall of the right main bronchus (See Figure 4.15 and Figure 4.16 e-g). In the waveforms with higher peak flow rates (i.e. pressure controlled constant, flow controlled ascending ramp, and flow controlled descending ramp) the vorticity suddenly drops near the bottom of the wall where the ETT jet is being deflected as the secondary jet detaches from the wall (Figure 4.15 (a) Figure 4.16 (f) and (g)). This behavior is not observed in the waveforms with a lower flow rate. A similar pattern occurs at the first bifurcation as the flow coming from the right lung passes over the carina. Another patch of high vorticity is observed at the top of the left main bronchus.

Contours of vorticity for the pressure controlled constant waveform at peak expiration are shown in Figure 4.16 (h) as an example. For the other waveforms, vorticity was very similar in expiration. Expiration for the pressure controlled sinusoidal waveform had vorticity that was also similar in structure but had smaller values for vorticity. The highest vorticity for expiration existed in the ETT where the highest velocity existed. Vorticity was also present in the left main bronchus where there was more significant swirling motion due to geometry.

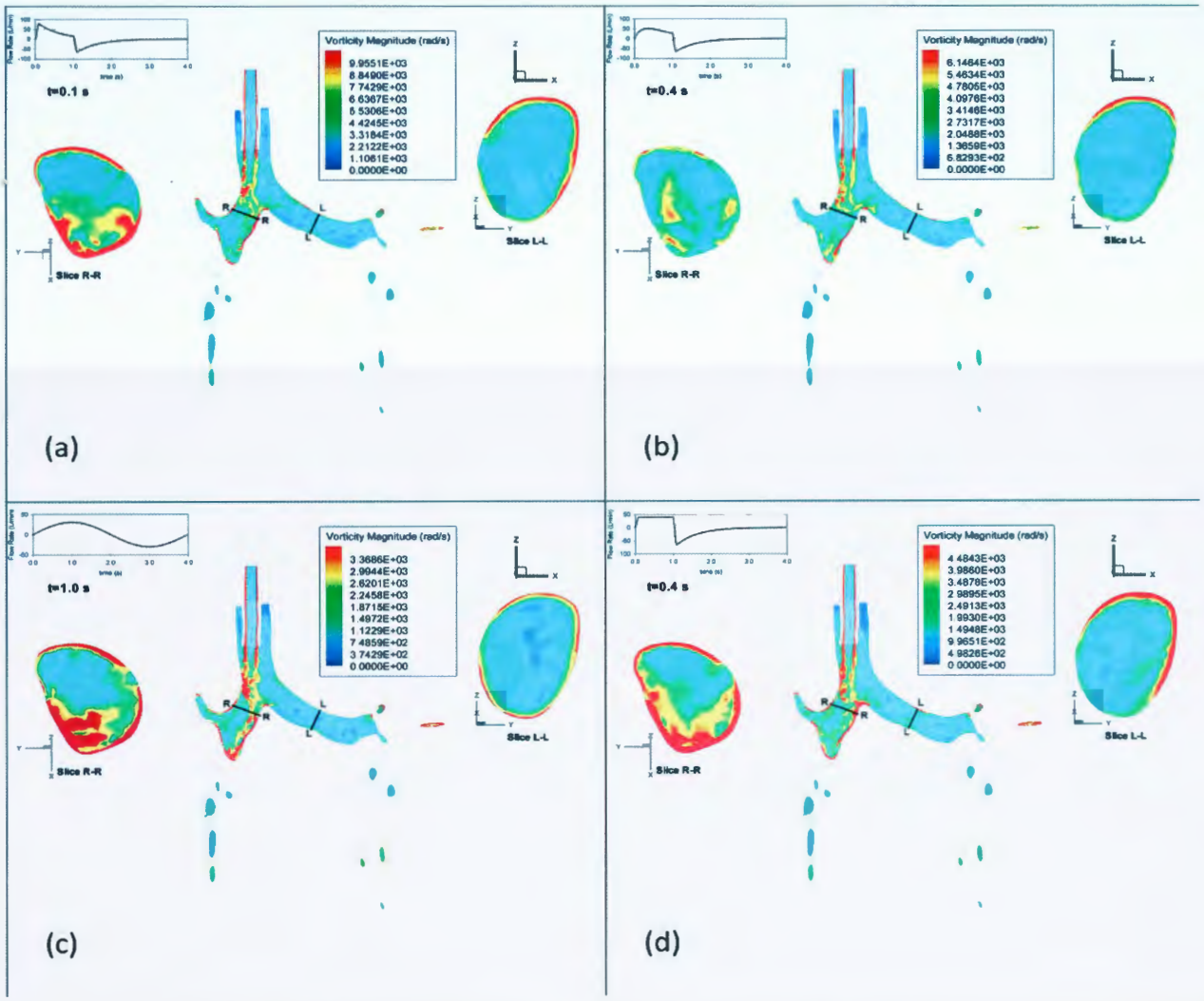

Figure 4.15: Contours of vorticity. For (a) pressure controlled constant at peak inspiration, (b) pressure controlled exponential at peak inspiration, (c) pressure controlled sinusoidal at peak inspiration, and (d) volume controlled ramp at peak inspiration

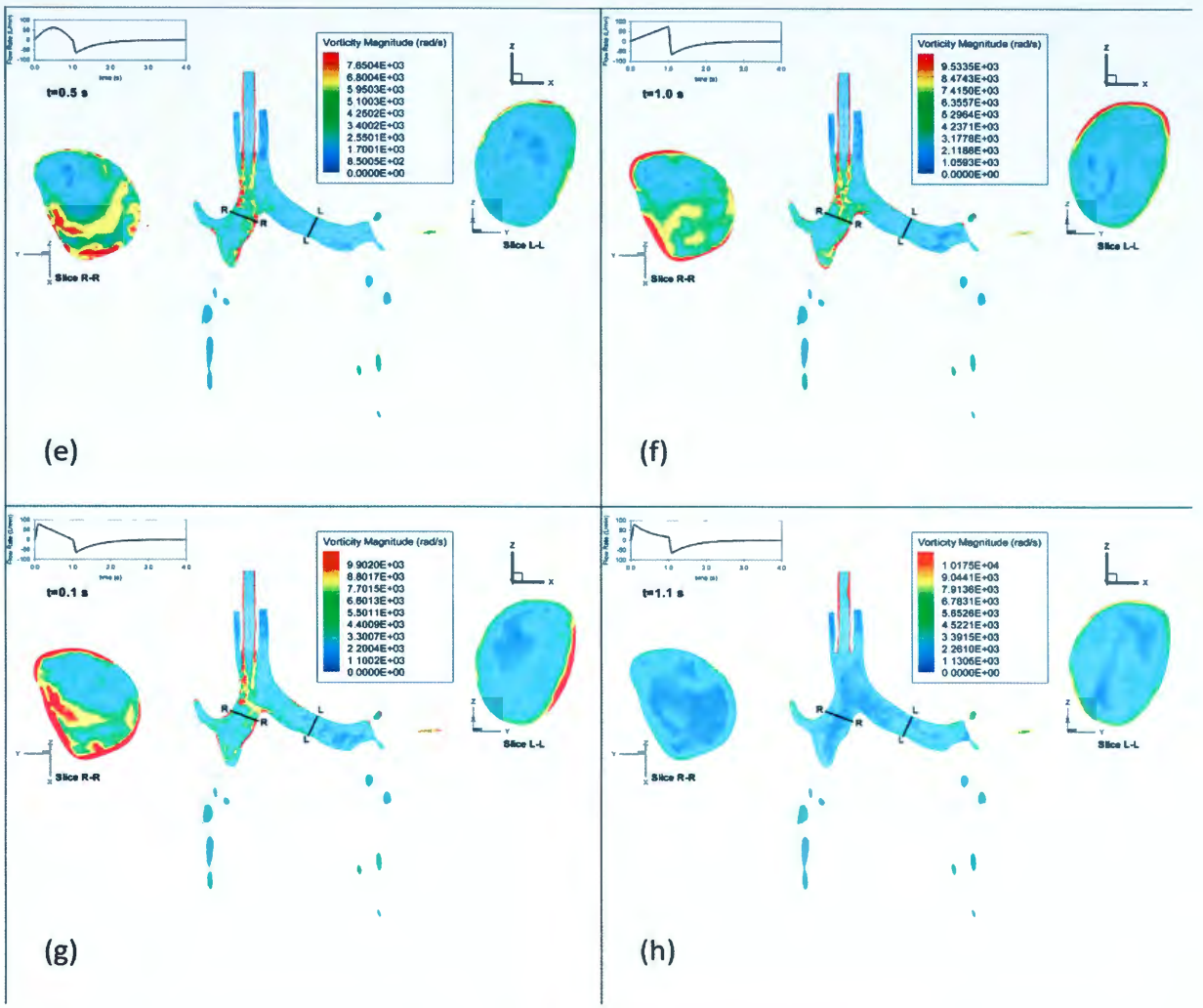

Figure 4.16: Contours of vorticity. For (e) volume controlled sigmoid at peak inspiration, (f) flow controlled ascending ramp peak inspiration, (g) flow controlled descending ramp peak inspiration, and (h) pressure controlled constant at peak expiration

4.6. PARTICLE DEPOSITION

Next, we discuss the results obtained from the particle tracking algorithm that was developed, and discussed in § 3.2. The end statuses of the particles as well as their global and local depositions will be discussed. Because of the added computational expense, particle transport and deposition was only simulated for cases: (a) pressure controlled

constant, (b) pressure controlled sinusoidal, (c) volume controlled ramp, and (d) flow controlled ascending ramp waveforms. The pressure controlled constant and volume controlled ramp cases were selected because they are the most frequently used, the pressure controlled sinusoidal waveform was chosen because of the low flow rates, and the flow controlled ascending ramp case was selected because it had similar peak flow rates to the pressure controlled constant case, but the shape of the flow rate curve is very nearly reversed in time during inspiration.

4.6.1. Particle End Status. Particles that were injected into the domain took on one of five end statuses: (1) deposited on the walls, (2) escaped through one of the outlets, (3) exceeded the particle tracking distance limit (100 m), (4) exceeded the maximum number of integration steps (1×10^6 steps), or (5) encountered an integration error. The integration errors occur when the particle velocity is too small ($\rightarrow0$) and may occur when a particle is injected very close to the wall with a velocity $\rightarrow0$. Particles may have exceeded the distance limit or the maximum number of integration steps when caught in a recirculation zone.

The overall particle end statuses for each simulation are summarized in Table 4.4. In all four cases, the number of particles that neither deposited nor escaped was <5%. Particles that are deposited on the walls of the model are assumed to flow with the mucus lining and rendered ineffective as medication [123]. Particles escaping from the domain to the lower airways have a chance of depositing in the lower airways or diffusing into the bloodstream for systemic delivery. There have been studies conducted to investigate particle deposition in the lower airways; however these studies do not focus on the effect of inspiratory waveform [64, 124-125]. Of the waveforms in this study, the waveform

that allowed the largest number of particles to escape from the domain (i.e. the maximum efficiency of delivery to the lower airways) is the pressure controlled sinusoidal waveform. The relatively low flow rates throughout the pressure controlled sinusoidal waveform reduced the role of impaction. The lower flow rate of the pressure controlled sinusoidal waveform causes increased particle residence times and may result in a slightly higher deposition of submicron particles by diffusion, however the lower flow rate also corresponds with a decrease in turbulent mixing which will reduce the role of turbulent diffusion and turbophoresis [30, 58].

Table 4.4: Particle end statuses. Percentage of total number of particles to enter the domain

Waveform	Deposited	Escaped	Exceeded Distance Limit	Exceeded Max # of Integration Steps	Integration Error
Pressure Controlled: Constant	56.03%	40.86%	3.01%	0.08%	0.01%
Pressure Controlled: Sinusoidal	39.88%	55.63%	4.33%	0.16%	0.00%
Volume Controlled: Ramp	53.85%	42.82%	3.23%	0.10%	0.01%
Flow Controlled: Ascending Ramp	57.29%	39.75%	2.88%	0.07%	0.01%

The particle end statuses, as they occur over time, are shown for the four waveforms in Figure 4.17. The number of particles entering the domain is directly related to the flow rate, so the rate of particles entering the domain is the same shape as the flow rate waveform and the total number of particles that have entered the domain is the same shape as the volume waveform. An offset is observed between the entry rate curve and the deposition rate curve, and between the entry rate curve and the escape rate curve, primarily due to the difference in location between the sites of the events. Entry occurs at the inlet, deposition usually occurs where the ETT jet impinges on the wall of the right main bronchus or at one of the carinas, and escape occurs at the outlets. The offset for the deposition rate curve is less than the offset for the escape rate curve because of the shorter distance the particles need to travel before deposition as compared to the distance traveled for escape. Very little offset is observed between the deposition and escape rate curves for the waveforms that maintain a low flow rate at the onset of inspiration (i.e. pressure controlled sinusoidal and flow controlled ascending ramp) because the particles will pass by many of the sites that are deposition hot spots and move close to the outlets before the flow rate becomes high enough to cause significant impaction. Deposition occurs much more quickly than escape in the waveforms with a higher flow rate near the onset of inspiration (i.e. pressure controlled constant and volume controlled ramp) because so many of the particles will deposit before reaching the outlets.

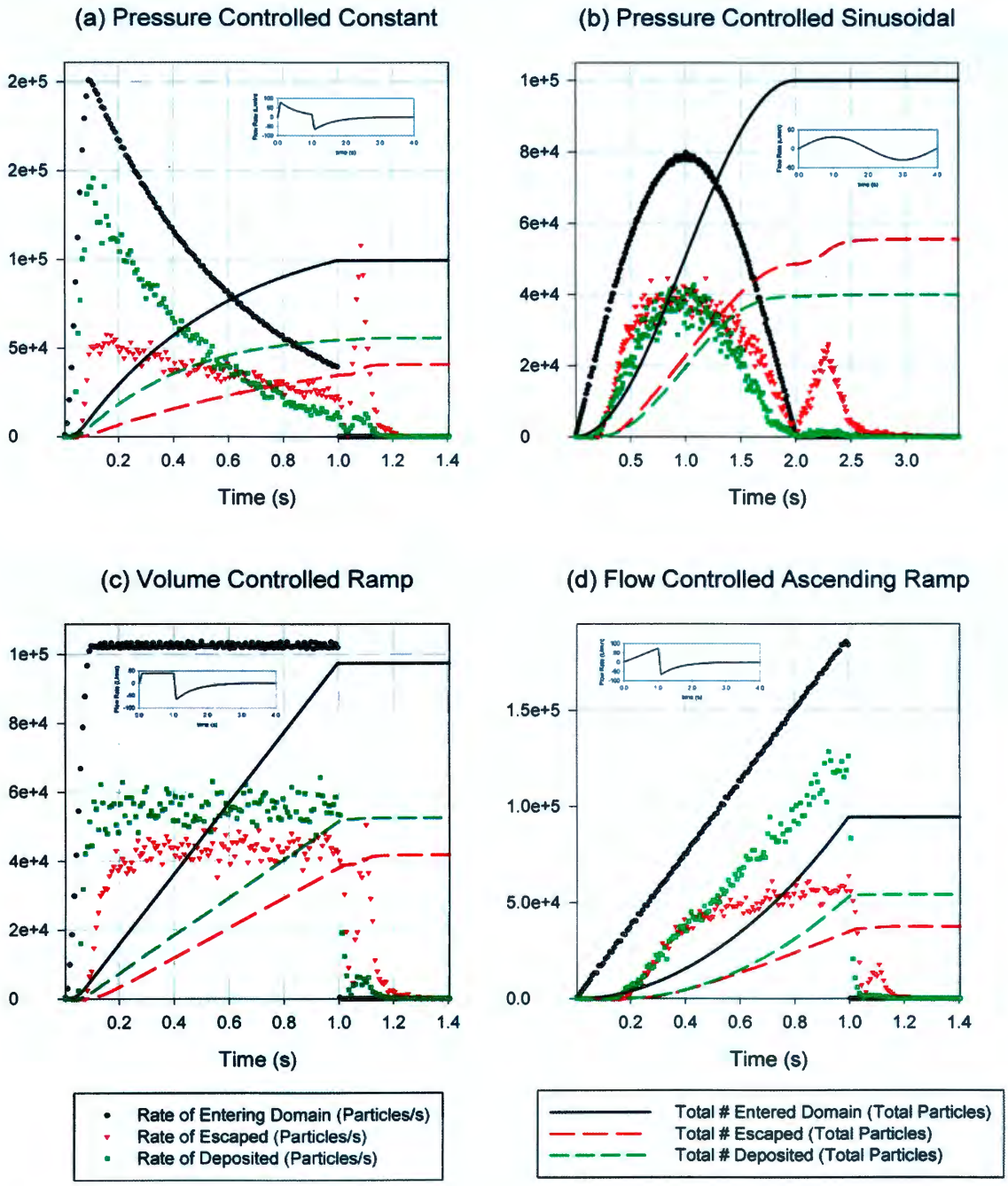

Figure 4.17: Particle end status for different waveforms. Data points represent the rate of particles entering, escaping, or depositing. Lines represent the sum of all of the particles that have entered, escaped, or deposited.

The slope of the deposition rate curve generally follows the flow rate curve. An increase in flow rate causes increased deposition because of the increased number of particles entering the domain and because of the increase in impaction, turbulent dispersion and turbophoresis. The escape rate also increases with the flow rate but the slope of the escape rate curve does not keep up with the slope of the flow rate curve at higher flow rates because of the higher number of particles depositing before reaching the outlets. This is most easily observed in Figure 4.17 (d) where there is clear separation of the deposition and the escape rate curves at approximately t=0.5 s.

At peak expiration, the deposition rates in Figure 4.17 are much lower than at peak inspiration, despite the high flow rates. This behavior is due to the decrease in potential impaction sites (most notably the carinas) and the reduction in turbulence (Figure 4.14) including the absence of the large recirculation zone in the right main bronchus (Figure 4.12). The reduction in the deposition rate along with the high flow rate causes a high escape rate in expiration (Figure 4.17). An additional factor that contributes to the high escape rate at peak expiration is the higher percentage of small particles that did not impact in inspiration. In the pressure controlled constant (Figure 4.17 (a)) and volume controlled ramp (Figure 4.17(c)) waveforms the highest escape rate is reached in expiration because of the large population of particles in the domain just before expiration. This high population of particles can be seen in Figure 4.18 and is caused by a long period of low flow rate. The pressure controlled sinusoidal waveform also has a large population of particles just before expiration and high escape rate is still seen despite the slow flow acceleration.

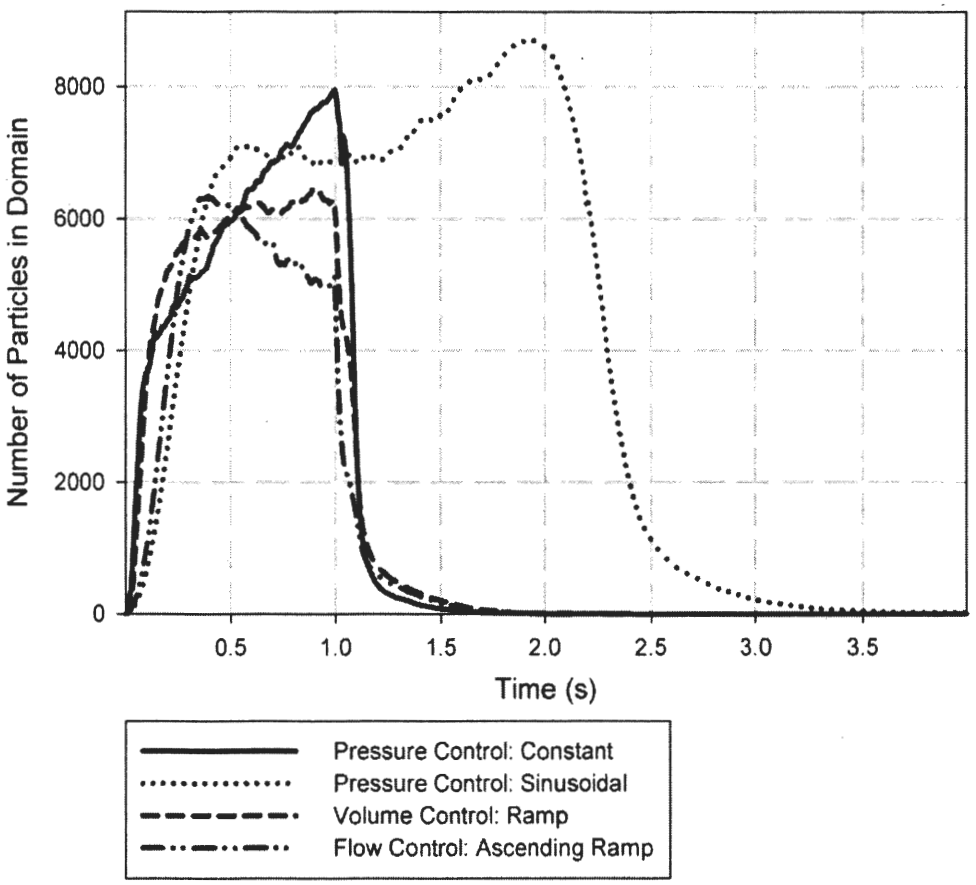

Figure 4.18: Number of particles in the domain as a function of time

4.6.2. Global Deposition. The most commonly used parameter to characterize global particle deposition is the deposition fraction, defined as the ratio of number of particles that have deposited in the domain to the number of particles that have entered the domain. The overall deposition fraction for each simulation is given in Table 4.5. The deposition fractions for the pressure controlled constant and the flow controlled ascending ramp waveforms were found to be similar at ~56 %. Because the volume controlled ramp waveform does not reach as high of a flow rate, the deposition fraction is

slightly lower at ~53.85 %. The deposition fraction for the pressure controlled sinusoidal waveform is significantly lower than the others due to the lower flow rates in inspiration ~39.88 %.

Table 4.5: Overall deposition fractions

Waveform	Overall Deposition Fraction
Pressure Controlled: Constant	56.03%
Pressure Controlled: Sinusoidal	39.88%
Volume Controlled: Ramp	53.85%
Flow Controlled: Ascending Ramp	57.29%

Deposition fraction histograms were created to show the relationship between Stokes number (defined in § 1.3.3) and deposition fraction (Figure 4.19). The same data is also presented in Figure 4.20 for easy comparison between the different waveforms. Deposition fractions as a function of particle diameter or Stokes number have been reported in other studies (e.g. [23, 30, 33, 70, 87]). Of these studies only the one by Li *et al* [87] used an unsteady inlet condition. Geometric differences such as curvature and size of the airways, shapes of the carinas, branching angles, and overall size (area) of the domain can also account for differences in deposition fractions. Studies by Xi *et al* [30], Zhang *et al* [33], and Zhang *et al* [23] included the larynx and the studies by Xi *et al* and Luo *et al* [70] used CT scan based geometry. The presence of a jet can alter fluid flow and particle deposition in the airways as well as differences in flow rates [30, 70, 83].

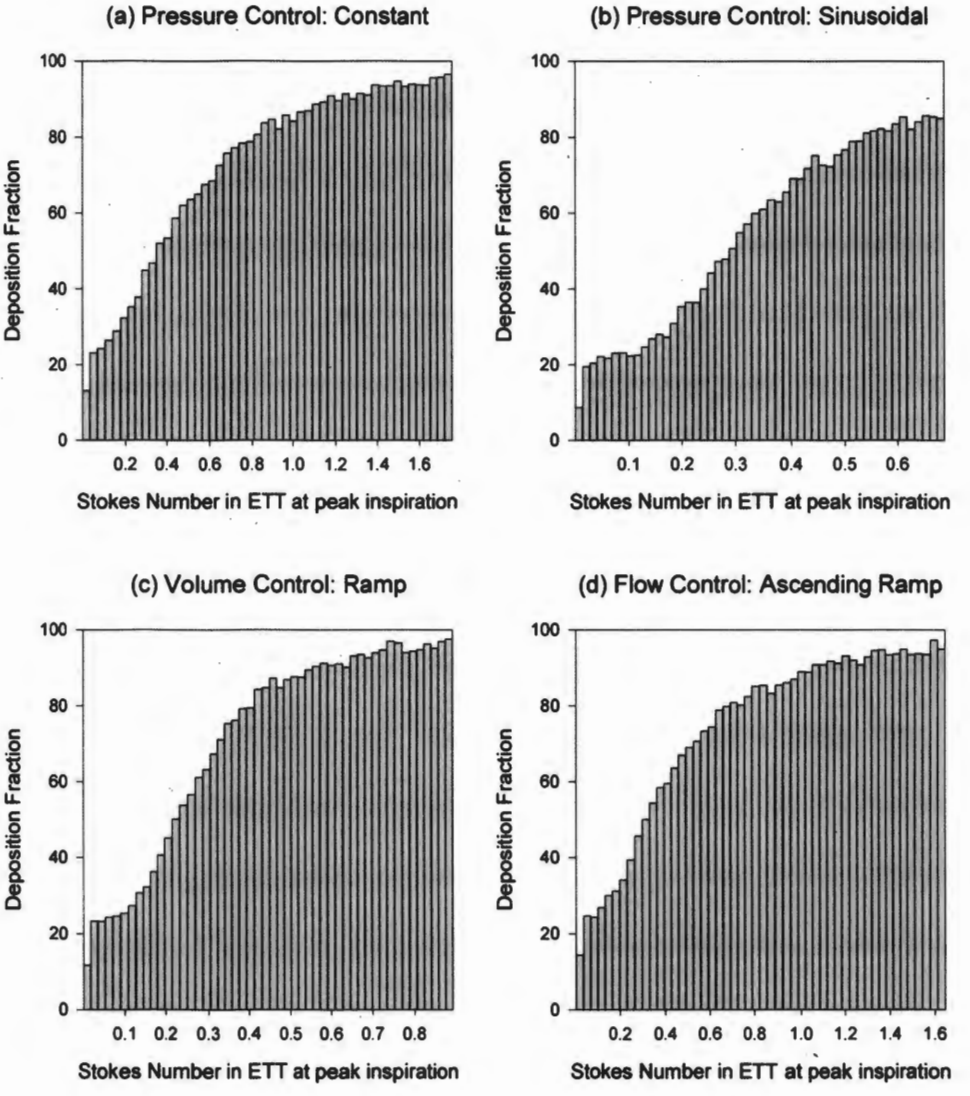

Figure 4.19: Deposition fraction histograms. Colored by Stokes number in the ETT at peak inspiration. Each histogram has 50 bins.

Deposition fractions presented in Figure 4.19 at lower diameters agree well with the study performed by Luo *et al* [70] when compared to the pressure controlled sinusoidal waveform with similar peak inspiratory flow rate. The deposition fractions in this study are about three times higher than those reported by Luo *et al* [70] for other particle diameters. This is likely due to the presence of the ETT jet increasing the role of

impaction. Even when the laryngeal jet is included, as in the study by Zhang *et al* [23], higher deposition fractions (~ 3 times higher) are seen in the current study. This is likely due to the closer proximity of the ETT jet to the carina of the first bifurcation and the absence of the oral airways filtering out a large percentage of the particles due to strong upstream deposition [23]. In general deposition fractions in the current study are higher than those reported in previous literature which is hypothesized to be caused by the unique characteristics of the ETT jet as well as geometric differences.

Deposition at the lowest particle diameters was similar between the different waveforms as observed in Figure 4.20 (a). The pressure controlled constant and the flow controlled ascending ramp waveforms showed very similar deposition fractions over the chosen diameter range (0.05-10 μm). The slightly higher deposition for the flow controlled ascending ramp case for particles between about 4.0-8.5 μm in diameter can be attributed to the higher population of particles just before reaching peak inspiratory flow as was observed in Figure 4.18. This difference would have been more pronounced had the population of particles been lower just before peak expiration in the pressure controlled constant case or had there been less of a difference in deposition rates between inspiration and expiration. The pressure controlled sinusoidal waveform showed a lower deposition fraction over the particle diameter range due to the decreased role of impaction, turbulent dispersion, and turbophoresis. The volume controlled ramp waveform had a lower deposition fraction than the pressure controlled constant and the flow controlled ascending waveforms for particles between 2-6 μm. Because of the consistent flow rate in the volume controlled ramp case, larger particles never had a period of time when they could pass the particle deposition hot spots, due to a very low

flow rate. This is different than the pressure controlled constant and flow controlled ascending ramp cases where higher flow rates existed, but there were also long periods of very low flow rate that lowered the deposition fraction for particles larger than about 3 μm in diameter.

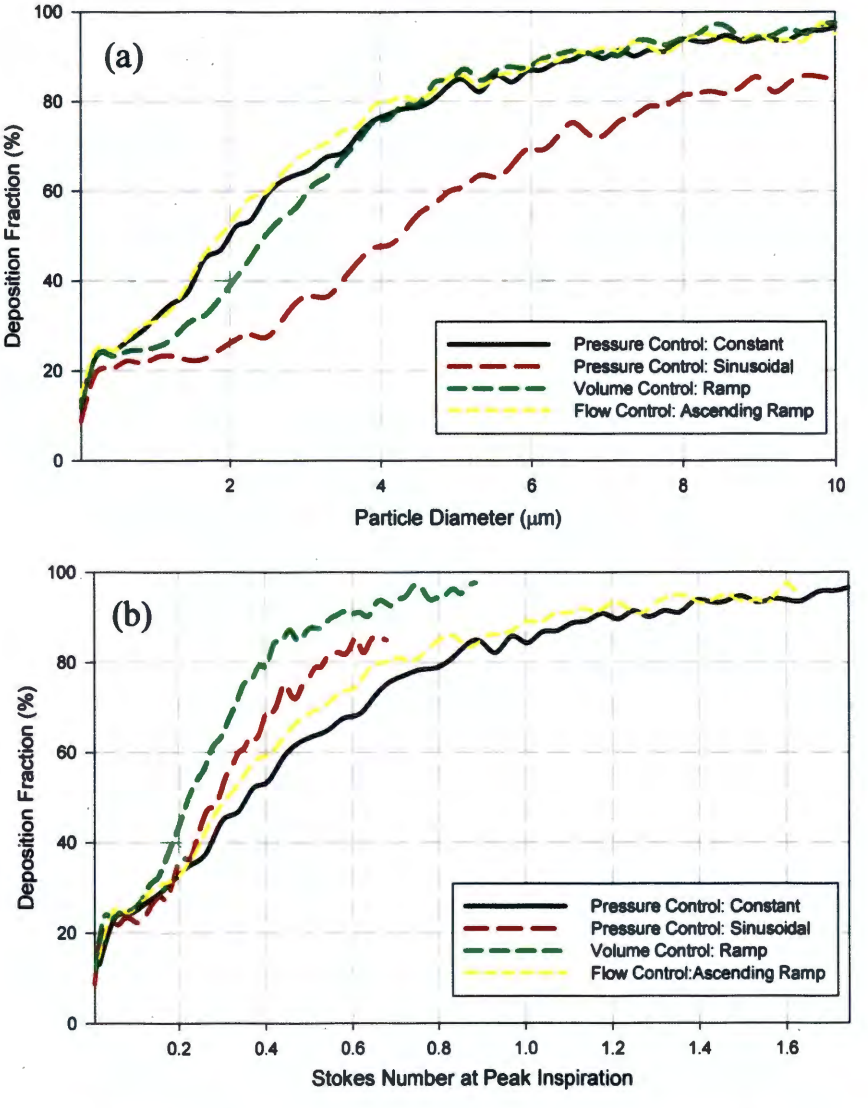

Figure 4.20: Deposition fraction (a) by particle diameter and (b) by Stokes number in the ETT at peak inspiration

4.6.3. Local Deposition. Local deposition is characterized qualitatively by identifying particle deposition locations, and quantitatively by contours of deposition enhancement factor (DEF). Particle locations for the pressure controlled sinusoidal waveform are shown in Figure 4.21. Similar particle deposition plots have been reported in the literature [26, 30-31, 70, 87, 126]. All of these studies used a steady state inlet condition, and only the study performed by Lambert *et al* [31] accounted for the unsteadiness of turbulence. Particle deposition in realistic and simplified models of the oral airways was studied by Xi *et al* [26]. Lambert *et al* [31], Luo *et al* [70], and Xi *et al* [30] studied particle deposition in CT scan based models of the upper tracheobronchial region. Particle deposition in geometrically simplified airways was studied by Luo *et al* [70] and Li *et al* [87]. Lambert *et al* [31], Xi *et al* [26], and Xi *et al* [30] included the larynx.

Several deposition hot spots are visible in Figure 4.21: the site where the ETT jet impinges and deflects off of the wall of the right main bronchus, the site where the deflected jet impinges on the wall of the right main bronchus, the walls surrounding the large rotating structure in the right main bronchus, the superior wall of the branch leading to the right upper lobe, the superior wall of the left main bronchus near the first bifurcation, and the carinas of the bifurcations.

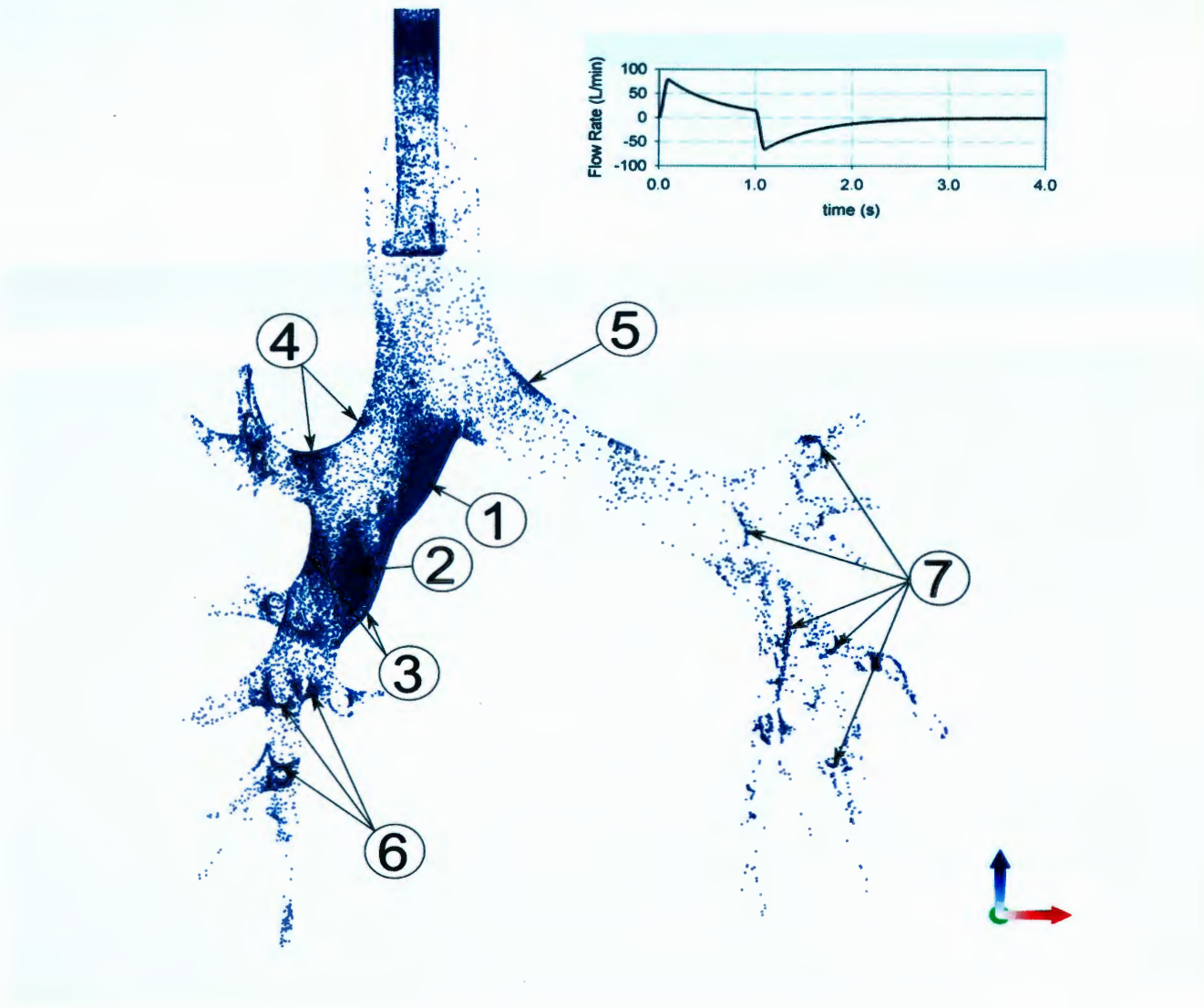

Figure 4.21: Deposition locations for the pressure controlled sinusoidal waveform. Key deposition hot spots are labeled as: (1) Site of impingement and the site where the ETT jet impinges and deflects off of the wall of the right main bronchus, (2) the site where the deflected jet impinges on the wall of the right main bronchus, (3) the walls surrounding the large rotating structure in the right main bronchus, (4) the superior wall of the branch leading to the right upper lobe, (5) the superior wall of the left main bronchi near the first bifurcation, (6) the carinas of the right lung e.g. (7) and the carinas of the left lung e.g.

The deposition at the impingement sites of the ETT jet is caused by impaction similar to the impaction reported by Xi *et al* [26] with a difference being that the

impaction sites are in the right main bronchi. The deposition caused by the large rotating structure is not as concentrated as the deposition at the impingement site; however this is clearly an area of enhanced deposition caused by turbulent dispersion and turbophoresis similar to the enhanced deposition around the recirculation zone reported by Xi *et al* [30] in the trachea. The deposition on superior wall of the branch leading to the right upper lobe and the superior wall of the left main bronchi near the first bifurcation are caused by impaction as the flow from the right main bronchi changes direction rapidly while it is redirected into the left main bronchi. This phenomenon is unique to this study and has not been reported previously. Enhanced particle deposition at the carinas is an established result of inertial impaction and has been reported in several prior studies [30-31, 70, 87, 126].

The CT scan based studies showed much less deposition in the right main bronchus and a much greater deposition on the ventral side of the left main bronchus than the current study [30-31, 70]. In the current study there was a much greater deposition in the right main bronchus compared to the CT scan based studies of the upper tracheobronchial region due to the impaction caused by the ETT jet and the large rotating structure in the right main bronchus along with the increased turbulence [30-31, 70]. The deposition is much greater on the superior side and much less on the inferior side of the left main bronchus than in the CT scan based studies of the upper tracheobronchial region because of the way the air enters the left main bronchus as described in § 4.5.1 [30-31, 70]. Particle deposition locations colored by Stokes number in the ETT at peak inspiration are presented in Figure 4.22 for each waveform.

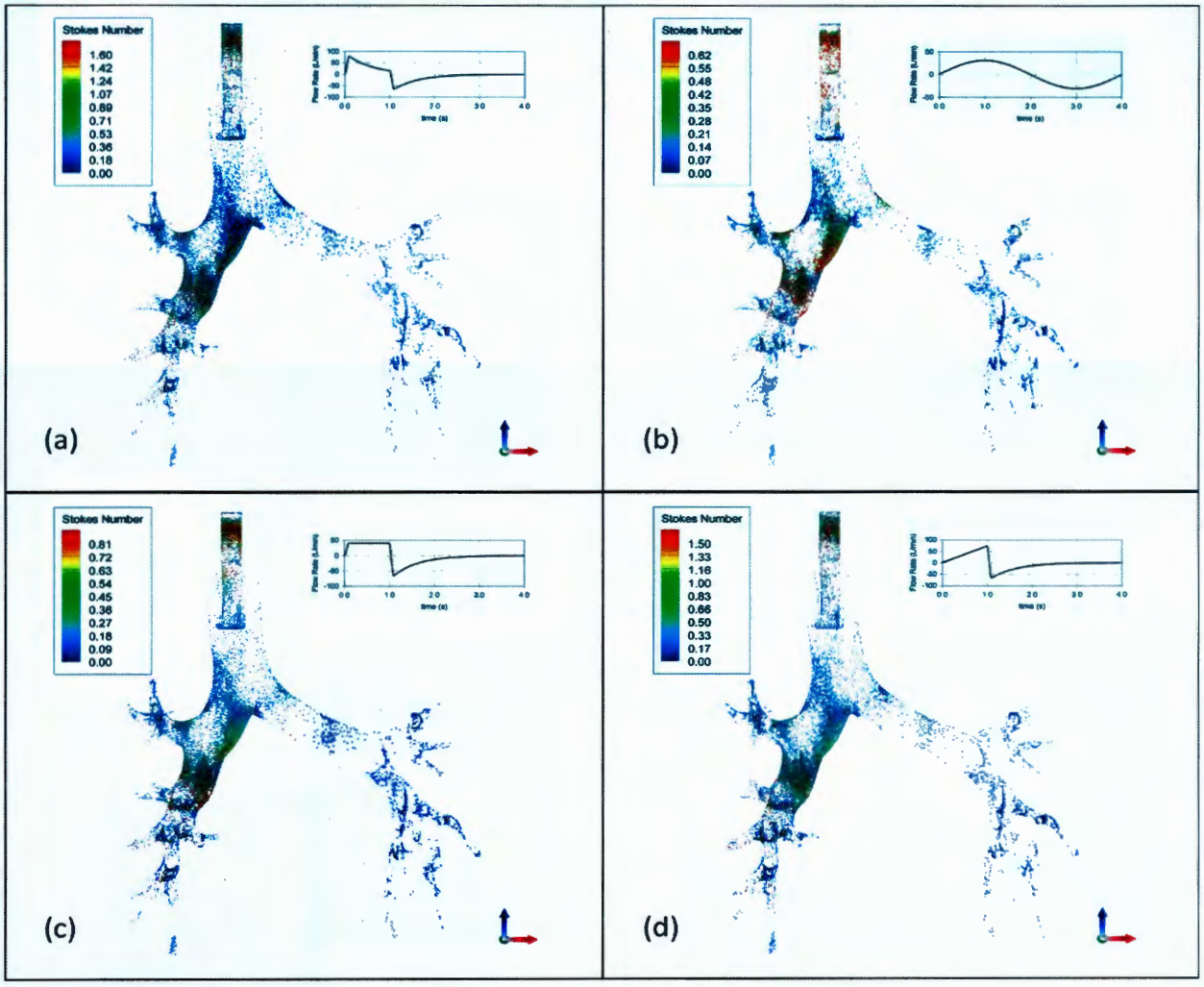

Figure 4.22: Deposition locations by Stokes number. Particles are colored by stokes number in the ETT at peak inspiration. (a) pressure controlled constant, (b) pressure controlled sinusoidal, (c) volume controlled ramp, and (d) flow controlled ascending ramp.

For the pressure controlled sinusoidal case (Figure 4.22 b) only particles at a high Stokes number range deposited at sites 1-5 (Figure 4.21) and most of the larger particles are filtered out before traveling through the left main bronchus. The pressure controlled constant and flow controlled ascending ramp cases (Figure 4.22 a and d) show a much greater range of particles deposited at sites 1-5, and most of the higher diameter particles

are filtered out before reaching site 5. The volume controlled ramp waveform (Figure 4.22 c) shows a larger range of particle sizes deposited at sites 1-5 than the pressure controlled sinusoidal waveform but a smaller range of particle sizes deposited at sites 1-5 than the pressure controlled constant or flow controlled ascending ramp waveforms. These results suggest that a higher peak inspiratory flow rate will cause particles to deposit at a shorter downstream distance and that this effect is more pronounced for larger particles.

Particle deposition locations colored by the time of deposition are presented in Figure 4.23 for each waveform. In general, particles did not deposit in the lower airways until later times and particles deposited in the left lung at a later times than the right lung because the flow would direct particles through the right lung before reaching the left lung. The particles deposited most heavily at times near the time of peak inspiration because of the influence of impaction, turbulent dispersion, and turbophoresis. The time of peak inspiration for the pressure controlled constant and flow controlled ascending ramp waveforms were sharp and occurred at 0.1 s and 1.0 s respectively and the corresponding colors for these times are clearly dominant in Figure 4.23 (a) and (d). The peak inspiration for the pressure controlled sinusoidal waveform is smoother and occurred at 1.0 s so a wider range of colors can be seen in Figure 4.23 (b) but they are still centered around the colors corresponding to 1.0 s. The volume controlled ramp waveform was at peak inspiration between 0.1 and 1.0 s so a very wide range of colors are seen in Figure 4.23 (c).

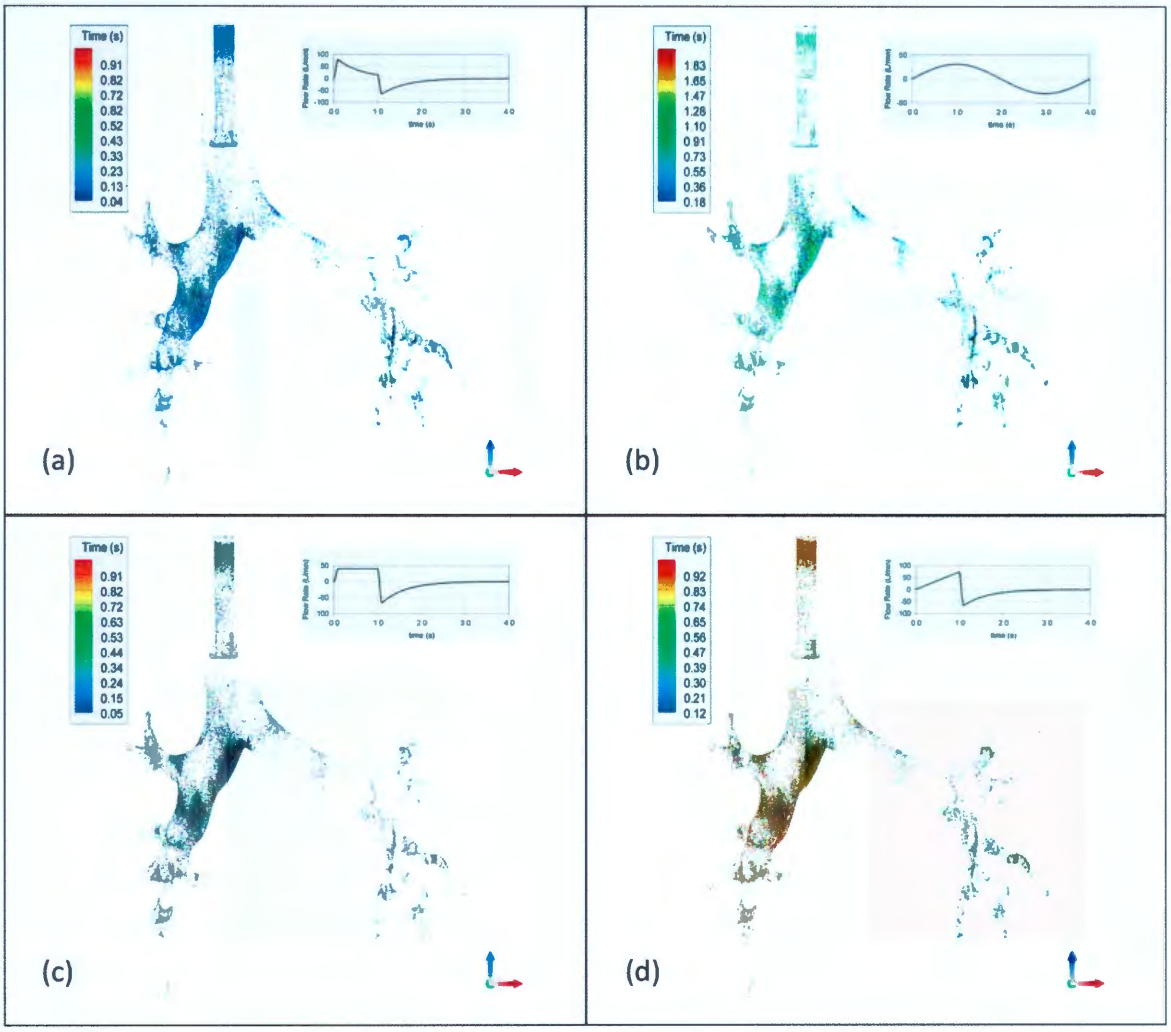

Figure 4.23: Deposition locations by time. Particles are colored by time of deposition. (a) pressure controlled constant, (b) pressure controlled sinusoidal, (c) volume controlled ramp, and (d) flow controlled ascending ramp.

The most commonly used parameter for characterizing local deposition is the deposition enhancement factor (DEF) defined by [67]:

$$DEF = \frac{N_i / A_i}{\sum_{j=1}^{m} N_j / \sum_{j=1}^{m} A_j} \tag{4.7}$$

where N_i is the number of particles deposited on face i, A_i is the area of face i, and m is the total number of faces. Balshazy *et al* [67] have shown that DEF is highly dependent upon patch size used and that a larger patch size will result in a lower maximum DEF. In the current study the surface mesh was used to facilitate the calculation of DEF. A patch was taken to be all of the faces adjacent to a single node and the patches were allowed to overlap as needed. The average area of a patch used was 1.00 mm^2 and the standard deviation of the patch area was 0.57 mm^2. The values of DEF were calculated for each node on the surface.

Contours of DEF have been reported by studies in the past [23, 27, 30, 101, 127]. All of these studies were performed with a steady inlet condition. The studies performed by Shi *et al* [127], Zhang *et al* [101], and Zhang *et al* [27] were focused on nano-scale particles and the study by Zhang *et al* [27] was performed in a simplified model of the oral airways. Only the studies by Xi *et al* [30] and Zhang *et al* [23] included a jet structure and the first few bifurcations and the study by Xi *et al* [30] was the only study with geometry based on CT scans.

The contours of DEF are displayed in Figure 4.24 as viewed from the front. In general the deposition enhancement factors reported by Xi *et al* [30] are larger than those found in the current study. This result is expected because of the difference in patch size (~0.2 mm^2 compared to 1.0 mm^2) however this also may be caused by differences in particle size, or geometry. In previous studies the carinas were areas where there was significant particle deposition [23, 30, 101, 127]. In the current study there was similar deposition enhancement factors seen at the carinas, however there were also large deposition enhancement factors at sites 1-4 (refer to Figure 4.21). The large deposition

enhancement factor at site 1 is caused by impaction at the site of the ETT jet impingement and can be seen in Figure 4.24 for all waveforms.

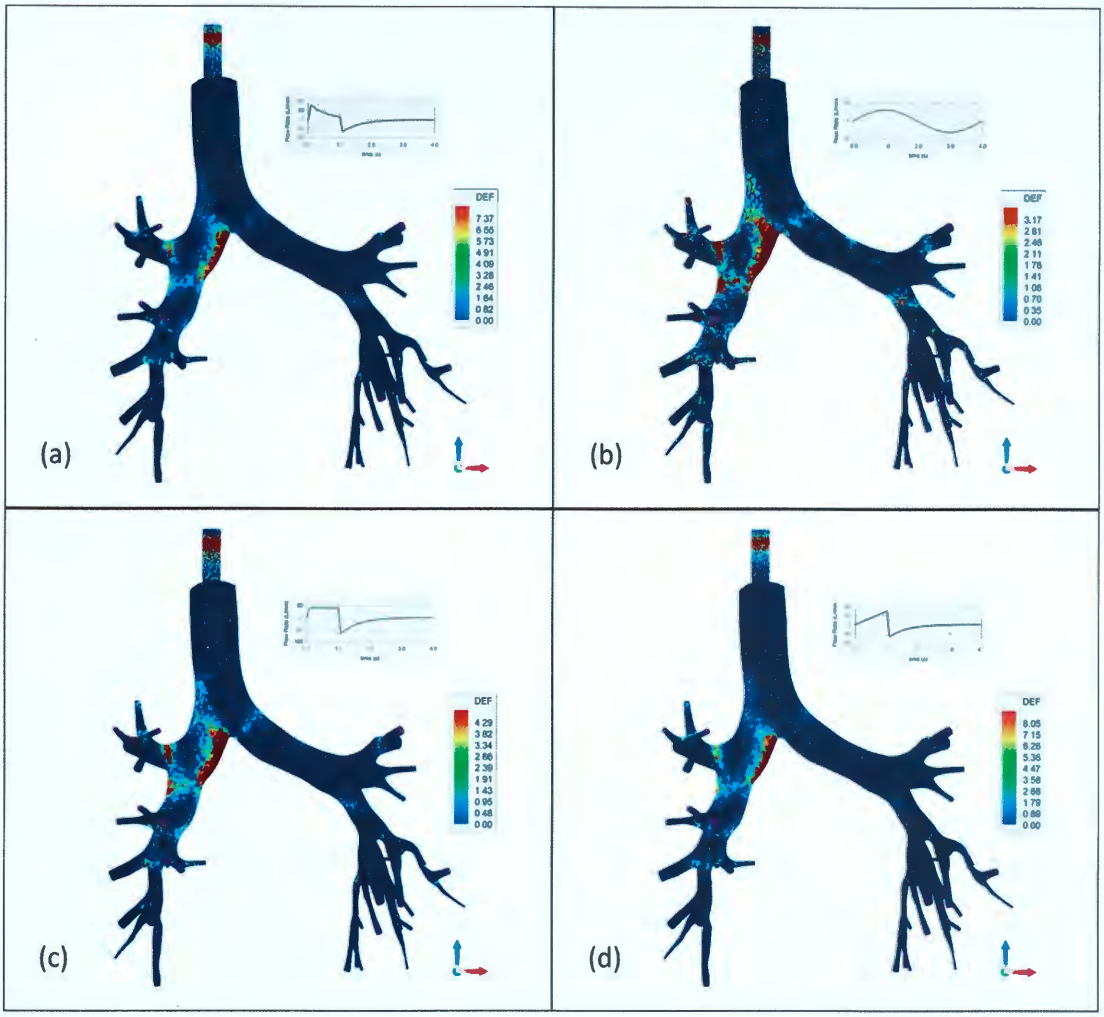

Figure 4.24: Contours of DEF (front view)

The large deposition enhancement factor for sites 2-4 are best seen in Figure 4.25 where the contours of DEF are shown from the back of the lung and focused on the right lung. A view of the contours of DEF from the front, with a focus on the left lung, is

shown in Figure 4.26. DEFs at the carinas of the right and left lungs are best seen in Figure 4.25 and Figure 4.26 respectively. Site 5 showed a large number of deposited particles however they were scattered so evenly over such a large area that an elevated deposition enhancement factor is not clearly visible. In general higher values of DEF are present in the right lung compared to the left lung due to the increased deposition.

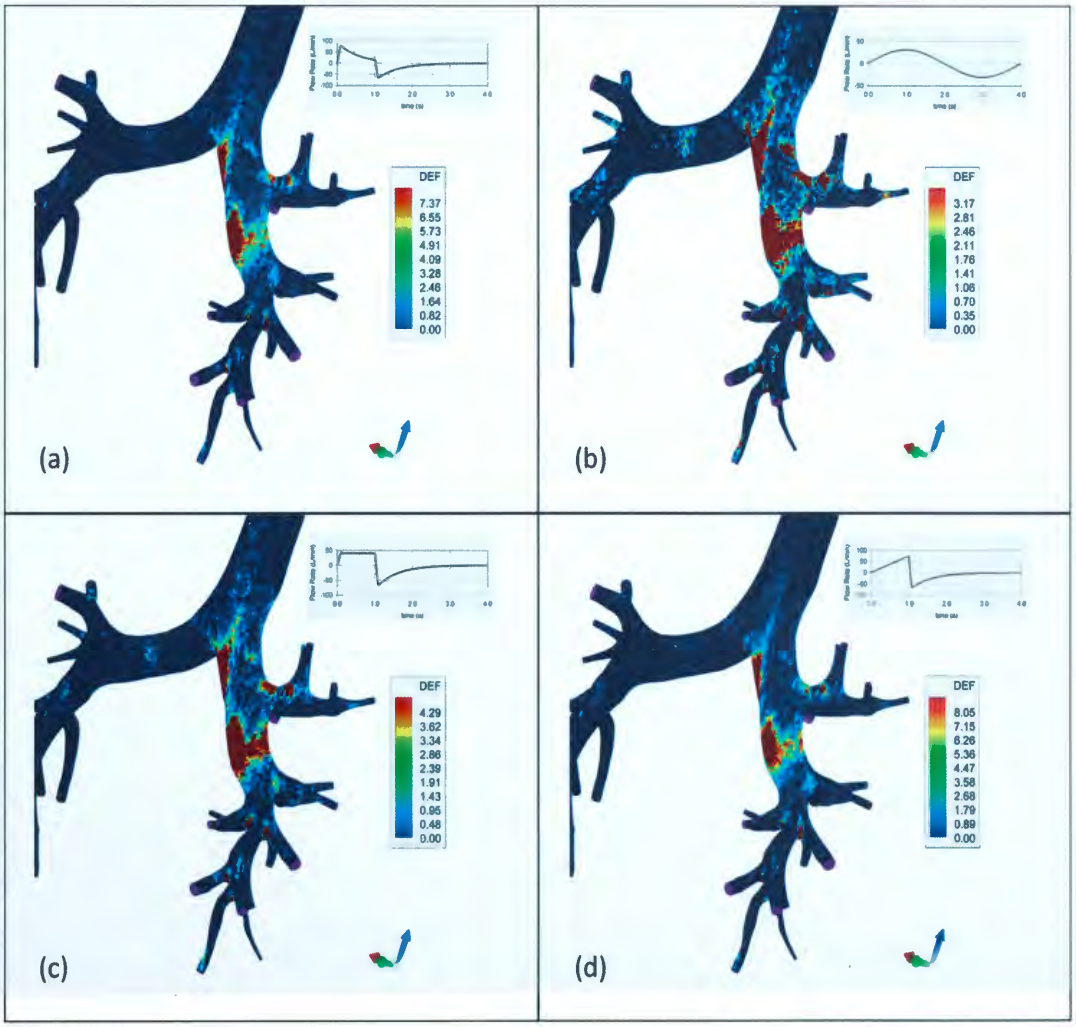

Figure 4.25: Contours of DEF (back right view)

The differences in DEF between the key deposition sites are more pronounced for the pressure controlled constant and flow controlled ascending ramp waveforms than the pressure controlled sinusoidal or volume controlled ascending ramp waveforms. This occurs because, at higher flow rates, there are more particles depositing at the lower numbered sites and this leaves a smaller number of particles left to deposit at the higher number sites. At lower flow rates the selection of particles reaching the different deposition sites are more similar.

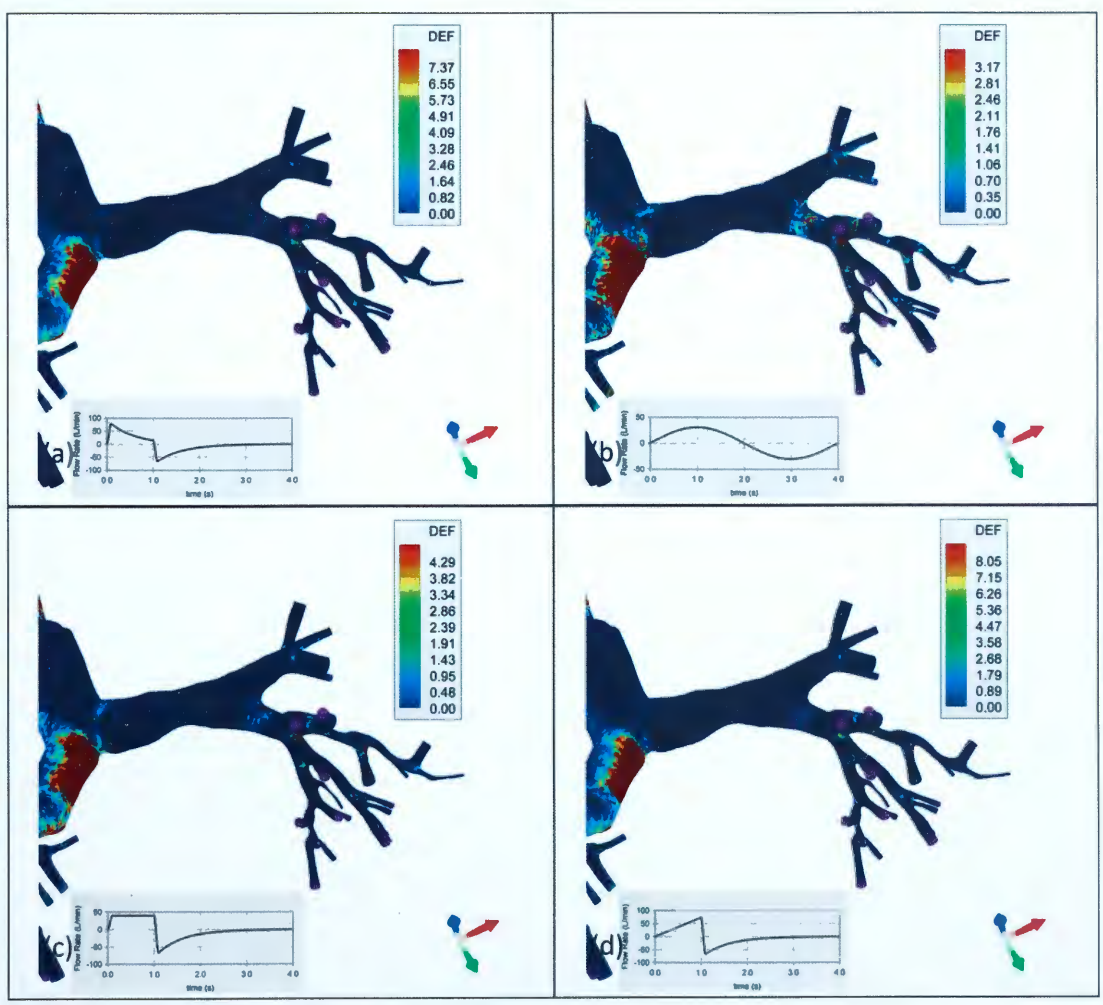

Figure 4.26: Contours of DEF (front left view)

The maximum deposition enhancement factor for each waveform is presented in Table 4.6. These values are generally lower than those presented in the study by Xi *et al* [30], however this result is again expected because of the difference in patch size however this also may be caused by differences in particle size, or geometry. In general, there are much greater differences in the maximum DEFs between the waveforms than the overall deposition fractions (Table 4.5). For example the percent difference between the overall deposition fraction for the volume controlled ramp and flow controlled ascending ramp waveforms is 6.20 % while the percent difference between the maximum DEFs is 60.82 %. This suggests that while the overall particle deposition is similar for the two waveforms, the particle deposition locations are much more concentrated for the flow control ascending ramp waveform than for the volume controlled ramp waveform. This could have significance for deposited drug aerosols that may have negative side effects in large concentrations. When the pressure controlled sinusoidal case and the volume controlled ramp case are compared, the percent difference between the overall deposition fractions is 29.81 % and the percent difference between the maximum deposition enhancement factor is 30.22 % which indicates that the difference in particle deposition concentrations results more from the number of particles depositing rather than the sites where the particles are depositing.

Table 4.6: Maximum deposition enhancement factor

Waveform	Maximum DEF
Pressure Controlled: Constant	270.2
Pressure Controlled: Sinusoidal	116.1
Volume Controlled: Ramp	157.5
Flow Controlled: Ascending Ramp	295.1

5. CONCLUSIONS AND FUTURE WORK

In this study, a computational domain was reconstructed from CT scans of a 57 year old male patient undergoing mechanical ventilation treatment. A numerical model was selected with appropriate boundary conditions and turbulence modeling using LES to simulate fluid flow with a transient inlet boundary condition. Studies were performed to ensure spatial and temporal convergence and simulations were run to validate the numerical model with comparison to experimental data of Lieber and Zhao [117]. Computational fluid dynamics along with a user defined particle force subroutine were applied to evaluate fluid flow and particle deposition characteristics for flow in the upper tracheobronchial region for a range of inspiratory waveforms typically seen in patients undergoing mechanical ventilation treatment.

5.1. CONCLUSIONS

From the evaluation of the fluid flow it was clear that the jet caused by the endotracheal tube was an important fluid flow feature with effects similar to that of the laryngeal jet. These effects include: high flow rates in the trachea, the creation of a zone of recirculation, the initiation of turbulence, and the impaction of particles at the site of the jet's impingement. The full range of effects of the jet caused by the endotracheal tube is not fully understood and requires further study. The presence and strength of the recirculation zone in the right main bronchus and the swirling flows in the bronchi were found to be dependent upon the flow history as well as the inspiratory flow rate. This implies that these transient fluid flow events may not be captured with steady state analyses. Strong turbulence was found in the wake of the jet caused by the flow from the

endotracheal tube which dissipated in the lower airways of the domain as indicated by vorticity magnitude and turbulence kinetic energy.

From the evaluation of particle deposition within the tracheobronchial model, it was found that particle impaction was linked to inspiratory flow rate with the rate of particle deposition generally following the inspiratory flow rate. The lowest value of overall deposition fraction was found in the pressure controlled sinusoidal waveform, followed by the volume controlled ramp, pressure controlled constant, and flow controlled ascending ramp with the highest overall deposition fraction. This does not create implications on particle deposition in the lower airways that were not included in the domain.

Upon evaluation of the local deposition, several key deposition locations were identified including: the site of impingement and deflection of the jet caused by the endotracheal tube on the wall of the right main bronchus, the site where the deflected jet impinges on the wall of the right main bronchus, the walls surrounding the large rotating structure in the right main bronchus, the superior wall of the branch leading to the right upper lobe, the superior wall of the left main bronchi near the first bifurcation, and the carinas of the airway bifurcations. The size of the particles depositing at the key deposition locations is linked with peak inspiratory flow rate due to the effects of particle impaction, turbulent dispersion and turbophoresis. The time at which particles deposit is also typically matched with the time of peak inspiratory flow. Finally the differences in the deposition enhancement factors and the overall deposition fractions give evidence of drug aerosol concentrations in key deposition sites which may be significant for drugs with negative side effects in high concentrations.

5.2. FUTURE WORK

For numerical studies to be clinically applicable, a degree of realism must be represented by the complete numerical model including the geometry, boundary conditions, and treatment of turbulence [13]. The current work studies fluid flow and particle deposition in a reconstructed model for a single intubated patient with a proportional mass flow rate outlet condition. Future work on fluid flow and particle transport in the human respiratory system may include the following:

• **Detailed study of the endotracheal tube**: The results of this study combined with the lack of detailed work on the endotracheal tube, show a need for studies to investigate the effects of endotracheal tube characteristics on fluid flow and particle deposition. A study performed by Esteban *et al* [37] reports that 99 % of the patients studied undergoing mechanical ventilation in America were ventilated through intubation or a tracheostomy. This indicates that a better understanding of the effects of the endotracheal tube is critical for clinical applications. Studies will be performed to investigate the effects of endotracheal tube size and position on fluid flow and particle deposition for patients undergoing mechanical ventilation treatment.

• **Improving the outlet condition**: An outlet condition based on a proportional mass flow rate has been applied by studies in the past; however an alternate outlet condition may be more physiologically realistic [30, 70, 115-116, 128]. Results that are more physiologically realistic may be achieved with a boundary condition that models the outlets as balloons with flow resistance. The pressure at each outlet could be specified based on the volume of flow that has passed through the outlet and the instantaneous flow rate combined with data of airway compliance and resistance.

• **Patient specific studies**: The use of geometry based on the CT scans of patients helps to ensure a realistic geometry and is an important step towards clinical usefulness [13]. However conclusions drawn from the results of simulations in the airways of a single patient may not be representative of the airways of every patient. In order to provide useful insight into fluid flow and aerosol drug delivery for clinicians it is important to consider patient specific geometry and boundary conditions [128]. Further study is necessary to determine what patient to patient differences will significantly impact drug aerosol delivery. In addition further techniques must be developed to measure and account for these significant patient to patient differences.

• **Experimental work**: CFD has proven useful in evaluating fluid flow and particle deposition in simplified numerical models of the human airways. To make these CFD studies more useful for real world applications the complexity of the numerical models must grow. With the growth of complexity of numerical models it becomes increasingly important to validate these numerical methods with experimental results. Experiments will be carried out to further validate the numerical methods used in the present and future works.

APPENDIX A.

VALIDATION AND CONVERGENCE STUDY GEOMETRY CREATION CODE

```
function []=geometry()
al=35;
be=18;
D=3.81;
d=D/sqrt(2);
L=2.5*D;
R=7*d;

a1=(8*d*cosd(be)-(L-d*sind(be))*tand(be)-4*D)/(6*(L-
d*sind(be))^2);
b1=((L-d*sind(be))*tand(be)-2*d*cosd(be)+D)/(6*(L-
d*sind(be))^8);

la=tand(be)*(L-d*sind(be))/(d*cosd(be));
a=0.5*d*cosd(be)/(0.5*L-0.5*d*sind(be))^la;

Ax=L-(R+0.5*d)*sind(be);
Mx=0;
Nx=0;
Cx=L;
Gx=L/2;
Ex=Cx-d*sind(be);
Kx=Cx-d/2*sind(be);
Px=Kx;
Jx=Kx+2*R*sind(0.5*(al-be))*cosd(be+0.5*(al-be));
Fx=Jx-0.5*d*sind(al);
Hx=Jx+0.5*d*sind(al);


dx=0.01;
dt=0.1;
%line ME
xme=(Mx:dx:Ex)';
yme=a1*xme.^2+b1*xme.^8+0.5*D;
zme=zeros(size(xme));
%line EF
xef=(Ex:dx:Fx)';
yef=(R+0.5*d)*cosd(be)-((R-0.5*d)^2-(xef-
L+(R+0.5*d)*sind(be)).^2).^(1/2);
zef=zeros(size(xef));
%line GK
xgk=(Gx:dx:Kx)';
ygk=a*(xgk-0.5*L).^la;
zgk=zeros(size(xgk));
%line KJ
xkj=(Kx:dx:Jx)';
```

```
ykj=(R+0.5*d)*cosd(be)-(R^2-(xkj-
L+(R+0.5*d)*sind(be)).^2).^(1/2);
zkj=zeros(size(xkj));
%line CH
xch=(Cx:dx:Hx)';
ych=(R+0.5*d)*cosd(be)-((R+0.5*d)^2-(xch-
L+(R+0.5*d)*sind(be)).^2).^(1/2);
zch=zeros(size(xch));
%line NP
xng=(Nx:dx:Gx)';
xnp=[xng;xgk];
ynp=[zeros(size(xng));ygk];
znp=0.5*(d-D)*xnp/(L-0.5*d*sind(be))+0.5*D;

plot3(xme,yme,zme,'.','Color',[rand(1) rand(1) rand(1)]);
hold on
plot3(xef,yef,zef,'.','Color',[rand(1) rand(1) rand(1)]);
plot3(xgk,ygk,zgk,'.','Color',[rand(1) rand(1) rand(1)]);
plot3(xkj,ykj,zkj,'.','Color',[rand(1) rand(1) rand(1)]);
plot3(xch,ych,zch,'.','Color',[rand(1) rand(1) rand(1)]);
plot3(xnp,ynp,znp,'.','Color',[rand(1) rand(1) rand(1)]);
xlim([-15,15]);
ylim([-15,15]);
zlim([-15,15]);


plot3(xme,-yme,zme,'.','Color',[rand(1) rand(1) rand(1)]);
plot3(xef,-yef,zef,'.','Color',[rand(1) rand(1) rand(1)]);
plot3(xgk,-ygk,zgk,'.','Color',[rand(1) rand(1) rand(1)]);
plot3(xkj,-ykj,zkj,'.','Color',[rand(1) rand(1) rand(1)]);
plot3(xch,-ych,zch,'.','Color',[rand(1) rand(1) rand(1)]);
plot3(xnp,ynp,-znp,'.','Color',[rand(1) rand(1) rand(1)]);
plot3(xnp,-ynp,-znp,'.','Color',[rand(1) rand(1) rand(1)]);
plot3(xnp,-ynp,znp,'.','Color',[rand(1) rand(1) rand(1)]);
hold off

figure;
plot(xme,yme,'.','Color',[rand(1) rand(1) rand(1)]);
hold on
plot(xef,yef,'.','Color',[rand(1) rand(1) rand(1)]);
plot(xgk,ygk,'.','Color',[rand(1) rand(1) rand(1)]);
plot(xkj,ykj,'.','Color',[rand(1) rand(1) rand(1)]);
plot(xch,ych,'.','Color',[rand(1) rand(1) rand(1)]);
xlim([0,15]);
ylim([0,15]);
hold off
```

```
xmef=[xme;xef];
ymef=[yme;yef];
zmef=[zme;zef];
file=fopen('curveMEF.txt','wt');
for i=1:length(xmef)
    fprintf(file,'%1.8f %1.8f
%1.8f\n',xmef(i),ymef(i),zmef(i));
end
fclose(file);

xgkj=[xgk;xkj];
ygkj=[ygk;ykj];
zgkj=[zgk;zkj];
file=fopen('curveGKJ.txt','wt');
for i=1:length(xgkj)
    fprintf(file,'%1.8f %1.8f
%1.8f\n',xgkj(i),ygkj(i),zgkj(i));
end
fclose(file);

file=fopen('curveCH.txt','wt');
for i=1:length(xch)
    fprintf(file,'%1.8f %1.8f
%1.8f\n',xch(i),ych(i),zch(i));
end
fclose(file);

xnpkj=[xnp;xkj];
ynpkj=[ynp;ykj];
znpkj=[znp;zkj+d/2];
file=fopen('curveNPKJ1.txt','wt');
for i=1:length(xnpkj)
    fprintf(file,'%1.8f %1.8f
%1.8f\n',xnpkj(i),ynpkj(i),znpkj(i));
end
fclose(file);

xnpkj=[xnp;xkj];
ynpkj=[-ynp;-ykj];
znpkj=[znp;zkj+d/2];
file=fopen('curveNPKJ2.txt','wt');
for i=1:length(xnpkj)
    fprintf(file,'%1.8f %1.8f
%1.8f\n',xnpkj(i),ynpkj(i),znpkj(i));
end
fclose(file);
```

```
xnpkj=[xnp;xkj];
ynpkj=[ynp;ykj];
znpkj=[-znp;-(zkj+d/2)];
file=fopen('curveNPKJ3.txt','wt');
for i=1:length(xnpkj)
    fprintf(file,'%1.8f %1.8f
%1.8f\n',xnpkj(i),ynpkj(i),znpkj(i));
end
fclose(file);

xnpkj=[xnp;xkj];
ynpkj=[-ynp;-ykj];
znpkj=[-znp;-(zkj+d/2)];
file=fopen('curveNPKJ4.txt','wt');
for i=1:length(xnpkj)
    fprintf(file,'%1.8f %1.8f
%1.8f\n',xnpkj(i),ynpkj(i),znpkj(i));
end
fclose(file);

function []=pr(xl,dx,th,yl,wh)
al=35;
be=18;
D=3.81;
d=D/sqrt(2);
L=2.5*D;
R=7*d;
a1=(8*d*cosd(be)-(L-d*sind(be))*tand(be)-4*D)/(6*(L-
d*sind(be))^2);
b1=((L-d*sind(be))*tand(be)-2*d*cosd(be)+D)/(6*(L-
d*sind(be))^8);
la=tand(be)*(L-d*sind(be))/(d*cosd(be));
a=0.5*d*cosd(be)/(0.5*L-0.5*d*sind(be))^la;
ps1=(xl(1):dx:xl(2))';
ps2=(xl(1):dx:xl(2))';
y=L/2*tand(be)-ps1.*cosd(th)-a1.*(L/2+ps1.*sind(th)).^2-
b1.*(L/2+ps1.*sind(th)).^8-0.5*D;
%w=- cosd(th) - 2*a1*sind(th)*(L/2 + ps1*sind(th)) -
8*b1*sind(th)*(L/2 + ps1*sind(th)).^7;
z=L/2*tand(be)-ps2.*cosd(th)-a.*(ps2.*sind(th)).^(la);
w=- cosd(th) - a*la*sind(th)*(ps2*sind(th)).^(la - 1);
if(wh==0)
    plot(ps1,z);
elseif(wh==1)
    plot(ps1,w);
elseif(wh==2)
```

```
    plot(ps1,z,ps1,w);
end
if(yl)
    ylim([-.1,.1]);
end

function [y]=ps1eq(th,ps1)
be=18;
D=3.81;
d=D/sqrt(2);
L=2.5*D;
a1=(8*d*cosd(be)-(L-d*sind(be))*tand(be)-4*D)/(6*(L-
d*sind(be))^2);
b1=((L-d*sind(be))*tand(be)-2*d*cosd(be)+D)/(6*(L-
d*sind(be))^8);
y=L/2*tand(be)-ps1.*cosd(th)-a1.*(L/2+ps1.*sind(th)).^2-
b1.*(L/2+ps1.*sind(th)).^8-0.5*D;

function [y]=ps2eq(th,ps2)
be=18;
D=3.81;
d=D/sqrt(2);
L=2.5*D;
la=tand(be)*(L-d*sind(be))/(d*cosd(be));
a=0.5*d*cosd(be)/(0.5*L-0.5*d*sind(be))^la;
y=L/2*tand(be)-ps2.*cosd(th)-a.*(ps2.*sind(th)).^(la);
```

APPENDIX B.

WOMERSLEY VELOCIY PROFILE SUBROUTINE

```
#include "cfx5ext.h"
dllexport(wom)
      SUBROUTINE WOM (
     &  NLOC, NRET, NARG, RET, ARGS, CRESLT, CZ,DZ,IZ,LZ,RZ
)
      IMPLICIT NONE
CD User routine: template for user CEL function
CC
CC --------------------
CC        Input
CC --------------------
CC
CC  NLOC   - size of current locale
CC  NRET   - number of components in result
CC  NARG   - number of arguments in call
CC  ARGS() - (NLOC,NARG) argument values
CC
CC --------------------
CC      Modified
CC --------------------
CC
CC  Stacks possibly.
CC
CC --------------------
CC        Output
CC --------------------
CC
CC  RET()  - (NLOC,NRET) return values
CC  CRESLT - 'GOOD' for success
CC
CC --------------------
CC       Details
CC --------------------
CC
CC============================================================
=============
C
C -----------------------------
C     Preprocessor includes
C -----------------------------
C
#include "parallel_partitioning.h"
C
C -----------------------------
C        Global Parameters
C -----------------------------
C
```

```
C
C -----------------------------
C       Argument list
C -----------------------------
C
      INTEGER NLOC,NARG,NRET
C
      CHARACTER CRESLT*(*)
C
      REAL ARGS(NLOC,NARG), RET(NLOC,NRET)
C
      INTEGER IZ(*)
      CHARACTER CZ(*)*(1)
      DOUBLE PRECISION DZ(*)
      LOGICAL LZ(*)
      REAL RZ(*)
C
C -----------------------------
C       External routines
C -----------------------------
C
C
C -----------------------------
C       Local Parameters
C -----------------------------
      COMPLEX I
      PARAMETER(I=(0,1))
C -----------------------------
C       Local Variables
C -----------------------------
C
      INTEGER ILOC
      REAL AL(1:NLOC,1), R(1:NLOC,1), T(1:NLOC,1),
     &  A(1:NLOC,1), W(1:NLOC,1), P(1:NLOC,1)
      COMPLEX B, C
C
C -----------------------------
C       Stack pointers
C -----------------------------
C
C============================================================
============
C
C --------------------------
C    Executable Statements
C --------------------------
C
```

```
      R(1:NLOC,1) = ARGS(1:NLOC,1)
      T(1:NLOC,1) = ARGS(1:NLOC,2)
      A(1:NLOC,1) = ARGS(1:NLOC,3)
      W(1:NLOC,1) = ARGS(1:NLOC,4)
      P(1:NLOC,1) = ARGS(1:NLOC,5)
      AL(1:NLOC,1) = ARGS(1:NLOC,6)
C
C Initialise RET(1:NLOC*NRET) to zero.
C
      DO ILOC = 1, NLOC
        CALL CBESSJ(COMPLEX(AL(ILOC,1)*
     &    R(ILOC,1)/0.01905,0.)*(I**(3./2.)),0,B)
        CALL
CBESSJ(COMPLEX(AL(ILOC,1),0.)*(I**(3./2.)),0,C)
        B=(COMPLEX(A(ILOC,1)/(P(ILOC,1)*W(ILOC,1)),0.)/I)
     &   *(COMPLEX(1.0,0.)-B/C)*EXP(I*COMPLEX(W(ILOC,1)
     &   *(T(ILOC,1)+18.0238016767),0.))
        RET(ILOC,1)=REAL(B)
      ENDDO
C
C Set success flag.
      CRESLT = 'GOOD'
C
C=============================================================
=============
      END SUBROUTINE WOM
C
        real*8 Function Fact(K)
        integer i
        real*8  f
          F=1.d0
          do i=2, k
            f=f*dfloat(i)
          end do
          Fact=f
        return
        End Function Fact
C
*****************************************
*           FUNCTION  GAMMA(X) [129]      *
* ------------------------------------- *
* Returns the value of Gamma(x) in double *
* precision as EXP(LN(GAMMA(X))) for X>0. *
*****************************************
      real*8 Function Gamma(xx)
      parameter(ONE=1.d0,FPF=5.5d0,HALF=0.5d0)
        real*8 xx
```

```
        real*8 cof(6)
        real*8 stp,x,tmp,ser
        integer j
        cof(1)=76.18009173d0
        cof(2)=-86.50532033d0
        cof(3)=24.01409822d0
        cof(4)=-1.231739516d0
        cof(5)=0.120858003d-2
        cof(6)=-0.536382d-5
        stp=2.50662827465d0

        x=xx-ONE
        tmp=x+FPF
        tmp=(x+HALF)*LOG(tmp)-tmp
        ser=ONE
        do j=1, 6
          x=x+ONE
          ser=ser+cof(j)/x
        end do
        Gamma = EXP(tmp+LOG(stp*ser))
      return
      End function gamma


      Subroutine CBESSJ(z, nu, z1)
C!-------------------------------------------------
C!                          inf.      (-z^2/4)^k
C!   Jnu(z) = (z/2)^nu x Sum  ------------------
C!                          k=0   k! x Gamma(nu+k+1)
C!  (nu must be >= 0).
C!-------------------------------------------------
        Parameter(MAXK=20,ZERO=0.d0)
        Complex z,z1
        Integer k
        Complex sum,tmp
        Real*8 Fact, Gamma
        sum = CMPLX(ZERO,ZERO)
        do k=0, MAXK
          !calculate (-z**2/4)**k
      tmp = (-z*z/4.d0)**k
          !divide by k!
      tmp = tmp / Fact(k)
          !divide by Gamma(nu+k+1)
          tmp = tmp / Gamma(dfloat(nu+k+1))
          !actualize sum
      sum = sum + tmp
        end do
```

```
        !calculate (z/2)**nu
        tmp = (z/2)**nu
        !multiply (z/2)**nu by sum
        z1 = tmp*sum
      return
      End

C!end of file wom.F
```

APPENDIX C.

WAVEFORM GENERATION CODES

```
%+-----------------------------------------+
%| for generation of waveforms using pressure|
%| control                                 |
%+-----------------------------------------+
function [Vmax,Qmax,Qmin]=PCon3(prn,R,C,sc)
T=2;
dt=0.001;
if(prn~=3)
    t1=(0:dt:0.5*T);
    t2=(0.5*T:dt:2*T);
    t=[t1,t2];
else
    t=(0:dt:5*T);
end

P=zeros(size(t));
V=zeros(size(t));
Q=zeros(size(t));

if(prn==1)
    P=P1(t,sc);
    [~,V]=runkut(0,t,@Qin,R,C,@P1,sc);
    Q=Qin(t,V,R,C,@P1,sc);
elseif(prn==2)
    P=P2(t,sc);
    [~,V]=runkut(0,t,@Qin,R,C,@P2,sc);
    Q=Qin(t,V,R,C,@P2,sc);
elseif(prn==3)
    P=P3(t,sc);
    [~,V]=runkut(0,t,@Qin,R,C,@P3,sc);
    Q=Qin(t,V,R,C,@P3,sc);
end

% A=pi/4*(19*10^(-3))^2;
% Q=Q/1000;
% G=Q/A;
V=V*1000;
Q=Q*60;

Vmax=max(V);
Qmax=max(Q);
Qmin=min(Q);

vfrr=153846153.846154;

np=ceil(Q*0.000016666666667*vfrr*dt);
Np=V*10^(-6)*vfrr;
```

```
disp(sum(np(1:ceil(length(np)*1.042/4))));
disp(ceil(length(np)*1.042/4));

po='b';
subplot(3,1,1);
plot(t,P,po);
title('Pressure');
xlabel('time(s)');
ylabel('Pressure(cm H_2O)');
subplot(3,1,2);
plot(t,V,po);
title('Volume');
xlabel('time(s)');
ylabel('Volume(mL)');
subplot(3,1,3);
plot(t,Q,po);
title('Flow');
xlabel('time(s)');
ylabel('Flow(L/min)');

disp(V(end));

Ain=pi/4*(8.35868*10^(-3))^2;%pi/4*(16.4E-3)^2;
K=Q/60/1000/Ain;

figure;
plot(t,Np,'b.');

filename=strcat('pr',num2str(prn),'.csv');
file=fopen(filename,'wt');
fprintf(file,'[name]\ninlet\n\n[Spatial
Fields]\nt\n\n[Data]\nt [s],Velocity [m s^-1]\n');
for i=1:length(t)
    fprintf(file,'%1.6E,%1.6E\n',t(i),K(i));
end
fclose(file);

filename=strcat('Npr',num2str(prn),'.csv');
file=fopen(filename,'wt');
fprintf(file,'[name]\nRealPartNum\n\n[Spatial
Fields]\nt\n\n[Data]\nt [s],NPR []\n');
for i=1:length(t1)
    fprintf(file,'%1.6E,%1.6E\n',t(i),Np(i));
end
fclose(file);
```

```
%definition of pressure curve
function [z]=P1(t,sc)
z=sc*ones(size(t)).*sig(t).*rsig(t,1);

function [z]=P2(t,sc)
z=sc*(1-exp(-4*t)).*rsig(t,1);

function [z]=P3(t,sc)
z=sc/3*(1-cos(2*pi*t));

function [z]=sig(t)
td=0.1;
z=(1/2-1/2*cos(t*pi/td)).*(1-heaviside(t-
td))+1*heaviside(t-td);

function [z]=rsig(t,s)
td=0.1;
z=(1/2-1/2*cos((t-s)*pi/td+pi)).*(heaviside(t-s)).*(1-
heaviside(t-(s+td)))+(1-heaviside(t-s));



%differential equation
function [Vdot]=Qin(t,V,R,C,Pr,sc)
Vdot=Pr(t,sc)/R-V/(C*R);


%+-----------------------------------------+
%| for generation of waveforms using volume  |
%| control                                   |
%+-----------------------------------------+
function [Vmax,Qmax,Qmin]=VCon3(von,R,C,sc)
T=2;
dt=0.001;
t1=(0:dt:0.5*T);
t2=(0.5*T:dt:2*T);
t=[t1,t2];

P=zeros(size(t));
V=zeros(size(t));
Q=zeros(size(t));

if(von==1)
    V(1:length(t1))=V1(t1,sc);
    for i=1:length(t1)-1
        Q(i)=((V(i+1)-V(i))/(t1(i+1)-t1(i)))*sig(t1(i));
```

```
    end
    Q(length(t1))=(V(length(t1))-V(length(t1)-1))/(t1(end)-
t1(end-1));
    V(1)=0;
    for i=2:length(t1)
        V(i)=V(i-1)+(Q(i)+Q(i-1))*(t1(i)-t1(i-1))/2;
    end
elseif(von==2)
    V(1:length(t1))=V2(t1,sc);
    for i=1:length(t1)-1
        Q(i)=(V(i+1)-V(i))/(t1(i+1)-t1(i));
    end
    Q(length(t1))=(V(length(t1))-V(length(t1)-1))/(t1(end)-
t1(end-1));
end

P(1:length(t1))=Q(1:length(t1))*R+V(1:length(t1))/C;

P(length(t1)+1:length(t))=Pr(t2,P(length(t1)));
[~,V(length(t1)+1:length(t))]=runkut(V(length(t1)),t2,@Qout
,R,C,@Pr,P(length(t1)));
Q(length(t1)+1:length(t))=Qout(t2,V(length(t1)+1:length(t))
,R,C,@Pr,P(length(t1)));

% P(length(t1)+1:length(t))=Pr(t2,P(length(t1)));
%
[~,V(length(t1)+1:length(t))]=runkut(V(length(t1)),t2,@Qout
,R,C,@Pr,P(length(t1)));
%
Q(length(t1)+1:length(t))=Qout(t2,V(length(t1)+1:length(t))
,R,C,@Pr,P(length(t1)));

V=V*1000;
Q=Q*60;

Vmax=max(V);
Qmax=max(Q);
Qmin=min(Q);

vfrr=153846153.846154;

np=ceil(Q*0.000016666666667*vfrr*dt);
Np=V*10^(-6)*vfrr;

disp(sum(np(1:ceil(length(np)*1.042/4))));
disp(ceil(length(np)*1.042/4));
```

```
% P=P/98.0665;
% V=V*1000*1000;
% Q=Q*60000;

po='b';
subplot(3,1,1);
plot(t,P,po);
title('Pressure');
xlabel('time(s)');
ylabel('Pressure(cm H_2O)');
subplot(3,1,2);
plot(t,V,po);
title('Volume');
xlabel('time(s)');
ylabel('Volume(mL)');
subplot(3,1,3);
plot(t,Q,po);
title('Flow');
xlabel('time(s)');
ylabel('Flow(L/min)');

Ain=pi/4*(8.35868*10^(-3))^2;
K=Q/60/1000/Ain;

figure;
plot(t,Np,'b.');

filename=strcat('vo',num2str(von),'.csv');
file=fopen(filename,'wt');
fprintf(file,'[name]\ninlet\n\n[Spatial
Fields]\nt\n\n[Data]\nt [s],Velocity [m s^-1]\n');
for i=1:length(t)
    fprintf(file,'%1.6E,%1.6E\n',t(i),K(i));
end
fclose(file);

filename=strcat('Nvo',num2str(von),'.csv');
file=fopen(filename,'wt');
fprintf(file,'[name]\nRealPartNum\n\n[Spatial
Fields]\nt\n\n[Data]\nt [s],NPR []\n');
for i=1:length(t1)
    fprintf(file,'%1.6E,%1.6E\n',t(i),Np(i));
end
fclose(file);

%definition of volume curves
function [z]=V1(t,sc)
```

```
z=sc*10^(-3)*0.9927*t;

function [z]=V2(t,sc)
z=sc*10^(-3)*(1/2-1/2*cos(pi*t));

function [z]=sig(t)
td=0.1;
z=(1/2-1/2*cos(t*pi/td)).*(1-heaviside(t-
td))+1*heaviside(t-td);

function [z]=rsig(t,s)
td=0.1;
z=(1/2-1/2*cos((t-s)*pi/td+pi)).*(heaviside(t-s)).*(1-
heaviside(t-(s+td)))+(1-heaviside(t-s));

function [z]=Pr(t,p)
z=p*rsig(t,1);

%differential equation
function [Vdot]=Qout(t,V,R,C,Pr,s)
Vdot=Pr(t,s)/R-V/(C*R);


%+-----------------------------------------+
%| for generation of waveforms using flow  |
%| control                                 |
%+-----------------------------------------+
function [Vmax,Qmax,Qmin]=QCon3(Qn,R,C,sc)
T=2;
dt=0.001;
t1=(0:dt:0.5*T);
t2=(0.5*T:dt:2*T);
t=[t1,t2];

P=zeros(size(t));
V=zeros(size(t));
Q=zeros(size(t));

if(Qn==3)
    t=(0:dt:2*T);
    t1=(0:dt:T);
    t2=(T:dt:2*T);
    V=zeros(size(t));
    Q=Q3(t,sc);
    V(1)=0;
    for i=2:length(t)
        V(i)=V(i-1)+(Q(i)+Q(i-1))*(t(i)-t(i-1))/2;
```

```
    end
    P=Q*R+V/C;
else
if(Qn==1)
    Q(1:length(t1))=Q1(t1,sc);
elseif(Qn==2)
    Q(1:length(t1))=Q2(t1,sc);
end
V(1)=0;
for i=2:length(t1)
    V(i)=V(i-1)+(Q(i)+Q(i-1))*(t1(i)-t1(i-1))/2;
end
P(1:length(t1))=Q(1:length(t1))*R+V(1:length(t1))/C;
P(length(t1)+1:length(t))=Pr(t2,P(length(t1)));
[~,V(length(t1)+1:length(t))]=runkut(V(length(t1)),t2,@Qout
,R,C,@Pr,P(length(t1)));
Q(length(t1)+1:length(t))=Qout(t2,V(length(t1)+1:length(t))
,R,C,@Pr,P(length(t1)));
end

V=V*1000;
Q=Q*60;

Vmax=max(V);
Qmax=max(Q);
Qmin=min(Q);

vfrr=153846153.846154;

np=ceil(Q*0.000016666666667*vfrr*dt);
Np=V*10^(-6)*vfrr;

disp(sum(np(1:ceil(length(np)*1.042/4))));
disp(ceil(length(np)*1.042/4));

% P=P/98.0665;
% V=V*1000*1000;
% Q=Q*60000;

po='b';
subplot(3,1,1);
plot(t,P,po);
title('Pressure');
xlabel('time(s)');
ylabel('Pressure(cm H_2O)');
subplot(3,1,2);
plot(t,V,po);
```

```
title('Volume');
xlabel('time(s)');
ylabel('Volume(mL)');
subplot(3,1,3);
plot(t,Q,po);
title('Flow');
xlabel('time(s)');
ylabel('Flow(L/min)');

Ain=pi/4*(8.35868*10^(-3))^2;
K=Q/60/1000/Ain;

figure;
plot(t,Np,'b.');

filename=strcat('Q',num2str(Qn),'.csv');
file=fopen(filename,'wt');
fprintf(file,'[name]\ninlet\n\n[Spatial
Fields]\nt\n\n[Data]\nt [s],Velocity [m s^-1]\n');
for i=1:length(t)
    fprintf(file,'%1.6E,%1.6E\n',t(i),K(i));
end
fclose(file);

filename=strcat('Nq',num2str(Qn),'.csv');
file=fopen(filename,'wt');
fprintf(file,'[name]\nRealPartNum\n\n[Spatial
Fields]\nt\n\n[Data]\nt [s],NPR []\n');
for i=1:length(t1)
    fprintf(file,'%1.6E,%1.6E\n',t(i),Np(i));
end
fclose(file);

%definition of flow rate curves
function [z]=Q1(t,sc)
z=sc*0.9808*(2*t);

function [z]=Q2(t,sc)
z=sc*(2-2*t).*sig(t);

function [z]=Q3(t,sc)
z=sc*sin(2/4*pi*t);

function [z]=sig(t)
td=0.1;
z=(1/2-1/2*cos(t*pi/td)).*(1-heaviside(t-
td))+1*heaviside(t-td);
```

```
function [z]=rsig(t,s)
td=0.1;
z=(1/2-1/2*cos((t-s)*pi/td+pi)).*(heaviside(t-s)).*(1-
heaviside(t-(s+td)))+(1-heaviside(t-s));

function [z]=Pr(t,p)
z=p*rsig(t,1);

%differential equation
function [Vdot]=Qout(t,V,R,C,Pr,s)
Vdot=Pr(t,s)/R-V/(C*R);
```

BIBLIOGRAPHY

1. Hickey, A.J., *Pharmaceutical inhalation aerosol technology*. Vol. 56. 1992, New York, NY: Marcel Dekker.

2. Dreyfuss, D. and G. Saumon, *From Ventilator-Induced Lung Injury to Multiple Organ Dysfunction.* Intensive Care Medicine, 1998. **24**: p. 102-104.

3. Kleinstreuer, C. and Z. Zhang, *Airflow and particle transport in the human respiratory system.* Annual Review of Fluid Mechanics, 2009. **42**: p. 301-334.

4. Levitzky, M.G., *Pulmonary Physiology*. 2003: McGraw-Hill Proefessional. 278.

5. Hickey, A.J., *Inhalation aerosols: physical and biological basis for therapy.* Vol. 94. 1996, New York, NY: Marcel Dekker.

6. Starr, C., C. Evers, and L. Starr, *Biology: today and tomorrow: with physiology*. 3 ed. 2009: Cengage Learning.

7. *The Oropharynx and Hypopharynx*. 03/12/2011 [cited 2012 03/19]; Available from: http://www.painneck.com/oropharynx-hypopharynx.

8. Horsfield, K., *Models of the Human Bronchial Tree.* Journal of Applied Physilology, 1971. **31**(2): p. 207-217.

9. Weibel, E.R., *Morphological Basis of Alveolar-Capillary Gas Exchange.* Physiological Reviews, 1973. **53**(2): p. 419-495.

10. Mobley, C. and G. Hochhaus, *Methods used to assess pulmonary deposition and absorption of drugs.* Drug Discovery Today, 2001. **6**(7): p. 367-375.

11. White, F.M., *Fluid Mechanics*. 6 ed. 2008: McGraw-Hill Higher Education. 864.

12. Olson, D.E., et al., *Convective Patterns of Flow Durrring Inspiration.* Archives of Internal Medicine, 1973. **131**: p. 51-57.

13. Kleinstreuer, C. and Z. Zhang, *Airflow and particle transport in the human respiratory system.* Annual Review of Fluid Mechanics, 2010. **42**: p. 301-334.

14. Kleinstreuer, C., Z. Zhang, and J.F. Donohue, *Targeted Drug-Aerosol Delivery in the Human Respiratory System.* Annual Review of Biomedical Engineering, 2008. **10**: p. 195-220.

15. Bouhuys, A., *Breathing; physiology, environment and lung disease*. 1974: Grune & Stratton. 511.

16. Thurlbeck, W.M. and A. Churg, *Pathology of the lung*. 1995: Thieme Medical Publishers.

17. Weibel, E.R., *Morphometry of the human lung*. 1963, New York, NY: Academic.

18. Xia, G., et al., *Airway Wall Stiffening Increases Peak Wall Shear Stress: A Fluid–Structure Interaction Study in Rigid and Compliant Airways.* Annals of Biomedical Engineering, 2010. **38**(5): p. 1836-1853.

19. Zhang, H. and G. Papadakis, *Computational analysis of flow structure and particle deposition in a single asthmatic human airway bifurcation.* Journal of Biomechanics, 2010. **43**: p. 2453-2459.

20. Nagels, M.A. and J.E. Carter, *Large eddy simulation of high frequency oscillating flow in an asymmetric branching airway model.* Medical Engineering and Physics, 2009. **31**: p. 1148-1153.

21. Comer, J.K., C. Kleinstreuer, and C.S. Kim, *Flow structures and particle deposition patterns in double-bifurcation airway models. Part 2. Aerosol transport and deposition.* Journal of Fluid Mechanics, 2001b. **435**: p. 55-80.

22. Comer, J.K., C. Kleinstreuer, and Z. Zhang, *Flow structures and particle deposition patterns in double-bifurcation airway models. Part 1. Air flow fields.* Journal of Fluid Mechanics, 2001a. **435**: p. 25-54.

23. Zhang, Z., et al., *Comparison of micro- and nano-size particle depositions in a human upper airway model.* Journal of Aerosol Science, 2005. **36**: p. 211-233.

24. Longest, P.W. and J. Xi, *Effectiveness of direct Lagrangian tracking models for simulating nanoparticle deposition in the upper airways.* Aerosol Science & Technology, 2007. **41**: p. 380-397.

25. Kleinstreuer, C., et al., *A new methodology for targeting drug-aerosols in the human respiratory system.* International Journal of Heat and Mass Transfer, 2008. **51**: p. 5578-5589.

26. Xi, J. and P.W. Longest, *Transport and Deposition of Micro-Aerosols in Realistic and Simplified Models of the Oral Airway.* Annals of Biomedical Engineering, 2007. **35**(4): p. 560-581.

27. Zhang, Z. and C. Kleinstreuer, *Laminar-to-turbulent fluid–nanoparticle dynamics simulations: Model comparisons and nanoparticle-deposition applications.* International Journal for Numerical Methods in Biomedical Engineering, 2011. **27**: p. 1930-1950.

28. Choi, J., et al., *On intra- and intersubject variabilities of airflow in human lungs.* Physics of Fluids, 2009. **21**: p. 101901: 1-17.

29. Inthavong, K., et al., *Micron particle deposition in a tracheobronchial airway model under different breathing conditions.* Medical Engineering and Physics, 2010. **32**: p. 1198-1212.

30. Xi, J., P.W. Longest, and T.B. Martonen, *Effects of the laryngeal jet on nano- and microparticle transport and deposition in an approximate model of the upper tracheobronchial airways.* Journal of Applied Physiology, 2008. **104**: p. 1761-1777.

31. Lambert, A.R., et al., *Regional deposition of particles in an image-based airway model: large-eddy simulation and left-right lung ventilation asymmetry.* Aerosol Science & Technology, 2011. **45**(1): p. 11-25.

32. Groβe, S., et al., *Time resolved analysis of steady and oscillating flow in the upper human airways.* Experiments in Fluids, 2007. **42**: p. 955-970.

33. Zhang, Y. and W.H. Finlay, *Measurement of the Effect of Cartilaginous Rings on Particle Deposition in a Proximal Lung Bifurcation Model.* Aerosol Science and Technology, 2005. **39**: p. 394-399.

34. Fresconi, F.E. and A.K. Prasad, *Secondary Velocity Fields in the Conducting Airways of the Human Lung.* Journal of Biomechanical Engineering, 2007. **129**: p. 722-732.

35. Kim, C.S. and D.M. Fisher, *Deposition Characteristics of Aerosol Particles in Sequentially Bifurcating Airway Models.* Aerosol Science and Technology, 1999. **31**(2): p. 198-220.

36. Papadakos, P. and B. Lachmann, *Mechanical Ventilation: Clinical Applications and Pathophysiology*. Vol. 23. 2007: Elsevier Health Sciences. 665.

37. Esteban, A., et al., *How Is Mechanical Ventilation Employed in the Intensive Care Unit?* American Journal of Respiratory and Critical Care Medicine, 2000. **161**: p. 1450-1458.

38. Kollef, M.H., et al., *The Use of Continuous IV Sedation Is Associated With Prolongation of Mechanical Ventilation.* Chest, 1998. **114**: p. 541-548.

39. Esteban, A., et al., *Characteristics and Outcomes in Adult Patients Receiving Mechanical Ventilation.* Journal of the American Medical Association, 2002. **287**(3): p. 345-355.

40. Gonda, I., *The Ascent of Pulmonary Drug Delivery.* Journal of Pharmaceutical Science, 2000. **89**(7): p. 940-945.

41. Dhand, R., *Aerosol Delivery During Mechanical Ventilation: From Basic Techniques to New Devices.* Journal of Aerosol Medicine and Pulmonary Drug Delivery, 2008. **21**(1): p. 45-60.

42. Hess, D.R., T.R. Myers, and J.L. Rau, *A Guide to Aerosol Delivery Devices for Respiratory Therapists*, A.A.f.R. Care, Editor. 2007.

43. Slutsky, A.S., *Lung Injury Caused by Mechanical Ventilation.* Chest, 1999. **116**: p. 9S-15S.

44. Yeow, M.E. and J.I. Santanilla, *Noninvasive Positive Pressure Ventilation in the Emergency Department.* Emergency Medicine Clinics of North America, 2008. **26**: p. 835-847.

45. Soni, N. and P. Williams, *Positive pressure ventilation: what is the real cost?* British Journal of Anaesthesia, 2008. **101**(4): p. 446-457.

46. Young, P.J., *Ventilatory Support.* Surgery (Oxford), 2003. **21**(3): p. 77-80.

47. MacIntyre, N.R. and R.D. Branson, *Mechanical Ventilation*. 2009, St. Louis, Missouri: Elsevier.

48. Nikischin, W., et al., *A New Method to Analyze Lung Compliance When Pressure–Volume Relationship Is Nonlinear.* American Journal of Respiratory and Critical Care Medicine, 1998. **158**: p. 1052-1060.

49. Vanrhein, T. and A. Banerjee. *Numerical investigation of aerosolized drug delivery in the human lungs under mechanical ventilator conditions.* in *American Physical Society- Division of Fluid Dynamics Annual Meeting*. 2010. Long Beach, CA: APS.

50. Gibson, B., *Long-term Ventilation for Patients WIth Duchenne Muscular Dystrophy: Physicians' Beliefs and Practices.* Chest, 2001. **119**(3): p. 940-946.

51. Pascal, S., P. Diot, and E. Lemarie, *Antibiotics in Aerosols.* Revue des Maladies Respiratoires, 1992. **9**(2): p. 145-153.

52. Vonnegut, B. and R.L. Neubauer, *Production of Monodisperse Liquid Particles by Electrical Atomization.* Journal of Colloid Science, 1952. **7**: p. 616-622.

53. Vecellio, L., *The mesh nebuliser: a recent technical innovation for aerosol delivery.* Breathe, 2006. **2**(3): p. 253-260.

54. Newman, S.P., *Principles of Metered-Dose Inhaler Design.* Respiratory Care, 2005. **50**(9): p. 1177-1188.

55. Dhand, R., *Inhalation Therapy With Metered-Dose Inhalers and Dry Powder Inhalers in Mechanically Ventilated Patients.* Respiratory Care, 2005. **50**(10): p. 1331-1345.

56. Kulkarni, P., P.A. Baron, and K. Willeke, *Aerosol Measurement: Principles, Techniques, and Applications*. 3 ed. 2011: John Wiley & Sons.

57. Meibohm, B., *Pharmacokinetics and pharmacodynamics of biotech drugs: principles and case studies in drug development*, ed. B. Meibohm. 2006: Wiley-VCH.

58. van Thienen, P., J.H.G. Vreeburg, and E.J.M. Blokker, *Radial transport processes as a precursor to particle deposition in drinking water distribution systems.* Water Research, 2011. **45**: p. 1807-1817.

59. Metzger, R.J., et al., *The Branching Progamme of Mouse Lung Development.* Nature, 2008. **453**: p. 745-751.

60. Lee, J.M., et al., *Lung tissue regeneration after induced injury in Runx3 KO mice.* Cell and Tissue Research, 2010. **341**: p. 465-470.

61. Armstrong, J.J., et al., *In vivo size and shape measurement of the human upper airway using endoscopic longrange optical coherence tomography.* Optics Express, 2003. **11**(15): p. 1817-1826.

62. Kleinstreuer, C., Z. Zhang, and L. Zheng, *Modeling airflow and particle transport/deposition in pulmonary airways.* Respiratory Physiology & Neurobiology, 2008. **163**: p. 128-138.

63. Luo, X.Y., et al., *LES Modelling of Flow in a Simple Airway Model.* Medical Engineering and Physics, 2004. **26**: p. 403-413.

64. Gemci, T., et al., *Computational model of airflow in upper 17 generations of human respiratory tract.* Journal of Biomechanics, 2008. **41**: p. 2047-2054.

65. Sandeau, J., et al., *CFD simulation of particle deposition in a reconstructed human oral extrathoracic airway for air and helium–oxygen mixtures.* Journal of Aerosol Science, 2010. **41**: p. 281-294.

66. Balashazy, I. and W. Hofmann, *PARTICLE DEPOSITION IN AIRWAY BIFURCATIONS--I. INSPIRATORY FLOW.* Journal of Aerosol Science, 1993. **24**(6): p. 745-772.

67. Balashazy, I., W. Hofmann, and H. T., *Computation of local enhancement factors for the quantification of particle deposition patterens in airway bifurcations.* Journal of Aerosol Science, 1999. **30**(2): p. 185-203.

68. Wilson, A.J., et al., *A computer model of the artificially ventilated human respiratory system in adult intensive care.* Medical Engineering and Physics, 2009. **31**: p. 1118-1133.

69. De Backer, J.W., et al., *Validation of Computational Fluid Dynamics in CT-based Airway Models with SPECT/CT.* Radiology, 2010. **257**(3): p. 854-862.

70. Luo, H.Y. and Y. Liu, *Particle deposition in a CT-scanned human lung airway.* Journal of Biomechanics, 2009. **42**: p. 1869-1876.

71. Choi, J., et al., *Numerical study of High-Frequency Oscillatory Air Flow and Convective Mixing in a CT-Based Human Airway Model.* Annals of Biomedical Engineering, 2010. **38**(12): p. 3550-3571.

72. Nithiarasu, P., et al., *Steady flow through a realistic human upper airway geometry.* International Journal for Numerical Methods in Fluids, 2008. **57**: p. 631-651.

73. Jeong, S.J., W.S. Kim, and S.J. Sung, *Numerical investigation on the flow characteristics and aerodynamic force of the upper airway of patient with obstructive sleep apnea using computational fluid dynamics.* Medical Engineering and Physics, 2007. **29**: p. 637-651.

74. *Getting Started: First Steps with MeVisLab*. 2009, MeVis Medical Solutions.

75. Soret, M., S.L. Bacharach, and I. Buvat, *Partial-Volume Effect in PET Tumor Imaging.* Journal of Nuclear Medicine, 2007. **48**: p. 932-945.

76. Yim, Y. and H. Hong, *Smoothing Segmented Lung Boundary in Chest CT Images Using Scan Line Search Progress in Pattern Recognition, Image Analysis and Applications*, J. Martínez-Trinidad, J. Carrasco Ochoa, and J. Kittler, Editors. 2006, Springer Berlin / Heidelberg. p. 147-156.

77. Zhang, Y., W.H. Finlay, and E.A. Matida, *Particle deposition measurements and numerical simulation in a highly idealized mouth–throat.* Journal of Aerosol Science, 2004. **35**: p. 789-803.

78. Grgic, B., W.H. Finlay, and A.F. Heenan, *Regional aerosol deposition and ow measurements in an idealized mouth and throat.* Journal of Aerosol Science, 2004. **35**: p. 21-32.

79. Li, W., et al., *Aerodynamics and Aerosol Particle Deaggregation Phenomena in Model Oral-Pharyngeal Cavities.* Journal of Aerosol Science, 1996. **27**(8): p. 1269-1286.

80. Matida, E.A., et al., *Improved numerical simulation of aerosol deposition in an idealized mouth–throat.* Journal of Aerosol Science, 2004. **35**: p. 1-19.

81. Nowak, N., P.P. Kakade, and A.V. Annapragada, *Computational Fluid Dynamics Simulation of Airflow and Aerosol Deposition in Human Lungs.* Annals of Biomedical Engineering,, 2003. **31**: p. 374-390.

82. Katz, I.M., B.M. Davis, and T.B. Martonen, *A numerical study of particle motion within the human larynx and trachea.* journal of Aerosol Science, 1999. **30**(2): p. 173-183.

83. Lin, C.-L., et al., *Characteristics of the turbulent laryngeal jet and its effect on airflow in the human intra-thoracic airways.* Respiratory Physiology and Neurobiology, 2007. **57**(2-3): p. 295-309.

84. Stapleton, K.W., et al., *On the suitability of k-epsilon turbulence modeling for aerosol deposition in the mouth and throat: a comparison with experiment.* Journal of Aerosol Science, 2000. **31**(6): p. 739-749.

85. Corcoran, T.E. and N. Chigier, *Characterization of the Laryngeal Jet Using Phase Doppler Interferometry.* Journal of Aerosol Medicine, 2000. **13**(2): p. 125-137.

86. Martonen, T.B., Y. Yang, and Z.Q. Xue, *Influences of cartilaginous rings on tracheobronchial fluid dynamics.* Inhaliation Toxicology, 1994. **6**(3): p. 185-203.

87. Li, Z., C. Kleinstreuer, and Z. Zhang, *Simulation of airflow fields and microparticle deposition in realistic human lung airway models. Part II: Particle transport and deposition.* European Journal of Mechanics B/Fluids, 2007. **26**: p. 650-668.

88. Martonen, T.B., Y. Yang, and Z.Q. Xue, *Effects of Carinal Ridge Shapes on Lung Airstreams.* Aerosol Science and Technology, 1994. **21**: p. 119-136.

89. Martonen, T.B. and X. Guan, *Effects of Tumors on Inhaled Pharmacologic Drugs. I. Flow Patterns.* Cell Biochemistry and Biophysics, 2001. **35**: p. 233-243.

90. Martonen, T.B., *Effects of Tumors on Inhaled Pharmacologic Drugs. II. Particle Motion.* Cell Biochemistry and Biophysics, 2001. **35**: p. 245-253.

91. Zhang, Z., et al., *Aerosol transport and deposition in a triple bifurcation bronchial airway model with local tumors.* Inhaliation Toxicology, 2002. **14**(11): p. 1111-1133.

92. Straus, C., et al., *Contribution of the Endotracheal Tube and the Upper Airway to Breathing Workload.* American Journal of Respiratory and Critical Care Medicine, 1998. **157**(1): p. 23-30.

93. Al-Majed, S.I., et al., *Effect of lung compliance and endotracheal tube leakage on measurement of tidal volume.* Critical Care Medicine, 2009. **8**(6): p. 398-402.

94. Fontan, J.J.P., G.P. Heldt, and G.A. Gregory, *Resistance and inertia of endotracheal tubes used in infants durring periodic flow.* Critical Care Medicine, 1985. **13**(12): p. 1052-1055.

95. Cherng, C.H., et al., *Airway Length in Adults: Estimation of the Optimal Endotracheal Tube Length for Orotracheal Intubation.* Journal of Clinical Anesthesia, 2002. **14**: p. 271-274.

96. Longest, P.W. and S.C. Vinchurkar, *Effects of mesh style and grid convergence on particle deposition in bifurcating airway models with comparisons to experimental data.* Medical Engineering and Physics, 2007. **29**: p. 350-366.

97. Vinchurkar, S.C. and P.W. Longest, *Evaluation of hexahedral, prismatic and hybrid mesh styles for simulating respiratory aerosol dynamics.* Computers and Fluids, 2008. **37**: p. 317-331.

98. *ANSYS CFX 13.0 Solver Modeling Guide*. 2010: ANSYS INC.

99. Xi, J. and P.W. Longest, *Effects of Oral Airway Geometry Characteristics on the Diffusional Deposition of Inhaled Nanoparticles.* Journal of Biomechanical Engineering, 2008. **130**(1): p. 011008-1-011008-16.

100. Isaacs, K.K., R.B. Schlesinger, and T.B. Martonen, *Three-dimensional Computational Fluid Dynamics Simulations of Particle Deposition in the Tracheobronchial Tree.* Journal of Aerosol Medicine, 2006. **19**(3): p. 344-352.

101. Zhang, Z., C. Kleinstreuer, and C.S. Kim, *Airflow and nanoparticle deposition in a 16-generation Tracheobronchial Airway Model.* Annals of Biomedical Engineering, 2008. **36**(12): p. 2095-2110.

102. Farkas, A. and I. Balashazy, *Simulation of the effect of local obstructions and blockage on airflow and aerosol deposition in central human airways.* Journal of Aerosol Science, 2007. **38**: p. 865-884.

103. *ANSYS ICEM 13.0 Documentation*. 2010: SAS IP, Inc.

104. Anderson, J.D., *Computational fluid dynamics: the basics with applications*. 1995: McGraw-Hill.

105. Nicoud, F. and D. F., *Subgrid-Scale Stress Modelling Based on the Square of the Velocity Gradient Tensor.* Flow, Turbulence, and Combustion, 1999. **62**(3): p. 183-200.

106. Wang, Q. and K.D. Squires, *Large Eddy Simulation of Particle Deposition in a Vertical Turbulent Channel Flow.* International Journal of Multiphase Flow, 1996. **22**(4): p. 667-683.

107. Pope, S.B., *Turbulent Flows*. 2001: Cambridge University Press.

108. Armenio, V., U. Piomelli, and V. Fiorotto, *Effect of the Subgrid Scales on Particle Motion.* Physics of Fluids, 1999. **11**(10): p. 3030-3042.

109. *ANSYS CFX 13.0 Solver Theory Guide*. 2010: ANSYS INC.

110. Morsi, S.A. and A.J. Alexander, *An investigation of particle trajectories in two-phase flow systems.* Journal of Fluid Mechanics, 1972. **55**: p. 193-208.

111. Crowe, C.T., *Multiphase Flow Handbook.* illustrated ed, ed. C.T. Crowe. 2006: CRC Press. 1156.

112. Longest, P.W., C. Kleinstreuer, and J.R. Buchanan, *Efficient computation of micro-particle dynamics including wall effects.* Computers & Fluids, 2004. **33**: p. 577-601.

113. Cherukat, P. and J.B. McLaughlin, *The inertial lift on a rigid sphere in a linear shear flow field near a flat wall.* Journal of Fluid Mechanics, 1994. **263**: p. 1-18.

114. Li, A. and G. Ahmadi, *Dispersion and deposition of spherical particles from point sources in a turbulent channel flow.* Aerosol Science & Technology, 1992. **16**: p. 209-226.

115. Ma, B. and K.R. Lutchen, *An Anatomically Based Hybrid Computational Model of the Human Lung and its Application to Low Frequency Oscillatory Mechanics.* Annals of Biomedical Engineering, 2006. **34**(11): p. 1691-1704.

116. van Ertbruggen, C., C. Hirsch, and M. Paiva, *Anatomically based three-dimensional model of airways to simulate flow and particle transport using computational fluid dynamics.* Journal of Applied Physilology, 2005. **98**: p. 970-980.

117. Lieber, B.B. and Y. Zhao, *Oscillatory Flow in a Symmetric Bifurcation Airway Model.* Annals of Biomedical Engineering, 1998. **26**: p. 821-830.

118. Grimby, G., et al., *Frequency Dependence of Flow Resistance in Patients with Obstructive Lung Disease.* Journal of clinical Investigation, 1968. **47**: p. 1455-1465.

119. Zhao, Y. and B. Lieber, *Steady inspiratory flow in a model symmetric bifurcation.* J Biomech Eng., 1994. **116**(4): p. 488-496.

120. Jan, D.L., A.H. Shapiro, and R.D. Kamm, *Some features of oscillatory flow in a model bifurcation.* Journal of Applied Physiology, 1989. **67**: p. 147-159.

121. Womersley, J.R., *Method for The Calculation of Velocity, Rate of Flow, and Viscous Drag in Arteries When The Pressure Gradient is Known.* Journal of Physiology, 1955. **127**: p. 553-563.

122. Dean, W.R., *Fluid Motion in a Curved Channel.* Proceedings of the Royal Society of London. Series A, 1928. **121**: p. 402-420.

123. Moller, W., et al., *Deposition, Retention, and Translocation of Ultrafine Particles from the Central Airways and Lung Periphery.* American Journal of Respiratory and Critical Care Medicine, 2008. **177**: p. 426-432.

124. Ma, B., et al., *CFD simulation and experimental validation of fluid flow and particle transport in a model of alveolated airways.* Journal of Aerosol Science, 2009. **40**: p. 403-414.

125. Zhang, Z., C. Kleinstreuer, and C.S. Kim, *Comparison of analytical and CFD models with regard to micron particle deposition in a human16-generation tracheobronchial airway model.* Journal of Aerosol Science, 2009. **40**: p. 16-28.

126. Luo, H.Y., Y. Liu, and X.L. Yang, *Particle deposition in obstructed airways.* Journal of Biomechanics, 2007. **40**: p. 3096-3104.

127. Shi, H., et al., *Nanoparticle Transport and Deposition in Bifurcating Tubes With Different Inlet Conditions.* Physics of Fluids, 2004. **16**(7): p. 2199-2213.

128. De Backer, J.W., et al., *Flow analyses in the lower airways: Patient-specific model and boundary conditions.* Medical Engineering and Physics, 2008. **30**: p. 872-879.

129. Moreau, J.P. *Complex Bessel Function of the 1st Kind of integer order.* 2005; Available from: http://jean-pierre.moreau.pagesperso-orange.fr/Fortran/cbessj_f90.txt.

VITA

Timothy Andrew Van Rhein was born on the 16th of September, 1986. He earned a Bachelor of Science in Mechanical Engineering from Missouri University of Science & Technology (Formerly known as University of Missouri, Rolla) in May of 2009. As an undergraduate he worked as a peer learning assistant for the Learning Enhancement Across Disciplines program. He was a member of the American Society of Mechanical Engineers. He was employed as an engineering intern by Genesis/Kolinahr in the summer of 2008. After being awarded his bachelor's degree, he was employed by The McGraw-Hill Companies and worked on the solutions manual for the ninth edition of Shigley's Mechanical Engineering Design. In 2009 he was awarded the Chancellors Fellowship and began work towards his Masters of Science in Mechanical Engineering at Missouri University of Science & Technology. While pursuing his master's degree he worked as a graduate teaching assistant and graduate research assistant under Dr. Arindam Banerjee. He presented his research titled, "Numerical Investigation of Aerosolized Drug Delivery in The Human Lungs Under Mechanical Ventilator Conditions" at the 63rd annual American Physical Society, Division of Fluid Dynamics conference in 2010. He was awarded a Master of Science in Mechanical Engineering from Missouri University of Science & Technology in December of 2012.